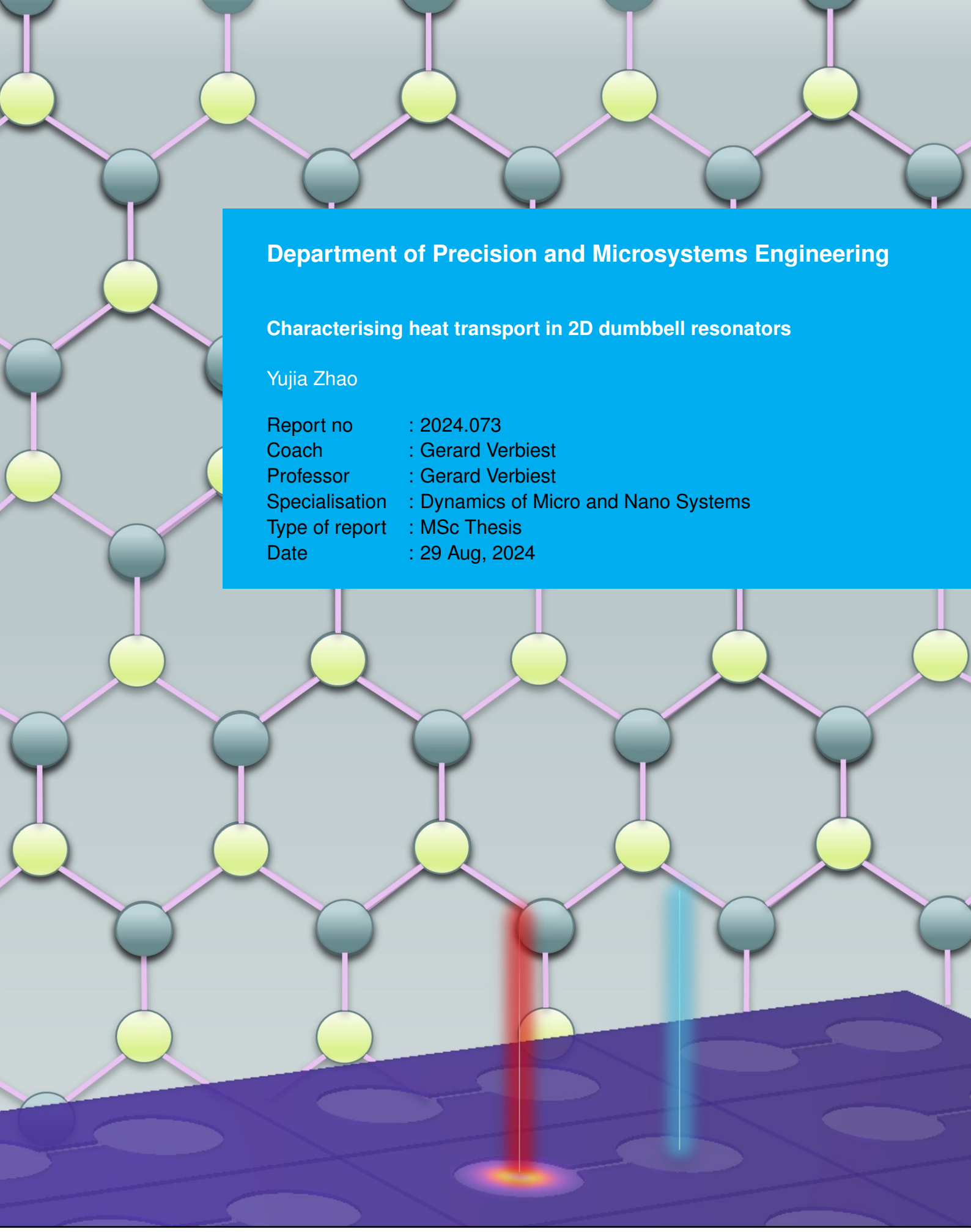

Department of Precision and Microsystems Engineering

Characterising heat transport in 2D dumbbell resonators

Yujia Zhao

Report no : 2024.073
Coach : Gerard Verbiest
Professor : Gerard Verbiest
Specialisation : Dynamics of Micro and Nano Systems
Type of report : MSc Thesis
Date : 29 Aug, 2024

Characterising heat transport in 2D dumbbell resonators

by Yujia Zhao

Student number: 5679168
Project duration: August, 2023 – August, 2024
Thesis committee: Dr. Gerard Verbiest, TU Delft, supervisor
Prof. dr. Peter Steeneken, TU Delft

Cover: Schematics of MoS_2 and COMSOL simulation of heat transfer in a chip with dumbbell resonators

An electronic version of this thesis is available at http://repository.tudelft.nl/.

TU Delft

”Human beings are poor examiners, subject to superstition, bias, prejudice, and a profound tendency to see what they want to see rather than what is really there.”

— M. Scott Peck, The Road Less Traveled

Abstract

When a free-standing membrane is actuated with photothermal method, the heat flux requires a certain time to diffuse through this membrane. This duration of time, called thermal time constant, is important for its application in sensors, nano-electromechanical systems, filters, etc. This report is devoted to exploring what plays a major role in the variation of experimentally measured thermal time constants, and to investigating the relationship between dumbbell dimensions (namely, two drum radius R_1 for drum 1 and R_2 for drum 2, half bridge width y_0, bridge length x_0) and thermal time constants.

First, dumbbell resonators of various dimensions were fabricated using exfoliated molybdenum disulfide flakes. Optomechanical experiments were conducted on these devices, involving two collocated (actuation and measurement located in the same drum) and two non-collocated (actuated at one drum and measured at the other) measurements for each device. Accordingly, four thermal time constants were extracted for each resonator through curve fitting. To understand temperature distribution and experimental variation, a COMSOL model and an analytical model were established, solving the heat equation with a harmonic laser actuation.

As a result, four thermal time constants for 16 devices were extracted. These experimental data were verified with a synergy of the two models. The primary contributors for large experimental data variation were the 2D material irregularities and laser locations. For collocated τ, it was almost unaffected by dumbbell dimensions, except for R_1 which gave a parabolic curve. For non-collocated τ, it increased monotonously with x_0, but a minimum was always observed when sweeping the other three parameters.

Such minimum occurred when x_0 is around 25$\%$ of the drum radius. This minimum was attributed to a balance between the efficiency of heat transport across the bridge and the acceptable duration required to heat the bridge itself. Meanwhile, the COMSOL model and the analytical model disagreed on the relationship between non-collocated τ and y_0, R_1, R_2. Moreover, the analytical model's deviation from the COMSOL model increased with larger bridge width or thermal conductivity. This stemmed from errors in the assumed boundary conditions: the existence of the bridge altered the temperature distribution at the boundaries of drum 1, and in the analytical model the boundaries of the dumbbell are fixed while in the COMSOL model they are controlled by the substrate.

Contents

1 Background

When a circular resonator with a thin membrane is excited by a laser with periodically fluctuating power at its centre, the temperature distribution of it u will change. It takes a certain duration τ for heat to diffuse through the whole membrane and for the resonator to regain a quasi-equilibrium. This is called a quasi state because the temperature distribution is changing periodically, with the same frequency as the excitation source. The change in temperature leads to thermal periodic thermal expansion in the membrane, Accordingly, such expansion incurs compressive stress at the edge of the membrane. The membrane is eventually pushed upward or downward, depending on the initial state. As the thermal expansion is periodical, the displacement field of the membrane is too periodic, hence this movement adds up to vibration.

By virtue of the periodicity, sweeping the excitation frequencies in experiments can offer the information of thermal signal and mechanical resonances of a device. Specifically, combining the measured data with established theories on heat transfer and vibration of circular plates, properties like Young's modulus, bending rigidity, quality factor, thermal time constant, thermal Conductivity, thermal expansion coefficient of the resonator can be extracted by curve fitting.

This is what happens to a single resonator and how it is studied with photothermal method. The same applies to any coupled resonators, yet with extra parameters characterising the coupling. This inspires us to start from investigating the vibration and heat transfer of a circular resonator, and then to combine the state-of-the-art of coupled resonators, as a background for heat transport in dumbbell resonators. Finally, insufficiency in existing literature is identified, so a motivation of this project follows.

1.1. 2D resonator

In the last decade, two-dimensional materials have gained immense popularity in research. Materials like graphene[19], MoS_2[37, 9], $FePS_3$[18] boost layered structures that is suitable for exfoliation, and such accessible fabrication urges many studies revealing their promising properties along with potential application. For instance, the low mass of 2D membranes can take the fundamental resonance to several megahertz[6, 11], which can expand the functional frequency range of sensors. In particular, thermal sensors can take advantage in the extremely high thermal conductivity of graphene[1, 39, 7]. While mass or force sensing also benefits from the low mass and high quality factor of 2D resonators[59, 46]. Moreover, information can be encoded and transferred among coupled resonators[47, 58].

Such transfer of information between resonators should be highlighted because the measured information of one resonator can be harnessed by another at a distance, and based on this more complex or efficient signal procession can be realised. This is more versatile than one-resonator setup. Besides, for almost all the applications of 2D resonators, heat dissipation or transfer is a significant concern to stabilise the device performance. Resonance, vibration amplitude, thermal conductivity, mode coupling are all temperature-dependent and thus can be sensitive to temperature fluctuation due to actuation or environment. More specifically, an impulse of actuation leads to temperature change at the driving

position in a 2D membrane, and it takes some time τ to reach an equilibrium again. The transfer of information cannot be faster than the limit set by this τ, otherwise information would be corrupted. Hence, it is important to make sure when the equilibrium is reached, and how different it is from the previous steady state.

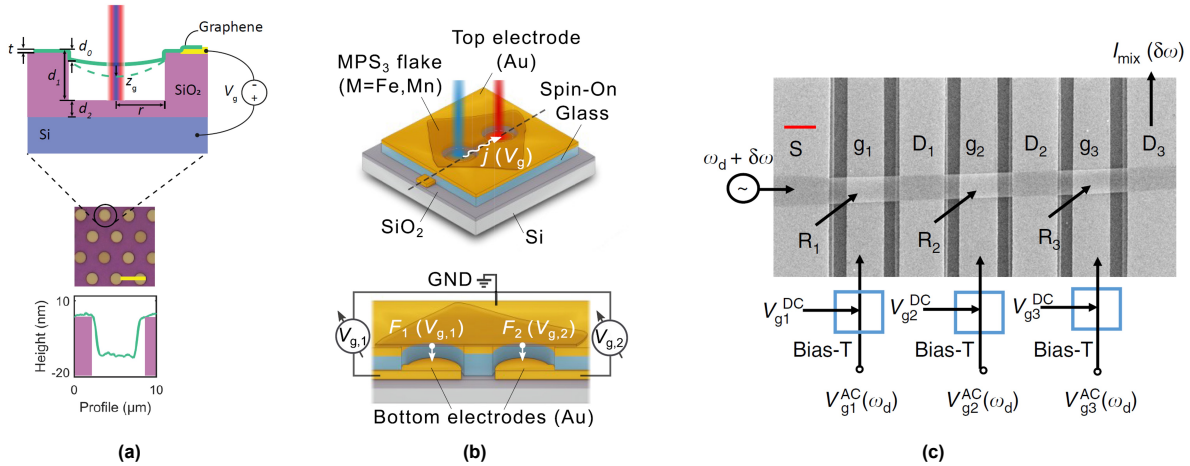

Figure 1.1: Various 2D resonators: (a) a circular resonator in literature [34]. The blue laser excitation and red laser readout are illustrated on top, and the cross section shows the profile of a membrane with pre-deformation. (b) A dumbbell resonator in literature [47]. A red and a blue laser are situated at the centre of either circular drums (top), and two gate voltages are employed to control the coupling between the two drums (bottom). (c) A graphene ribbon resonator in literature [36]. The setup comprises four contact areas S, D_1, D_2, D_3, and three gate voltages. The readout is a current I_{mix} at D_3.

In this report, a 2D resonator (also called a nanodrum) denotes a micro device comprising a substrate and a free-standing thin material that can resonate with actuation. A resonator can take assorted shapes, as shown in figure 1.1. It can be excited by one or several electrostatic[36], piezoelectric[3], magnetic[2], or photothermal[32] drives. Two examples of photothermal drives are illustrated in figure 1.1a and figure 1.1b, while an electrostatic drive is displayed in figure 1.1c.

1.2. Vibrating membranes

For a vibrating circular membrane of radius R and thickness z_t, if we assume sufficiently thin membrane thus negligible bending rigidity, small amplitude of vibration, and no damping, the displacement field z of free vibration in polar coordinates (r, θ) must satisfy:

$$\frac{\partial^2 z}{\partial t^2} = c^2 \left(\frac{\partial^2 z}{\partial r^2} + \frac{1}{r}\frac{\partial z}{\partial r} + \frac{1}{r^2}\frac{\partial^2 z}{\partial \theta^2} \right), \quad 0 \le r \le R, \quad 0 \le \theta < 2\pi \tag{1.1}$$

where c is flexural speed of sound. With boundary condition $z = 0$ at $r = R$, literature [31] gives the solution:

$$z_{mn}(r, \theta, t) = J_m(\lambda_{mn} r)[A cos(c\lambda t) + B sin(c\lambda t)][C cos(m\theta) + D sin(m\theta)] \tag{1.2}$$

where J is the first kind Bessel function, and m, n are both integers. The corresponding resonance is given by:

$$f_{mn,\ membrane} = \frac{\lambda_{mn}}{2\pi r} c = \frac{\lambda_{mn}}{2\pi r} \sqrt{\frac{n_0}{\rho z_t}} \tag{1.3}$$

where n_0 is in-plane tension and ρ is membrane density. However, if we do not assume thin membrane, the resonance frequency is no longer dominated by pretension, but instead is dictated by bending rigidity[9]:

$$f_{mn,\ plate} = \frac{\lambda_{mn}}{2\pi r^2}\sqrt{\frac{D}{\rho z_t}} \tag{1.4}$$

where D is bending rigidity and is given by:

$$D = \gamma\frac{Et^3}{12(1-\nu^2)} \tag{1.5}$$

where E is Young's modulus, ν is Poisson ratio, and γ is a factor accounting for interlayer shear interactions[52]. Naturally, there are 2D materials behaving like something between a thin membrane and a plate, and their resonance is a combination of equation (1.3) and equation (1.4):

$$f_{mn} = \sqrt{f_{mn,\ membrane}^2 + f_{mn,\ plate}^2} \tag{1.6}$$

Now we get back to equation (1.1) and investigate other assumptions. If the thin membrane is driven by a force $f(r,\theta,t)$, and the damping is $\alpha(r,\theta,t)$, then equation (1.1) evolves into:

$$\ddot{z} + \alpha(r,\theta,t)\dot{z} = c^2\nabla^2 z + f(r,\theta,t) \tag{1.7}$$

In a driven motion (i.e. excitation fixed at a frequency ω), all modes z_{mn} are excited but with different contribution to the total motion, and the solution can still be broken down to time-dependent part and time-independent part as in equation (1.2). Thus, we normalise modes to an amplitude of 1 and change the numbering from m,n into i for simplicity so that the time-independent mode shape becomes $\phi_i(r,\theta)$, and we use time-dependent $z_i(t)$ to indicate its share in the total motion. The driven motion solution $w(r,\theta,t)$ is assumed to be:

$$w(r,\theta,t) = \sum_{i=1}^{\infty} z_i(t)\phi_i(r,\theta) \tag{1.8}$$

Then we plug equation (1.8) back to equation (1.7),

$$\sum_{i=1}^{\infty}(\ddot{z}_i\phi_i) + \sum_{i=1}^{\infty}(\alpha_i\dot{z}_i\phi_i) = c^2\sum_{i=1}^{\infty}(z_i\nabla^2\phi_i) + f \tag{1.9}$$

Next, we multiply mode ϕ_j on both sides, and integrate them over the membrane area called Ω:

$$\sum_{i=1}^{\infty}\ddot{z}_i\iint_{\Omega}\phi_i\phi_j d\Omega + \sum_{i=1}^{\infty}\dot{z}_i\iint_{\Omega}\alpha_i\phi_i\phi_j d\Omega = \sum_{i=1}^{\infty}q_i c^2\iint_{\Omega}(\nabla^2\phi_i)\phi_j d\Omega + \iint_{\Omega} f\phi_j d\Omega \tag{1.10}$$

In this way, we have the mass, spring, damping, and force terms as M_{ji}, K_{ji}, C_{ji}, f_j, respectively:

$$
\begin{aligned}
M_{ji} &= \iint_{\Omega} \phi_i \phi_j d\Omega \\
K_{ji} &= -c^2 \iint_{\Omega} (\nabla^2 \phi_i) \phi_j d\Omega \\
C_{ji} &= \dot{q}_i \iint_{\Omega} \alpha_i \phi_i \phi_j d\Omega \\
f_j &= \iint_{\Omega} f \phi_j d\Omega
\end{aligned}
\tag{1.11}
$$

Finally, the equation of motion is assembled into the matrix form:

$$
\mathbf{M}\ddot{\boldsymbol{z}} + \mathbf{C}\dot{\boldsymbol{z}} + \mathbf{K}\boldsymbol{z} = \boldsymbol{f} \tag{1.12}
$$

If we assume modes are orthogonal each other, then equation (1.12) can be decoupled into:

$$
m_j \ddot{z}_j + c_j \dot{z}_j + k_j z_j + F_{nl,j} = F_{ext,j}(\omega) e^{i\omega t} \tag{1.13}
$$

where $F_{ext,j}$ is the j-th external (i.e. driving) force, and $F_{nl,j}$ is the nonlinear force, q_j is the j-th generalised coordinates, m_j, c_j, k_j are the j-th effective mass, damping, and spring, respectively. $F_{nl,j}$ is negligible if the driving amplitude is small. But we should be aware that mode coupling is always present, as Suzuki et al[50] found that the first 18 eigenvalues of a stretched drum were interdependent. For this matter, we shall delve deeper into mode coupling in section 1.3.

Previously, the excitation is fixed at one frequency, but as actuation and vibration are always of the same frequency, the steady-state solution of equation (1.13) should be a function of ω as well. When $F_{nl,j} = 0$, the solution takes the form of:

$$
z_i(\omega, t) = z_i(\omega) e^{i\omega t} \tag{1.14}
$$

Many studies start from investigating vibration modes, however, measured vibrations are never exactly the same as described in equation (1.2), and we should pay attention to the reasons. In experiments, modes can be split or degenerate, as Davidovikj et al[14] found using a phase-sensitive interferometer. The uneven distribution of built-in tension and bulging membranes can also cause the deviation from theories, as seen in the h-BN resonators under electrical tension of Chiout et al[60].

Texts above introduce the theories of vibrating membranes, and below we discuss how to extract and describe measured resonances.

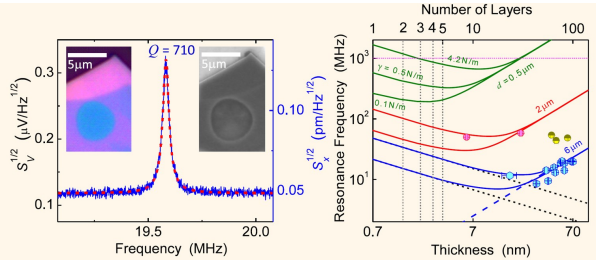

(a) Curve fitting with S_x (left) and tension tuning with various membrane thickness (right), adopted from [27].

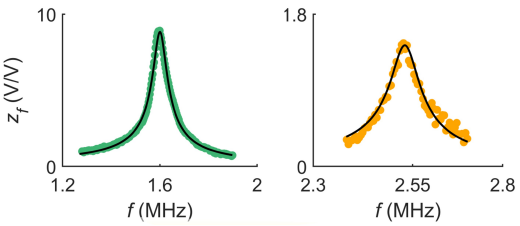

(b) Curve fitting with z_f (normalised A_f) of the fundamental (left) and second (right) resonance, adopted from [33].

Figure 1.2: Extracting properties using curve fitting

The amplitude of $q_i(t)$ in equation (1.14) is a function of frequency, and to obtain the exact location of the resonance alomng with quality factor Q, one can use curve fitting of a harmonic oscillator in equation (1.15)[33] upon measured motion-frequency relationship, as shown in figure 1.2b. Using other models like frequency-domain displacement spectral density (see figure 1.2a left) also works.

$$A_f = \frac{A/m_{eff}}{\sqrt{(\omega_0^2 - \omega^2)^2 + (\omega_0\omega/Q)^2}} \tag{1.15}$$

where A is the amplitude of driven force, m_{eff} is effective mass, ω_0 is fundamental resonance. Many studies start with building a theoretical model, and then driving a parameter ζ to measure $\zeta - f_0$ relationship (ζ refers to AFM forces, actuation power amplitude or frequency, etc.), so that properties like bending rigidity, Young's modulus, and pre-tension can be extracted by curve fitting upon equations (1.3), (1.4) and (1.6). For example, to extract Young's modulus Sajadi et al[42] built a numerical model based on Lagrange method, and Sarafraz et al[43] presented a reduced-order continuum model.

Since in experiments, the modes can be split or degenerate[14], the numbering of resonance m, n is changed into i for simplicity (for example, μ_1 refers to λ_{01} in equations (1.3) and (1.4), more are listed in literature [14]). Accordingly, equation (1.6) is transformed into:

$$f_i = \frac{\mu_i}{2\pi}\sqrt{\frac{D}{\eta\rho z_t r^4}\left[\mu_i^2 + \frac{n_0 r^2}{D}\right]}, \qquad i = 0, 1, 2... \tag{1.16}$$

where η is mass correction factor due to contamination, μ_i is a mode-specific factor.

However, the extracted resonance $\omega_{eff,i}$ and quality factor $Q_{eff,i}$ for the i-th mode by equation (1.15) usually differ from the theoretical $\omega_i = \sqrt{k_i/m_i}$ and the intrinsic $Q_i = \frac{c_i}{\omega_i m_i}$ owing to feedback forces, electrostatic interactions, gas molecules interactions, etc[48]. And those factors can be summarised as extra terms, $\omega_{extra,i}$ and $Q_{extra,i}$:

$$\omega_{eff,i}^2 = \frac{k_i}{m_i} + \omega_{extra,i}^2, \qquad \frac{1}{Q_{eff,i}} = \frac{c_i}{\omega_i m_i} + \frac{1}{Q_{extra,i}} \tag{1.17}$$

We see from equation (1.3) that material density, tension, membrane thickness (see figure 1.2a right) all play a part in resonance location, and in experiments different applied strain direction[8], nonlinear damping[38], temperature[13] can all change the aforementioned factors. Moreover, Kim et al[25] noticed hysteresis in resonance tuning and attributed this to inelastic tension and adhesion at the kink, and also reasoned that interlayer slippage or unzipped folds would reduce the tension between layers of heterostructures. Particularly, the resonance also depends on the physical state of the membrane, which is described by a thermally-induced buckling model[32].

1.3. Heat transfer in a 2D resonator

Since 2D material, in experiments, is stored with quasi-constant temperature and in vacuum, convection which relies on temperature gradient and flow of fluid in the ambient is not the dominant way of heat transfer. While radiation becomes the dominant mode when temperature is high, which is also not the case for our experiments. Hence, conduction is the dominant mode of heat transfer, especially when the materials are heated directly or have high thermal conductivity like graphene[5].

To quantify heat conduction , Fourier heat conduction equation[21] is applied to a laser-actuated drum with radius R and thickness z_t:

$$\frac{\partial u}{\partial t} = \kappa\left(\frac{\partial^2 u}{\partial r^2} + \frac{1}{r}\frac{\partial u}{\partial r} + \frac{\partial^2 u}{\partial z^2}\right) + \frac{1}{c_p\rho}\frac{dQ}{dt} \qquad in \quad 0 < z < z_t,\, 0 < r < R \tag{1.18}$$

where κ is the thermal diffusivity, and $\frac{dQ}{dt}$ is the absorbed heat flux from the actuation. Liu[31] obtained the transient (i.e. no actuation) and solution.

$$u_{trans}(r,z,t) = \sum_{m=1}^{\infty}\sum_{n=1}^{\infty} A_{mn} J_0(\eta_m r) sin\left[\frac{(2n-1)\pi z}{2z_t}\right] e^{-\lambda_{mn}^2 t} \tag{1.19}$$

where A_{mn} is the Fourier coefficient which is defined in literature [20]. This solution resembles equation (1.2), because the non-homogeneous heat equation is similar to the non-homogeneous wave equation in equation (1.1). if we compare their form:

$$\begin{aligned} \text{Wave equation:} \quad & \ddot{z} = c^2 \nabla^2 z \\ \text{Heat equation:} \quad & \dot{u} = \kappa \nabla^2 u \end{aligned} \tag{1.20}$$

we can see that mathematically the spatial variations of u in both equations is governed by the Laplacian operator despite different amplitude, while time variation differs as wave equation exhibits a higher order of time differentiation. Physically, in lattice vibration, atoms leave the equilibrium state, and consequently there are unbalanced forces on them, thus changing the acceleration, which causes the second-order partial derivative on the left side of wave equation. While temperature gradient governs the heat flow, and thus the speed of temperature change is linked to the spatial variation, leading to first-order partial derivative. Nonetheless, wave equation is akin to heat equation on the right hand side owing to the energy propagation process. When the isotropic material experiences a change in temperature, this leads to an increase in kinetic energy among the lattice constituents, causing them to vibrate. These lattice vibrations can be considered as a form of wave traveling through the lattice, propagating energy in a manner similar to a wave in a continuous medium, so two equations resemble in terms of spatial variation.

Assuming a constant amplitude A at the centre of the drum, Liu[31] also offered the quasi-steady state (i.e. uniform temperature in z direction) solution expressed with Bessel functions. Following this solution, another one not supposing constant amplitude A for all frequencies is detailed in section 2.5.

As mentioned in the beginning of this chapter, there is delay τ between laser actuation $P_{ac}e^{i\omega t}$ and membrane deflection z, and this delay is ascribed to the time needed to raise the temperature of the membrane. This process can be derived from the heat equation presented in equation (1.18)[16]. If we decompose the actuation term $\frac{1}{c_p\rho}\frac{dQ}{dt}$ in equation (1.18) into DC and AC component, i.e.:

$$\frac{1}{c_p\rho}\frac{dQ}{dt} = \frac{1}{C}\left(P_{dc} + e^{i\omega t}P_{ac}\right) \tag{1.21}$$

where C is thermal capacitance, P_{ac} and P_{dc} are laser heat flux amplitudes of AC and DC components, respectively. Then we suppose the solution of the following heat equation:

$$\dot{u} = \kappa\nabla^2 u + \frac{P_{dc}}{C} \tag{1.22}$$

can be expressed as:

$$u_{dc} = T_0\Phi(r,\theta) \tag{1.23}$$

Then adding $\frac{e^{i\omega t}P_{ac}}{C}$ as a harmonic perturbation in equation (1.22), we assume the new solution u_{ac} is in the form of:

$$u_{ac} = u_{dc} + \Delta u = \left(T_0 + \Delta T(t)\right)\Phi(r,\theta) \tag{1.24}$$

Plugging u_{ac} back to the heat equation and cancel out the terms in equation (1.22) leads to:

$$\Delta\dot{T}(t)\Phi(r,\theta) = \kappa\Delta T(t)\cdot\nabla^2\Phi(r,\theta) + \frac{P_{ac}\,e^{i\omega t}}{C} \tag{1.25}$$

To solve equation (1.25), we first tackle its non-homogeneous counterpart, i.e. $P_{ac} = 0$. Then we write:

$$\frac{\Delta\dot{T}(t)}{\Delta T(t)} = \kappa\frac{\nabla^2\Phi(r,\theta)}{\Phi(r,\theta)} = -\frac{1}{\tau} \tag{1.26}$$

where τ is a constant. Next, replacing the $\Phi(r,\theta)$-related terms with τ in equation (1.25) and resetting $P_{ac} \neq 0$ produce:

$$\frac{d\Delta T}{dt} + \frac{1}{\tau}\Delta T = \frac{P_{ac}}{C}e^{i\omega t} \tag{1.27}$$

Finally, solving for ΔT results in:

$$\Delta T = P_{ac}\frac{\tau}{C}\frac{e^{i\omega t}}{i\omega\tau + 1} \tag{1.28}$$

If we express this time constant $\tau = RC$, where R is thermal resistance, and also suppose the vibration amplitude z_ω is proportional to the temperature perturbation ΔT with a thermal expansion coefficient α, i.e. $z_\omega = \alpha\Delta T$, then we can write:

$$z_\omega = \frac{A_{th}}{1 + i\omega\tau} \tag{1.29}$$

where A_{th} is thermal expansion amplitude. For a circular resonator, the measured data of z_ω (the thermal signal at low frequencies, see figure 2.7a) is curve-fitted by equation (1.29) to obtain τ and A_{th}. With the obtained τ, thermal diffusive constant μ^2 can further be extracted using equation (1.30)[17], as an index of heat transport. Liu[31] used it to compare results of experiments, analytical models, and computational models, with values ranging from 5.02 to 5.78.

$$\tau = \frac{R^2 C_v \rho}{\mu^2 k} \tag{1.30}$$

where C_v is specific heat, k is thermal conductivity.

Furthermore, equations of coupled resonance and thermal signal can be derived. If we consider the fundamental resonance in the linear regime only, we can ignore the subscript j and $F_{nl,j}$ in equation (1.13). Then replacing the driving force $F_{ext}, j(\omega)$ with $\frac{A_{th}}{1+i\omega\tau}$ yields:

$$m\ddot{z} + c\dot{z} + kz = \frac{A_{th}}{1 + i\omega\tau}e^{i\omega t} \tag{1.31}$$

Supposing the solution of equation (1.31) is $z = z_\omega\, e^{i\omega t}$, we plug it back and obtain the amplitude z_ω as:

$$z_\omega = \frac{A_1}{1 + i\omega\tau}\cdot\frac{1}{-\omega^2 m_k + i\omega c_k + 1} \tag{1.32}$$

where $m_k = \frac{m}{k}$ and $c_k = \frac{c}{k}$, and A_1 is constant.

1.4. Coupling of resonators

For small amplitude of vibration in one nanodrum, ignoring all coupled modes can still lead to decent approximation of motion. But in reality, modes are always coupled, and the total movement is a summation of infinite number of modes. Luckily, the further the resonance of a mode from the excitation frequency, the less it contributes to the total displacement field. Hence, even for large amplitude (or in other words, nonlinear regime), considering one or two coupled mode would usually suffice. That means there would be two or three coupled equations if equation (1.12) is expanded. For instance, Keskekler [24] simplified the coupled (0,1) and (0,2) modes of a graphene resonator as:

$$\begin{aligned} \ddot{z_1} + (k_x + T_x)z_1 + \gamma z_1^3 + \tau_x \dot{z_1} + 2\alpha z_1 z_2 = Fcos(\Omega t) \\ \ddot{z_2} + (k_q + T_q)z_2 + \tau_q \dot{z_2} + \alpha z_1^2 = 0 \end{aligned} \tag{1.33}$$

where z_1 and z_2 are generalised coordinates, γ is the Duffing coefficient, and α is the coupling strength. As seen in equation (1.33), intermode coupling usually involves nonlinear terms, and the resonance of all coupled modes can be modified by tuning the amplitude of one mode, since they affect each other through tension[10].

Apart from internal mode coupling, connecting two resonators will induce coupling as well, and the simplest case is the linear resonant coupling drawn in figure 1.3a.Based on the Duffing equation and ignoring the van der Pol term due to small amplitude, one can construct the EOM of two coupled beam resonators [55]:

$$\begin{aligned} m_1\ddot{z_1} + c_1\dot{z_1} + k_1 z_1 - k_c(z_2 - z_1) = F_1(t) \\ m_2\ddot{z_2} + c_2\dot{z_2} + k_2 z_2 + k_c(z_2 - z_1) = F_2(t) \end{aligned} \tag{1.34}$$

where the coupling spring k_c can transfer elastic energy between two resonators [15]. As for dumbbell resonators, Siskins et al [47] described such linear coupled oscillators in the form of:

$$\begin{aligned} m_1\ddot{z_1} + c_1\dot{z_1} + k_1 z_1 = Jz_2 + Fcos(\omega_d t) \\ m_2\ddot{z_2} + c_2\dot{z_2} + k_2 z_2 = Jz_1 \end{aligned} \tag{1.35}$$

where J is a coupling parameter that can be tuned by voltage (see figure 1.3b).

Connecting resonators, or using 2D membranes as coupling agency can have diverse application, such as a variations of transmission for filters[54], a motion amplifier involving integrated square and circular resonator[45], a tunable motion indicator for a suspended beam and a CD actuator[51], a signal processor[47], a molecule-mass-based gas sensor[41]. Meanwhile, we should be aware that a more complex layout can change the vibration that has been introduced in section 1.2. For instance, Kirchhof et al[26] identified defect modes that could not propagate from central actuation point through a honeycomb lattice of holes, and showed that frequencies of those modes could be tuned by tension. Yang et al[57] found that a microdisk's symmetry is broken by a waveguide path, which results in mode coupling.

In recapitulate, despite a comprehensive understanding of mechanics and thermodynamics of a single resonator with insight into internal mode coupling, coupling of spatially separated resonators were only investigated by a few, and they concentrated on the mechanical part rather than the thermal. For instance, Siskins et al[47] showed the promising potential of such device to transmit bit-by-bit information with an electromechanical coupling model. Yang et al[57]demonstrated that an extra waveguide path could change the mode shape and Q factor of a microdisk. Luo et al[36] observed avoided crossings in figure 1.4b as a sign of mode coupling, and introduced a three-mode coupling model where Ω_{ij}, a measurable and tunable parameter, was employed to quantify coupling strength.

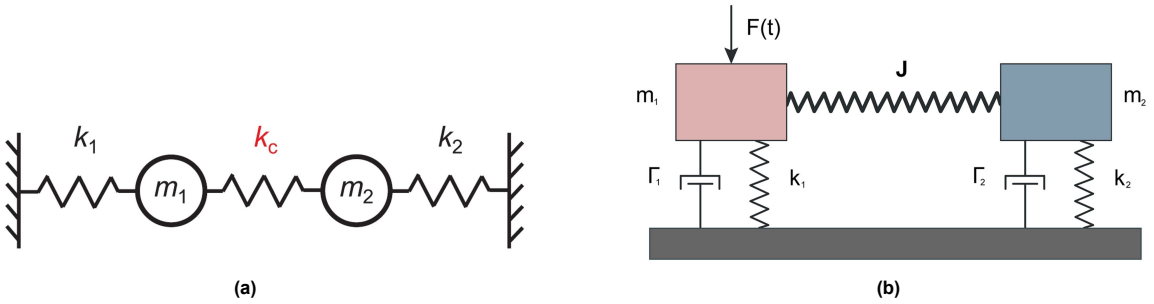

Figure 1.3: Models of coupled oscillators: (a) coupled bean oscillator, adopted from [55]; (b) Coupled nanodrum oscillator, adopted from [47].

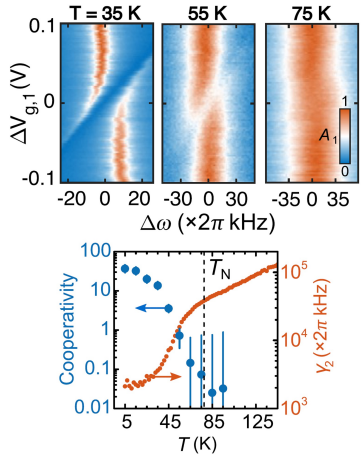

(a) Two coupled circular resonators, adopted from literature [47]. Top: the crossing is more distinct at low temperature; bottom: decreasing cooperativity and increasing dissipation rate γ_2 against growing temperature.

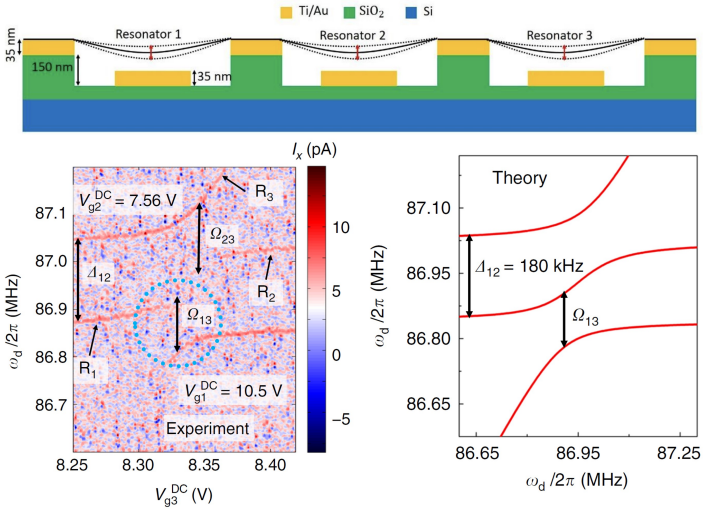

(b) Three coupled quadrilateral resonators, adopted from literature [55]. Top: schematic drawing of setup; bottom left: measured spectrum of three-mode system; bottom right: theoretical model of three-mode system.

Figure 1.4: Temperature-dependent coupling of resonators

Although most studies are focusing on the mechanical part, the thermal coupling also counts, since the thermal expansion can affect the in-plane strain and thus resonance as mentioned in section 1.1, unless the thermal signal is always well separated from the resonance. One of the simplest example of thermal coupling is two connected objects with different temperature, and the conduction is governed by the Fourier's law:

$$\boldsymbol{q} = -k\nabla u \tag{1.36}$$

where $\boldsymbol{q}$ is heat flux density vector, and u is the temperature field. In fact, the Fourier's law is related to the heat equation in equation (1.20). Using the first law of thermodynamics, the rate of change in thermal energy inside a volume must be identical to the net heat flux into this volume[4]:

$$\frac{\partial(\rho c_p u)}{\partial t} = -\nabla \boldsymbol{q} \tag{1.37}$$

Regarding material density ρ and specific heat c_p as constant and combining equation (1.36), equation (1.37) becomes:

$$\frac{\partial u}{\partial t} = \frac{k}{\rho c_p} \nabla^2 u \tag{1.38}$$

where $\frac{k}{\rho c_p}$ equals to the thermal diffusivity κ.

Although there are already solutions for a circular plate or a rectangular plate, heat transfer or thermal coupling between resonators has not yet been thoroughly investigated. Analytically, solving heat equation can fuel our investigation into the temperature pattern of a dumbbell resonator with the correct boundary condition.

1.5. Motivation

The existing literature on coupled resonators in general focus on building a mathematical or computational model to describe their vibration modes, and using experimental methods to visualise mode shapes or extracting constants, which is similar to what has been done to a single resonator. By characterising properties like resonance, coupling strength, cooperativity, etc, a tunable information transmitter can be built. However, figure 1.4 shows that all these properties depends on temperature, and very few studies have been published to examine the heat transfer from the heated (actuated) resonator to the reactive (measured) one. This is important because the resonance of the measured resonator would change due to heat flux input from the actuated one, and an unknown thermal coupling between two resonators can lead to inaccurate information transfer. Such issue inspires us to study the heat transfer and thermal coupling of two resonators by characterising how fast and how much the heat transfer is, with approaches that have been applied to a single resonator.

Ideally, the thermal time constant can be an indicator for how long the input-output delay should be, while thermal expansion coefficient indicates the vibration amplitude, and they are both useful information for potential application, i.e. sensors and signal processors. In practice, it would be difficult to obtain a clear signal for all resonator devices with the same actuation power, so cimparing thermal expansion would be more complex. Therefore, this project concentrates on the thermal time constant τ, which does not depend on actuation power amplitude[31].

2

Methodology

This chapter consists of all preparations and approaches employed to investigate the thermal signal in a dumbbell resonator, from making samples to solving differential equations in an analytical model. In this way, experiments, simulation, and analytics ensure a thorough understanding of heat transfer in a dumbbell resonator. To simplify the terminology, the dimensions and components of a dumbbell resonator is defined in figure 2.1.

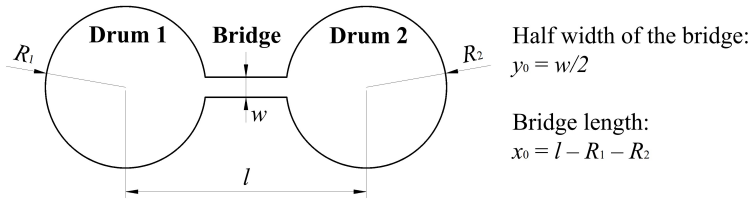

Figure 2.1: Terminology of a dumbbell resonator

2.1. Sample fabrication

As defined in chapter 1, a resonator comprises substrate and free-standing material, and this section introduces how to prepare the 2D material part. As for the substrate, chips prepared by Liu[31] are employed. These chips features a 285-nm layer of silicon dioxide upon a silicon wafer, and the well-defined cut is made by electron beam lithography and later etched by CHF_3 and Ar plasma. The chip offers circular drums ranging from 2 to 5 μm in radius, and dumbbells with width y_0 from 0.2 to 1.5 μm and length x_0 from 0.5 to 7 μm.

Although there are several ways of creating atomically thin flakes, including chemical vapor deposition (CVD)[29], liquid phase exfoliation[56], electrochemical exfoliation[49], the original mechanical exfoliation[40] by tapes remains the simplest yet still powerful method to prepare membranes. Mechanical exfoliation can maintains the intrinsic properties of the material without introducing chemical residues, but it is limited to small-scale production thus requires more manual labour. Fortunately, the largest dumbbell in the chip covers a rectangular of $27\mu m \times 10\mu m$, thus relatively small flakes would suffice, while the inefficiency is negligible if a mere dozen of samples are to be prepared.

To start with mechanical exfoliation, thick flakes are collected and stored on scotch tapes (dubbed original tapes). On an original tape, One can identify shiny patches, where thick flakes abound, ideal for peeling off top layers while still preserving flake size. Then new scotch tapes would be attached to the original tapes for the first round of exfoliation, and more rounds can be conducted until there are abundant flakes that are not all shiny. Then these tapes are then attached to polydimethylsiloxane (PDMS) stamps to thin out the layers for a final round. Through fast releasing of the tape from the PDMS, some thin flakes of 1 nm to 20 nm can be created and found with microscopy.

In our experiments, MoS_2 was used owing to its availability in the lab. Usually, MoS_2 flakes of 1 nm to 15 nm in thickness on PDMS exhibit no metallic gaze and are rather dull, as shown by the red arrows in figure 2.2a, while the thickest ones are often grey or golden with wrinkles, depending on the light source. After locating thin flakes, they are aligned on the top of a dumbbell cavity and by attaching PDMS to the chip and slowly releasing it, the flakes are transferred to the chip. This works because the chip is made of SiO_2 and exhibits a stronger adhesion compared to PDMS. To further enlarge the adhesion force gap between the two materials, one can heat up the chip up to 40 °C.

As a result, a dumbbell cavity can be fully covered by 2D MoS_2, and the thinnest ones (around 5 nm thick, see figure 2.2c) exhibit an indigo hue, while the medium ones (around 20 nm thick, figure 2.2d) manifest a lighter blue, but the thicker ones (around 50 nm thick, see figure 2.2b) display shades of greyish-green. Sometimes a stark dark part can remain on the chip, as seen in figure 2.2d, and this stems from parts of a flake not attached to the chip, often caused by a dusty chip or dots of previously transferred material underneath that weaken the adhesion. Therefore, fabrication should be conducted in a cleanroom to minimise the interference of small particles.

Observing the fabricated samples, hues of deep crimson on the yellow dumbbells or nanodrums indicates pre-deformation thus uneven strain in the material, and that is ineluctable. What can be improved is the uniformity of material thickness, for example, the top right sample in figure 2.2c is more desired than the top left one.

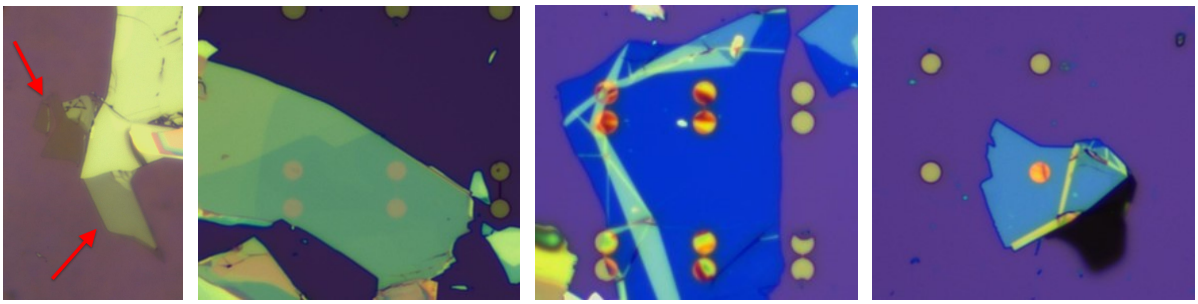

Figure 2.2: Examples of fabricated MoS_2 flakes: (a) before transferring to the chip, thin flakes take a dull to opaque look; (b) relatively thick flakes of approximately $50nm$ are in greenish hues; (c) thin flakes of around $10nm$ are blue to indigo; (d) completely dark part indicates flakes not adhere to the chip surface.

2.2. Optomechanical measurement

The setup is drawn in figure 2.3, featuring an actuation laser, a readout laser, and an analyser to show the results.

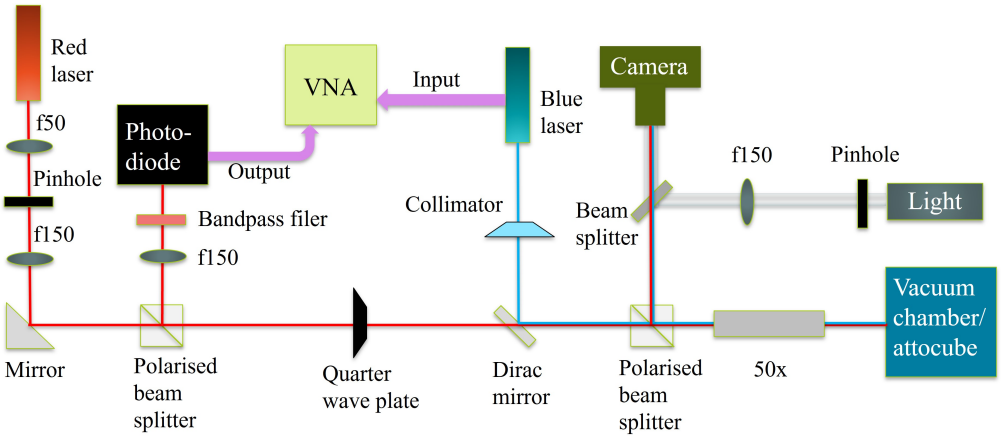

Figure 2.3: Schematics of optomechanical measurement setup

When dumbbell resonators have been fabricated a on chip, the chip is fixed in the attocube (i.e. the vacuum chamber) by double-sided tapes. The attocube is a metal box with 3-DoF positioner controlled by piezos.

Turning on the red laser, the 632 nm wavelength beam serves as actuation, and it shines through two focal lengths and a pinhole to assure that the light is concentrated and parallel to the table surface. Limited by the table size, a mirror anchored in the corner directs the red laser into a polarised beam splitter (PBM), which, as the name suggests, split the incident beam into two perpendicular polarised beams. The transmitted beam travels towards the sample in a vacuum chamber, and when this beam finally meets the vibrating membrane, part of it would be reflected back. The quarter-wave plate needs to be tuned for a maximum reflected light (i.e. a 45° angle), as in the light path of the red laser lies two PBS in figure 2.3. Now this reflected light adds up to the transmitted beam and the sum is read by a photodiode, which converts light into an electrical current. This current, containing information of light phase and intensity, would be the output of a vector network analyser (VNA).

In order to read at various positions, the blue laser with 404 nm wavelength transmits through a collimator and then a dirac mirror mounted on H45 (which makes the light wave polarized at a 45° angle to the horizontal plane). The collimator can narrows the beam, and it is attached to a plane positioner of 2 DoFs, so by fine-tuning the knobs on the positioner, the blue laser sopt can land on a desired location. While the dirac mirror reflects the blue laser but let the red laser pass. It also features a plane positioner, so that one can make sure that the concentrated blue laser dive into the hole of the 50x objective lens.

As for the CCD (Charge-Coupled Device) camera, it takes the background light from a light source, and presents the image of devices in the vacuum chamber along with laser spots. However, the focus for the camera is not necessarily the focus of lasers, and in fact hard to align their focus. Hence, in experiments, the camera is used to do the first stage of location, and then by moving the positioner in the vacuum chamber to reach maximum signal in VNA plots, one can find the optimal actuation location at the centre of a circular drum, or as close to it as possible.

After locating the sample in the camera, for each dumbbell resonator, four measurements are to be carried out, as depicted in figure 2.4. Actuating at drum 1 and reading at drum 2 is called measurement ”drum 12”, and the corresponding thermal time constant is dubbed ”τ_{12}”, as shown in setup 4. The same nomenclature is applied to the rest of the setups in figure 2.4.

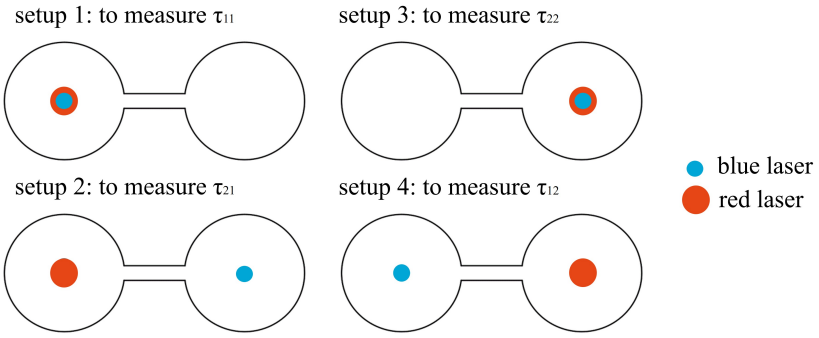

Figure 2.4: Four measurements of each dumbbell resonator

The VNA plays a key role in each measurement, as it calculates the transfer function from red laser readout to blue laser actuation. When the membrane vibrates, the depth of the cavity fluctuates, and the reflected light from the membrane and from the substrate can add up or cancel each other, so that the total intensity of reflected light is a function of driving frequency, and this information is stored in the current $I_{red}\, e^{i\omega t+\phi}$ flowing into the VNA from the photodiode. The current controller of blue laser (i.e. DC controller) would produce a current I_{blue}, and the VNA would add a harmonic part to it and results in a current $\beta I_{blue}(\alpha + P_{ac}e^{i\omega t})$, where α and β are constants, and this current acts as the AC controller, dictating the blue laser behaviour over time. In the end, the VNA would plot the amplitude of signal $S(I_{blue}, P_{ac}, \omega)$, as shown in figure 2.6a, by calculating:

$$S(I_{blue}, P_{ac}, \omega) = \frac{1}{t_0}\int_0^{t_0} \frac{\beta I_{blue}(\alpha + P_{ac}e^{i\omega t})}{I_{red}\, e^{i\omega t+\phi}} dt \tag{2.1}$$

where I_{blue} is the input of DC controller of blue laser, while P_{ac} is the input of AC controller in VNA. And t_0 is the integration time, which is determined by the bandwidth ω_b (usually within 10 Hz to 100 Hz for a precise measurement):

$$t_0 = \frac{1}{\omega_b} \tag{2.2}$$

Therefore, both the DC and AC controller can affect the DC intensity of blue laser, and the DC intensity is associated with the strain in the membrane. While only the AC one determines the amplitude of harmonic driving. In experiments, the maximum AC power is limited to 8 dBm in the VNA due to the vulnerable photodiode.

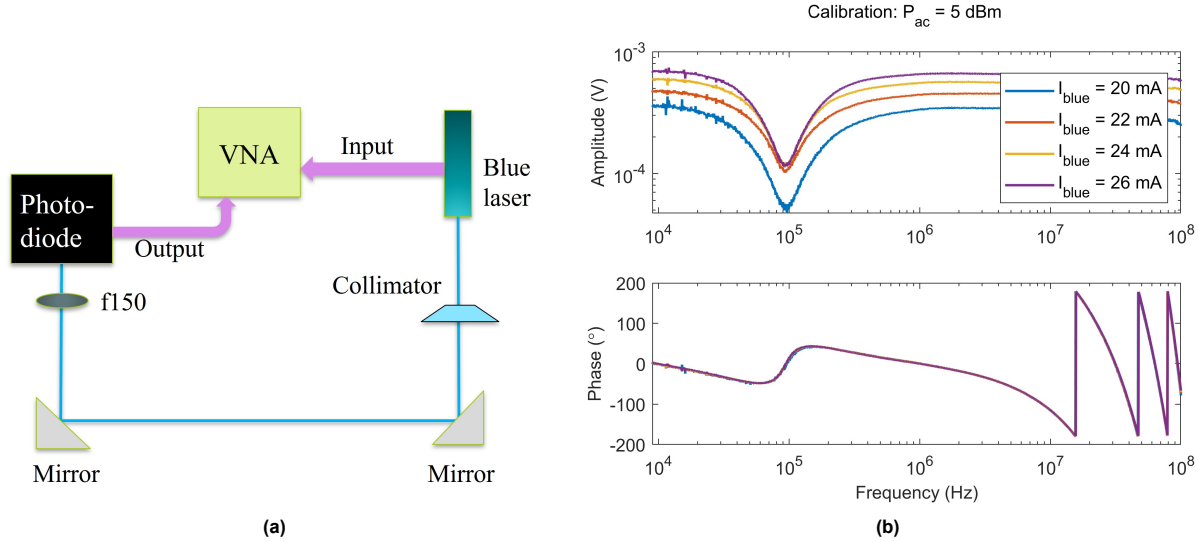

Figure 2.5: (a) calibration setup; (b) calibration results

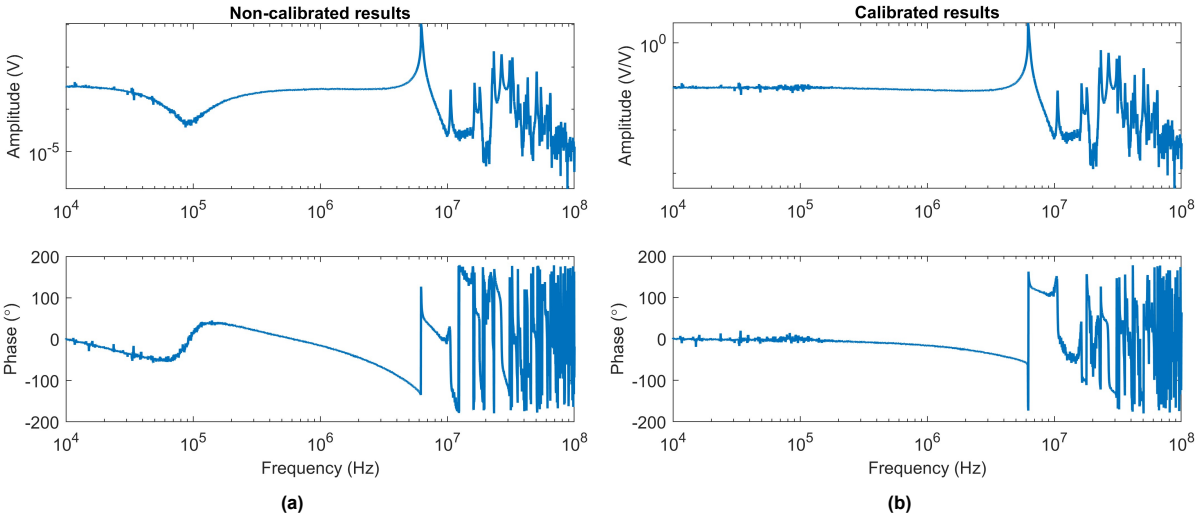

Figure 2.6: Comparison of bode plots of device 8, drum 11: (a) non-calibrated results and (b) calibrated results

Since the thermal time constant is usually much smaller than the delay in the system, a calibration to filter out this delay need to be conducted. The amplitude of calibration curves depend on the DC controller but not he AC controller, Therefore, each measurement $S(I_{blue}, P_{ac}, \omega)$ should be calibrated with corresponding calibration $S_{cali}(I_{blue}, \omega)$ by:

$$z(I_{blue}, P_{ac}, \omega) = \frac{S(I_{blue}, P_{ac}, \omega)}{S_{cali}(I_{blue}, \omega)} \tag{2.3}$$

where P_{ac} and P_{dc} are power of AC and DC controller, respectively, and $z(I_{blue}, P_{ac}, \omega)$ denotes the calibrated results, as presented in figure 2.6b. Comparing the two bode plots in figure 2.6, the phase lag in calibration is subtracted from the raw data, while the shape of resonance is preserved despite the amplitude division.

With the calibrated results, one can separate the real and imaginary part to identify the thermal signal, often found as a valley in the imaginary part at 10^6 Hz to 10^8 Hz with molybdenum disulfide resonators. The exact thermal time constant τ is calculated by a curve fitting of the following model:

$$z(I_{blue}, P_{ac}, \omega) = \frac{A_{th}}{1 + i\omega\tau} \tag{2.4}$$

where A_{th} is the thermal amplitude. Similar to similar to equation (1.15), the amplitude of the resonance A_f can be fitted by:

$$A_f = \frac{A_{reso}}{\sqrt{(\omega_0^2 - \omega^2)^2 + (\omega_0\,\omega/Q)^2}} + B_{reso}\,\omega + C_{reso} \tag{2.5}$$

where $\omega_0 = 2\pi f_0$ is the resonance frequency, Q is the quality factor, and A_{reso}, B_{reso}, C_{reso} are constants. A linear perturbation $B_{reso}\,\omega + C_{reso}$ is added since the resonance can reside on the deep slope of the thermal signal, thus being lopsided. An example of such fitting is drawn in figure 2.7b.

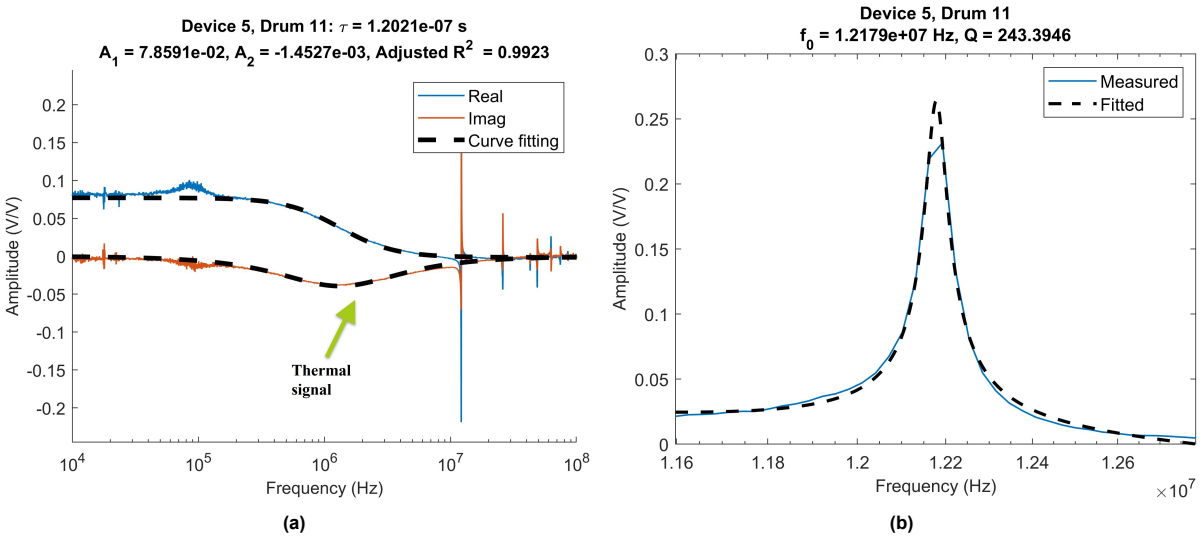

Figure 2.7: Curve fitting of: (a) thermal signal with equation (2.6) and (b) resonance amplitude with equation (2.5)

However, in the curve fitting of equation (2.4), a constant discrepancy in the real part is usually present, which inspire us to modify equation (1.29) and to use the following model for curve fitting:

$$z(I_{blue}, P_{ac}, \omega) = \frac{A_1}{1 + i\omega\tau} + A_2 \tag{2.6}$$

where A_1 is the same as A_{th} in equation (2.4), and A_2 is a real constant denoting the gap. An example of fitting is shown in figure 2.7a, where the thermal signal can clearly be recognised by the green arrow. Nonetheless, there is still some measurement with a merged thermal signal and resonance. As derived in equation (1.32), a coupled model updated from equation (2.6) is used for curve fitting:

$$z(I_{blue}, P_{ac}, \omega) = \left[\frac{A_1}{1 + i\omega\tau} + A_2\right] \frac{1}{-\omega^2 m_k + i\omega c_k + 1} \tag{2.7}$$

where m_k and c_k are constants that can be derived from resonance and Q factor. Finally, some measurement do not have a ideal fitting with any models above, which might be caused by the coupling of the two circular drums. The following model with a coupling term exhibits a better fitting in terms of the coefficient of determination adjusted R squared:

$$z(I_{blue}, P_{ac}, \omega) = \left[\frac{A_1}{1 + i\omega\tau} + (a + bi)\omega + c + di\right] \frac{1}{-\omega^2 m_k + i\omega c_k + 1} \tag{2.8}$$

where a, b, c, d are all real constants. The results of the three model equation (2.6), equation (2.7), and equation (2.8) are presented and compared in section 3.1.

2.3. AFM measurement

The atomic force microscope (AFM), a high-resolution type of scanning probe microscopy, is a widely used experimental method to characterise static[23, 44, 30] and recently dynamic properties[12] of membranes. In our case, the drive bend a cantilever that is connected to a probing tip. When the tip moves upon the sample, the topology of it, described by pixels over the measuring range, can be obtained. And in this way, the thickness, among other properties, can be measured. When more deflection is exerted to the cantilever and thus more deflection in the sample, a force-displacement relationship can also be recorded[8].

More specifically, the topology data is processed by Gwyddion to compensate error in measurement, with the assumption that the surface of the chip is flat. Then two masks, indicated by two rectangular boxes in figure 2.8, are created to represent the height of the base (i.e. chip surface) and that of the membrane, respectively. Next, we fit height values of pixels in each mask to a normal distribution, and the thickness of a membrane is calculated as the height difference between the base and the membrane, as shown in figure 2.8b.

Table 2.1: Dimension of dumbbell devices

Device	$R_1(\mu m)$	$R_2(\mu m)$	$w(\mu m)$	$l(\mu m)$	$t(nm)$
1	5.0	5.0	0.2	15.0	13
3	2.5	5.0	0.6	11.5	15
4	4.0	4.0	0.3	12.0	8
5	4.0	4.0	0.4	15.0	60
7	4.0	4.0	0.3	15.0	60
8	5.0	5.0	0.6	12.0	13
9	5.0	5.0	0.6	11.0	13
10	5.0	5.0	0.2	12.0	13
11	3.0	3.0	0.3	8.0	-
12	5.0	5.0	0.2	17.0	9
14	5.0	5.0	0.6	17.0	9
15	4.0	4.0	0.6	12.0	17
16	4.0	4.0	0.5	11.0	12
17	4.0	4.0	0.5	10.0	12
18	3.0	3.0	0.4	8.0	-
19	2.0	3.5	0.6	9.5	15

As a result, in total 19 devices are measured and listed in table 2.1. Device 2 and 6 are not listed due to a behaviour not obeying any of the three aforementioned model thus not included in extracting thermal

time constants, and this behaviour is discussed in section 3.2. Device 13 is excluded due to a failure in measuring its τ_{21}. Except for device 4 and 5, membranes of the devices boost small variation in thickness, within $12 \pm 5\,nm$. For devices 11 and 17, thickness is no longer measurable, owing to too large a initial force in the AFM setting, or decay during optomechanical measurement.

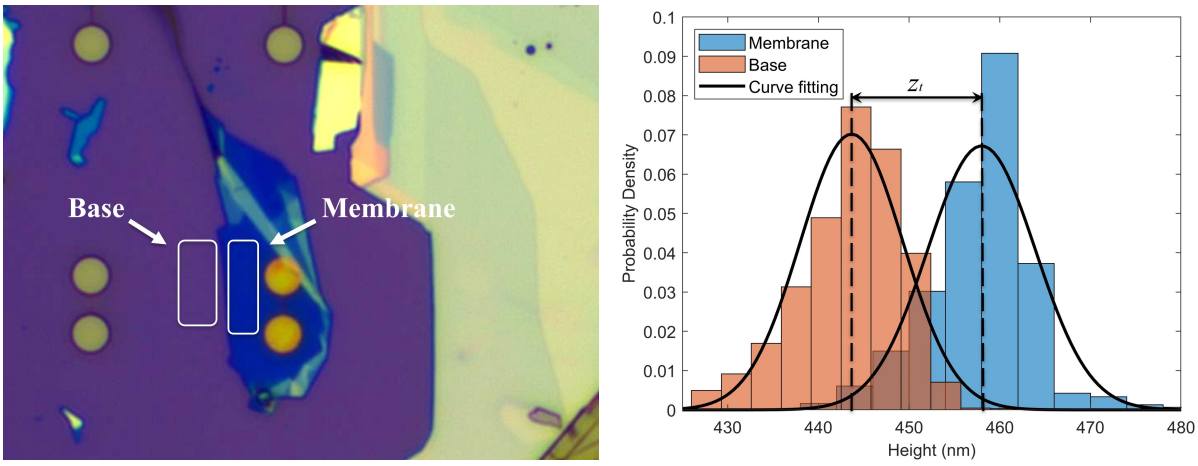

(a) (b)

Figure 2.8: Post-processing of AFM measurement: (a) mask location of the base and the membrane; (b) curve fitting of normal distribution to obtain the membrane thickness z_t.

2.4. COMSOL simulation

With the ”heat transfer in solids” module in COMSOL multiphysics, similar setup of laser actuation and readout in figure 2.4 can be established. To begin with, a 3D model of a circular drum (shown in figure 2.9a) was built to match the results calculated by Liu's verified axis-symmetric model[31] using ”heat transport in thin shells module”. Then this 3D model is expanded to become a dumbbell resonator, as shown in figure 2.9b.

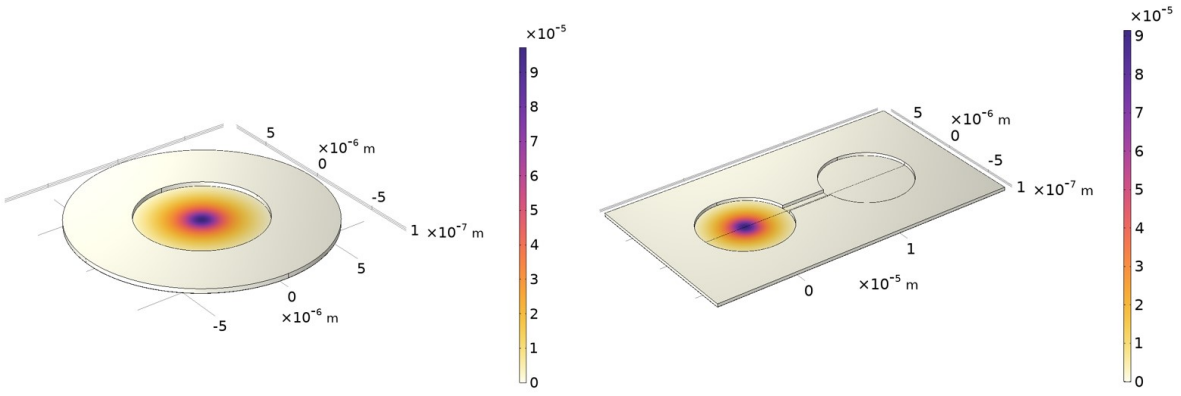

(a) (b)

Figure 2.9: Surface temperature (in Kelvin, bottom view) distribution at 1 MHz calculated by: (a) 3D circular drum model, and (b) dumbbell model.

To build this model, a rectangular 2D membrane is placed on a SiO_2 plate of 285 nm in thickness, and drum 1 is actuated by a heat source with normal distribution in space, as defined in equation (2.15). Then a harmonic perturbation featuring 10 kHz to 1000 MHz heating is calculated and shown in figure 2.11. Clear thermal signal can be identified in all three graphs, despite fluctuations in figure 2.11b and figure 2.11c at high frequencies that are not obvious in experiments. Furthermore, we could also define analytic functions to simulate readout locations, as explained in equation (2.39).

As for boundary conditions, the temperature is set to be constant at 293.15 K at the bottom of the substrate, which is attached to the positioner in the vacuum chamber (see figure 2.3, not modelled in the COMSOL simulation). Since the positioner is much larger than the substrate, temperature change of the positioner due to lasers is negligible. Thus, the bottom of the substrate should be kept at room temperature, as shown in figure 2.10a. For other surfaces, there is a thermal insulation owing to the vacuum environment. As the default boundary condition, it is named **BC1**, and is applied to all simulations in chapter 3.

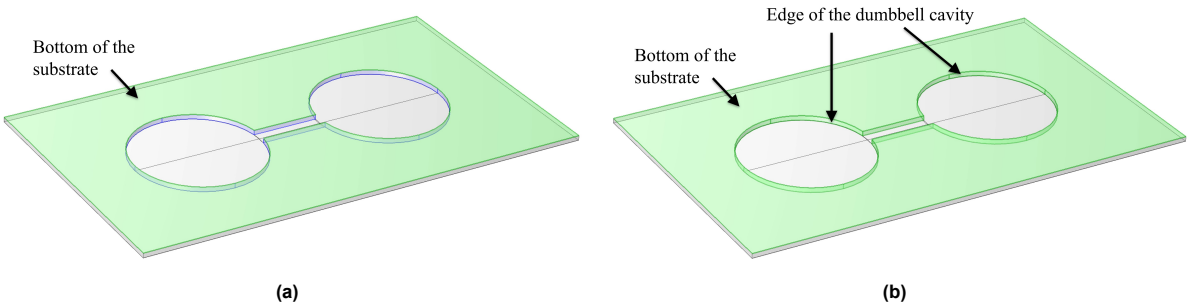

Figure 2.10: Boundary condition of surfaces with constant temperature, coloured in green: (a) **BC1**, only bottom of the substrate, applied in chapter 3; (b) **BC2** with extra surfaces at the edge of the dumbbell cavity, applied in section 4.2.

However, this boundary condition is not exactly the same as that of the analytical model introduced in section 2.5. For this matter, another boundary condition with an extra constant temperature for the edge of the dumbbell cavity, as indicated by the green surfaces in figure 2.10b. This boundary condition called **BC2**, and is applied in some of section 4.2 simulations.

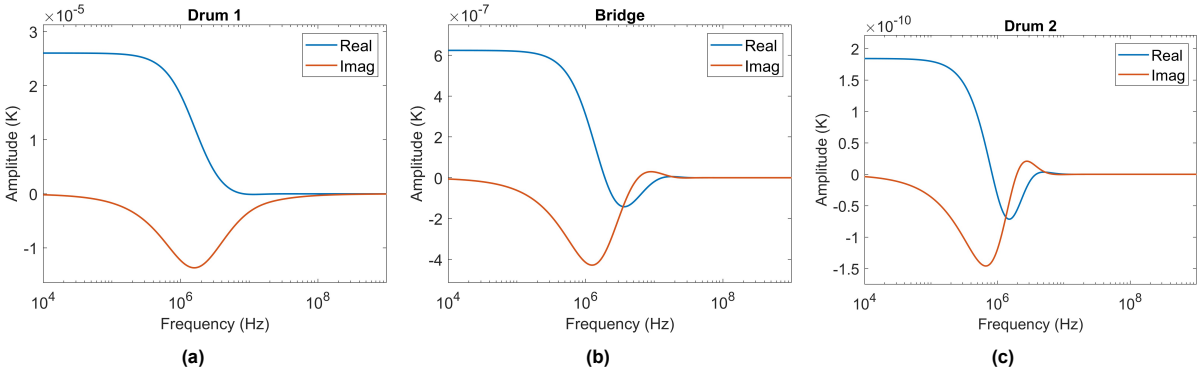

Figure 2.11: Average surface temperature of: (a) drum 1, (b) bridge, and (c) drum 2, calculated by the dumbbell model with parameters: $R_1 = R_2 = 4\mu m$, $x_0 = 4\mu m$, $y_0 = 0.5\mu m$, $H_0 = 1.5 \cdot 10^{10}$ W/m^2, $r_0 = 0.5\mu m$, $k = 40$ W/(m · K), $\rho = 5060$ kg/m^3, $c_p = 240$ J/(g·K). Boundary conditions follow figure 2.10a.

2.5. Analytical calculation

COMSOL simulation can offer us a temperature distribution induced by a harmonic heat source, but to dig out the exact pattern, an analytical solution needs to be developed. This section employs the nomenclature in figure 2.1, and derives the temperature distribution for drum 1 as $u_1(x,t)$, bridge as $v(x,y,t)$, and drum 2 as $u_1(x,\theta,t)$, with the coordinates illustrated in figure 2.12.

Starting with drum 1, we consider a two-dimensional circular resonator heated up by a fluctuating power $P(x,t)$, and for simplicity this problem is regarded as axisymmetric, the heat equation can be written as:

$$\frac{\partial u_1}{\partial t} = \kappa \left(\frac{\partial^2 u_1}{\partial x^2} + \frac{1}{x}\frac{\partial u_1}{\partial x} \right) + P(x,t) \tag{2.9}$$

First we solve for the solution of homogeneous equation (2.9), i.e. $P(x,t) = 0$. Assume the variables are separable, thus:

$$u_1(x,t) = U_1(x)e^{i\omega t} \tag{2.10}$$

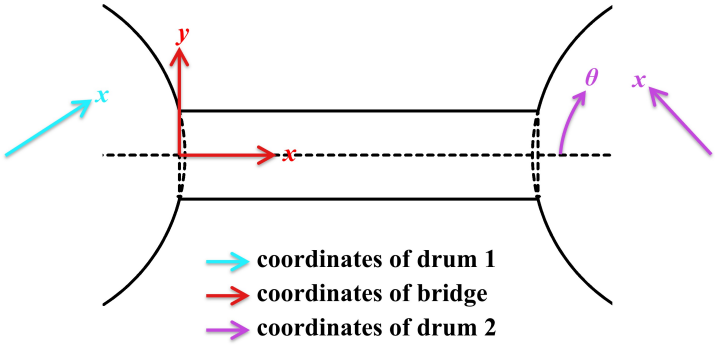

Figure 2.12: Coordinates applied in analytical calculation

Plugging equation (2.10) into equation (2.9) yields:

$$x^2\frac{dU_1}{dx^2} + x\frac{dU_1}{dx} + x^2\frac{i\omega}{\kappa}U_1 = 0 \tag{2.11}$$

Then equation (2.11) is in the form of Bessel's differential equation, hence the solution is:

$$U_1(x) = \sum_{i=0}^{n}\left[c_i J_i(mx) + d_i Y_i(mx)\right] \tag{2.12}$$

where $m = \sqrt{-\frac{i\omega}{\kappa}}$. Due to no singularity at $x = 0$, we set $d_i = 0$. After applying boundary condition $U_1(R_1) = 0$, c_n can be expressed as:

$$c_n = -\frac{\sum_{i=0}^{n-1} c_i J_i(mR_1)}{J_n(mR_1)} \tag{2.13}$$

In this way, $U_1(x)$ can be rewritten as:

$$U_1(x) = \sum_{i=0}^{n} c_i w_i(x) = \sum_{i=0}^{n-1} c_i\left[J_i(mx) - \frac{J_i(mR_1)}{J_n(mR_1)}J_n(mx)\right] \tag{2.14}$$

As $u_1(x,t)$ now only satisfies the homogeneous heat equation $\dot{u} = k\nabla^2 u$, the solution of the non-homogeneous one (see equation (2.9)) is considered to be the same form as $U_1(x)\,e^{i\omega t}$, so that the Galerkin method can be applied to determine coefficient c_i. First, the actuation power $P(x,t)$ writes:

$$P(x.t) = P_0(x)e^{i\omega t} = H_0 e^{-\frac{x^2}{r_0^2}}e^{i\omega t} \tag{2.15}$$

where H_0, r_0 are constants. Then plugging $u_{nh}(x,t)$ into the non-homogeneous equation when using Galerkin method gives:

$$\int_0^{R_1} \sum_{i=0}^{n-1} \left[c_i i\omega \cdot w_i(x) - c_i k\nabla^2 w_i(x) - P_0(x)\right] \cdot w_j(x) x dx = 0\,, \quad (j = 0, 1, 2..., n-1) \tag{2.16}$$

To solve for c_i in equation (2.16), it is reconstructed into matrix form $\mathbf{A}\mathrm{c} = \mathrm{f}$, where:

$$\begin{aligned} A_{ij} &= \int_0^{R_1} \left[i\omega \cdot w_{j-1}(x) - k\nabla^2 w_{j-1}(x)\right] w_{i-1}(x) x dx \\ f_i &= \int_0^{R_1} P_0(x) w_{i-1}(x) x dx \end{aligned} \tag{2.17}$$

Note that i and j in equation (2.17) are 1-based, instead of 0-based as in equation (2.16). Hence, the coefficient c_i assembled in c in equation (2.16) can be calculated by:

$$\mathrm{c} = \mathbf{A}^{-1}\mathrm{f} \tag{2.18}$$

Following the solution of equation (2.14), we can proceed to obtain the solution of heat equation for the bridge part, $V(x, y)$. Assuming the width of the bridge is small relative to the diameter of the circular drum, the change in temperature distribution of drum 1 $U_1(x)$ because of the opening on drum 1's boundary is negligible, then $U_1(x)$ can directly be applied as input of the bridge part. Thus, the boundary condition of the bridge part writes:

$$v(x, y = \pm y_0, t) = 0; \quad v(x = 0, y, t) = u_1(\sqrt{y^2 + R_1^2 - y_0^2}, t) \tag{2.19}$$

where y_0 is half width of the bridge. Similar to how we solved equation (2.11), the homogeneous equation is considered thanks to negligible heating power on the bridge part, and the solution is assumed to be:

$$v(x, y, t) = V(x, y)e^{i\omega t} = X(x)Y(y)e^{i\omega t} \tag{2.20}$$

Plugging equation (2.20) into the homogeneous heat equation gives:

$$\frac{i\omega}{\kappa} = \frac{1}{X}\frac{d^2X}{dx^2} + \frac{1}{Y}\frac{d^2Y}{dy^2} \tag{2.21}$$

The solution of equation (2.21) can be presented in the form:

$$X(x) = A_x e^{-\sqrt{s}x} + B_x e^{\sqrt{s}x} \tag{2.22}$$

$$Y(y) = A_j cos\left(\frac{(j + \frac{1}{2})\pi y}{y_0}\right), \quad j = 1, 2, 3... \tag{2.23}$$

where $s = \frac{i\omega}{\kappa} + \frac{(j+1/2)^2\pi^2}{y_0^2}$, and A_x, B_x, A_n are constants. Along the x-axis of the bridge, we suppose the temperature drop for no heating is present, i.e.:

$$\frac{dX}{dx} < 0 \quad for \quad x > 0 \tag{2.24}$$

Hence $B_x = 0$, and the solution can be assembled into:

$$v(x, y, t) = \sum_{j=0}^{n} \left[a_j V_j(x, y)\right] e^{i\omega t} = \sum_{j=0}^{n} \left[a_j e^{-\sqrt{s}x} cos\left(\frac{(j + \frac{1}{2})\pi y}{y_0}\right)\right] e^{i\omega t} \tag{2.25}$$

To determine coefficients a_j, we use the Galerkin method to satisfy the boundary condition in equation (2.19). Note that $Y(y)$ already satisfies the first boundary condition, and it can serve as a set of orthogonal base. Then the Galerkin equation to satisfy the second boundary condition reads:

$$\int_0^{y_0} \sum_{j=0}^{n} \left[a_j V_j(x=0,y) - U_1\left(\sqrt{y^2+R_1^2-y_0^2}\right)\right] cos\left(\frac{(k+\frac{1}{2})\pi y}{y_0}\right) dy = 0, \quad k=0,1,2... \tag{2.26}$$

With a similar approach in equation (2.17), the solution of $v(x,y,t)$ can be attained: equation (2.26) is rearranged in matrix form $\mathbf{K}\mathrm{a} = \mathrm{p}$, where:

$$\begin{aligned} K_{ij} &= \int_0^{y_0} V_{j-1}(x=0,y)\, cos\left(\frac{(i-\frac{1}{2})\pi y}{y_0}\right) dy \\ p_i &= \int_0^{y_0} U_1\left(\sqrt{y^2+R_1^2-y_0^2}\right) cos\left(\frac{(i-\frac{1}{2})\pi y}{y_0}\right) dy \end{aligned} \tag{2.27}$$

Note that i and j are again 1-based in equation (2.27). The final step is to solve a_j in array a with:

$$\mathrm{a} = \mathbf{K}^{-1}\mathrm{p} \tag{2.28}$$

Using $V(x,y)$, the coupling of the bridge is defined as:

$$V_{cp} = \frac{V(x=x_0,y)}{V(x=0,y)} \tag{2.29}$$

From this point on, we again use $v(x,y,t)$ as the input of drum 2, with assumption that the introduction of drum 2 would not change $v(x,y,t)$. In drum 2, the temperature distribution $u_2(x,\theta,t)$ must satisfy:

$$\frac{\partial u_2}{\partial t} = \kappa\left(\frac{\partial^2 u_2}{\partial x^2} + \frac{1}{x}\frac{\partial u_2}{\partial x} + \frac{1}{x^2}\frac{\partial^2 u_2}{\partial \theta^2}\right) \tag{2.30}$$

Similarly, we separate the variables and write the solution as:

$$u_2(x,\theta,t) = U_2(x,\theta)e^{i\omega t} = F(x)\Theta(\theta)e^{i\omega t} \tag{2.31}$$

And plugging equation (2.31) into equation (2.30) yields:

$$\frac{x^2}{F}\frac{d^2F}{dx^2} + \frac{x}{F}\frac{dF}{dx} - \frac{i\omega}{\kappa}x^2 = -\frac{1}{\Theta}\frac{d^2\Theta}{d\theta^2} = \lambda^2 \tag{2.32}$$

where λ is a constant. With the symmetry $\Theta(\theta) = \Theta(-\theta)$, the solution of equation (2.32) is:

$$F(x) = b_x J_\lambda(mx); \quad \Theta(\theta) = b_\theta\, cos(\lambda\theta) \tag{2.33}$$

Note that $\Theta(\theta)$ is a set of orthogonal base within the interval $[0,\pi]$, so that we can construct again the Galerkin equation to satisfy the boundary condition in equation (2.34):

$$u_2(x=R_2,\theta,t) = v\left(x_0 + R_2(1-cos(\theta)), R_2 sin(\theta), t\right)\cdot(\theta<\beta) = g(\theta)e^{i\omega t} \tag{2.34}$$

where β is the opening angle illustrated in figure 2.1. Due to periodicity in θ axis, λ in equation (2.32) is rewritten as an integer j, so that u_2 is expressed as:

$$u_2(x,\theta,t) = \sum_{j=0}^{n} b_j U_{2,j}(x,\theta)e^{i\omega t} = \sum_{j=0}^{n} b_j J_j\,(mx)\,cos(j\theta)e^{i\omega t} \tag{2.35}$$

Based on equation (2.35), the Galerkin equation to satisfy equation (2.34) is written as:

$$\int_0^{\pi} \sum_{j=0}^{n} [b_j U_{2,j}(R_2,\theta) - g(\theta)] \cdot cos(k\theta)d\theta = 0, \quad k = 0,1,2... \tag{2.36}$$

By virtue of the orthogonality of $cos(k\theta)$ over $[0,\pi]$, solution of b_j can be calculated by:

$$b_j = \frac{2}{\pi}\frac{\int_0^{\pi} g(\theta)cos(j\theta)d\theta}{J_j\,(mR_2)} \tag{2.37}$$

Finally, the average temperature of drum 1 $U_{1,avg}$, bridge V_{avg}, and drum 2 $U_{2,avg}$ are given by:

$$\begin{aligned} U_{1,avg} &= \frac{1}{R_1}\int_0^{R_1} U_1(x)x\,dx \\ V_{avg} &= \frac{1}{x_0 y_0}\int_0^{y_0}\int_0^{x_0} V((x,y)\,dxdy \\ U_{2,avg} &= \frac{2}{\pi R_2^2}\int_0^{\pi}\int_0^{R_2} U_2(x,\theta)x\,dxd\theta \end{aligned} \tag{2.38}$$

Hence, an analytical model describing temperature distribution in a dumbbell resonator is established, with three domains: $u_1(x,t)$ for drum 1, $v(x,y)$ for bridge, and $u_2(x,\theta,t)$ for drum 2, and an illustrative result is plotted in figure 2.13. Noticeable noise at low frequencies in the real part and strong noise at low frequencies can be observed, despite a clear thermal signal for all three graphs, and further investigation is presented in section 3.3.

Additionally, a location of readout can be incorporated in this model, as the red laser also has a normal distribution in space. This is realised by adding a weight function to the average temperature in equation (2.38):

$$W(x.y) = e^{-\frac{(x-x_r)^2+(y-y_r)^2}{R_0^2}} \tag{2.39}$$

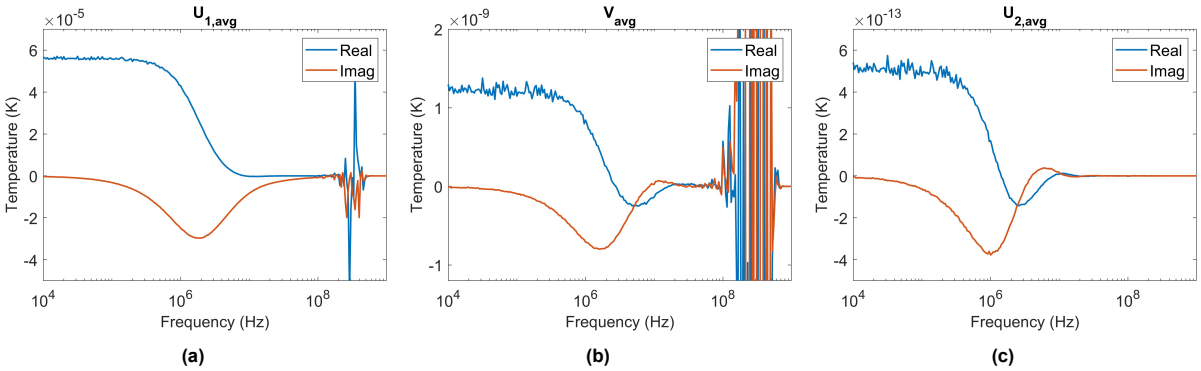

Figure 2.13: Analytical calculation of: (a) $U_{1,avg}$, (b) V_{avg}, and (c) $U_{2,avg}$, with parameters same as in figure 2.11

where x_r and y_r are coordinates of readout position, and R_0 is a constant. Hence, taking readout at drum 2 as example, results picked up at $(x_r,\ y_r)$ become:

$$U_{2,avg,r} = \frac{2}{\pi R_2^2} \frac{\int_0^{\pi} \int_0^{R_2} U_2(x,\theta) W(xcos(\theta), xsin(\theta)) x \, dx d\theta}{\int_0^{\pi} \int_0^{R_2} W(xcos(\theta), xsin(\theta)) x \, dx d\theta} \tag{2.40}$$

3

Results

This chapter presents the results of three approaches described in the previous chapter: optomechanical experiments, COMSOL simulation, and analytical calculation. A comparison of all three method is also conducted. More importantly, parameters in the COMSOL and analytical models are tuned in an effort to explain the variation in experiments, and to visualise the impact of dumbbell dimensions.

3.1. Extracting thermal time constant

Based on experiments described in section 2.2, we try to locate the thermal signal and thus obtain the four thermal time constants τ_{11}, τ_{12}, τ_{21}, τ_{22}, for a dumbbell resonator. Broadly speaking, there are four types of measurement results we can see: (1) the most ideal one, with a clear thermal signal at low frequency separated from the fundamental resonances in high frequencies, as shown in figure 3.1a; (2) the thermal signal is coupled with the fundamental resonance, without a clear ”valley” in the imaginary part, often stemming from a small thermal time constant, as shown in figure 3.1b; (3) thermal signal is clear, but resonance is of small amplitude or absent, usually a fluctuation at high frequencies that resembles simulation in figure 2.11c can be noticed, as shown in figure 3.1c; (4) amplitude of signal is too small that noises cloud the thermal signal, as shown in figure 3.1d. In general, type 1 and 2 are the most common in measurement, therefore the following contents address the curve fitting performance for those two types.

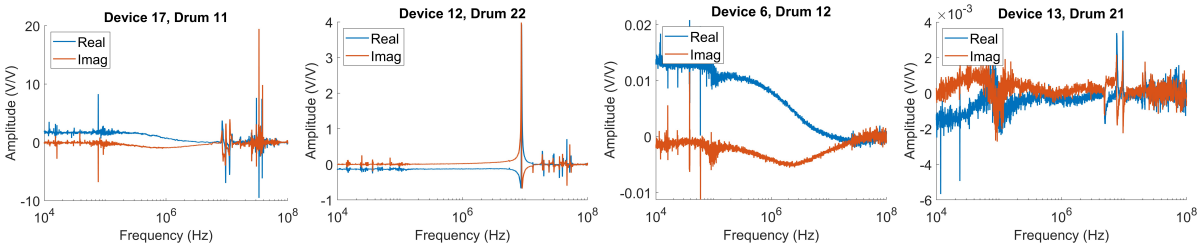

(a) Type 1 **(b)** Type 2 **(c)** Type 3 **(d)** Type 4

Figure 3.1: Four types of measurement results

To extract those τ from the measured and calibrated signal z_ω, we borrow the models mentioned in section 2.2. For the first and the third type, we can obtain the τ by directly fitting equation (3.1) with an adjusted R^2 of 0.70 to 0.99, thanks to a clear thermal signal. Meanwhile, some distortion and noise are present in low frequencies, especially from 10 kHz to 100 kHz. That is because calibration, despite the same input of laser controllers, can still vary due to different temperature and moisture, optics alignment in the setup, and noise from the vacuum pump. Additionally, though a τ can be extracted, type 3 can never give an ideal fit for equation (3.1), as at high frequencies the imaginary part rises above zero.

$$\text{Model 1} : z_\omega = \frac{A_1}{1 + i\omega\tau} + A_2 \tag{3.1}$$

However, curve fitting for type 2 measurement is more tricky. Theoretically, equation (3.2) describes the behaviour of coupled thermal signal and fundamental resonance, but in practice, this model yields the worst fitting, leaving the largest gap between fitted curves and data, as seen in figure 3.3a and figure 3.3b. In particular, the location of the valley (thermal signal) in figure 3.3b differs in the fitted curve, and the gap is even larger at higher frequencies or near resonances. This inspires us to come up with term linear to ω in lieu of A_2 so that this gap can be narrowed, as shown in equation (3.3).

$$\text{Model 2} : z_\omega = \left[\frac{A_1}{1 + i\omega\tau} + A_2\right] \frac{1}{-\omega^2 m_k + i\omega c_k + 1} \tag{3.2}$$

$$\text{Model 3} : z_\omega = \left[\frac{A_1}{1 + i\omega\tau} + (a + bi)\omega + c + di\right] \frac{1}{-\omega^2 m_k + i\omega c_k + 1} \tag{3.3}$$

To compare the three models and decide which one to trust, we extract thermal time constant τ_{m-p} with model p, and introduce coefficient of determination $R^2_{adj,p}$, which is defined as:

$$R^2_{adj,p} = 1 - (1 - R^2_p)\frac{n-1}{n-v-1}, \quad p = 1, 2, 3 \tag{3.4}$$

where v is number of variables, n is number of data points, and R^2_p is expressed as:

$$R^2_p = 1 - \frac{\sum_{i=1}^{n} |y_i - y_{fit,i}|^2}{\sum_{i=1}^{n} |y_i - y_{mean}|^2} \tag{3.5}$$

where y_i is the $i-$th data point, $y_{fit,i}$ is the $i-$th point in fitted curve, and y_{mean} is the mean value of all y_i. Meanwhile, we also observe in graphs if the thermal signal is well represented by the fitted curve.

Starting with model 1, we trust its fitting results for type 1 measurement, as it always demonstrates a thermal signal overlapping the measured data, with a $R^2_{adj,1}$ often over 0.9, as plotted in figure 3.2a. Whereas model 1 is less trustworthy when it comes to measurement type 2, as shown in figure 3.2b. When model 1 creates a thermal signal, there is no reference in measured data, despite a good (but less optimal than fitting of type 1 data) $R^2_{adj,1}$ just below 0.8. Additionally, τ extracted here is more susceptible to the fitting frequency range $[f_b, f_t]$: when f_t approaches the resonance frequency, the thermal signal location also advances toward it, making τ fluctuating up to 30%. Hence, we determine f_b to be 1.65E5 Hz to avoid interference in low-frequency noises and calibration, and to set f_t in all curve fittings of model 1 as equation (3.6) with constant $\alpha = 27$ for a same regime in fitting.

$$f_t = f_0 - \alpha\frac{f_0}{Q} \tag{3.6}$$

Table 3.1: Comparison of three curve fitting models

Measurement	Type	$\tau_{m-1}\,(s)$	$R^2_{adj,1}$	$\tau_{m-2}\,(s)$	$R^2_{adj,2}$	$\tau_{m-3}\,(s)$	$R^2_{adj,3}$
Device 5, drum 21	1	1.6430E-7	0.9715	3.3834E-7	0.3667	1.5782E-7	0.9723
Device 14, drum 11	1	1.0863E-7	0.9401	2.5584E-7	0.1343	1.0718E-7	0.8715
Device 16, drum 21	2	1.0144E-7	0.7324	1.3824E-7	0.8211	7.6083E-8	0.9762

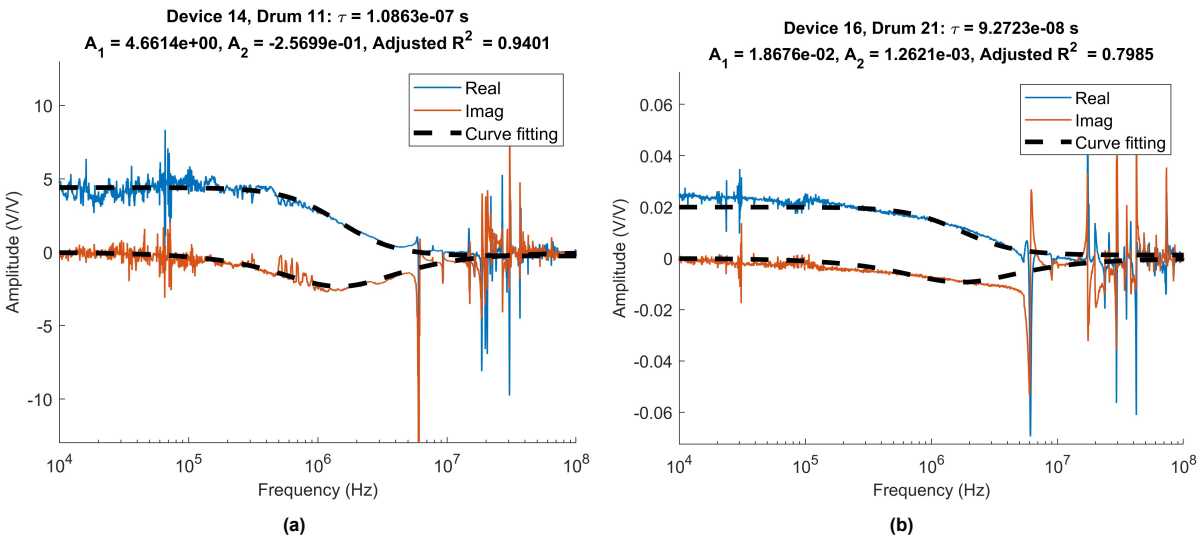

Figure 3.2: Curve fitting with model 1: (a) type 1 measurement, device 14, drum 11; and (b) type 2 measurement, device 16, drum 21

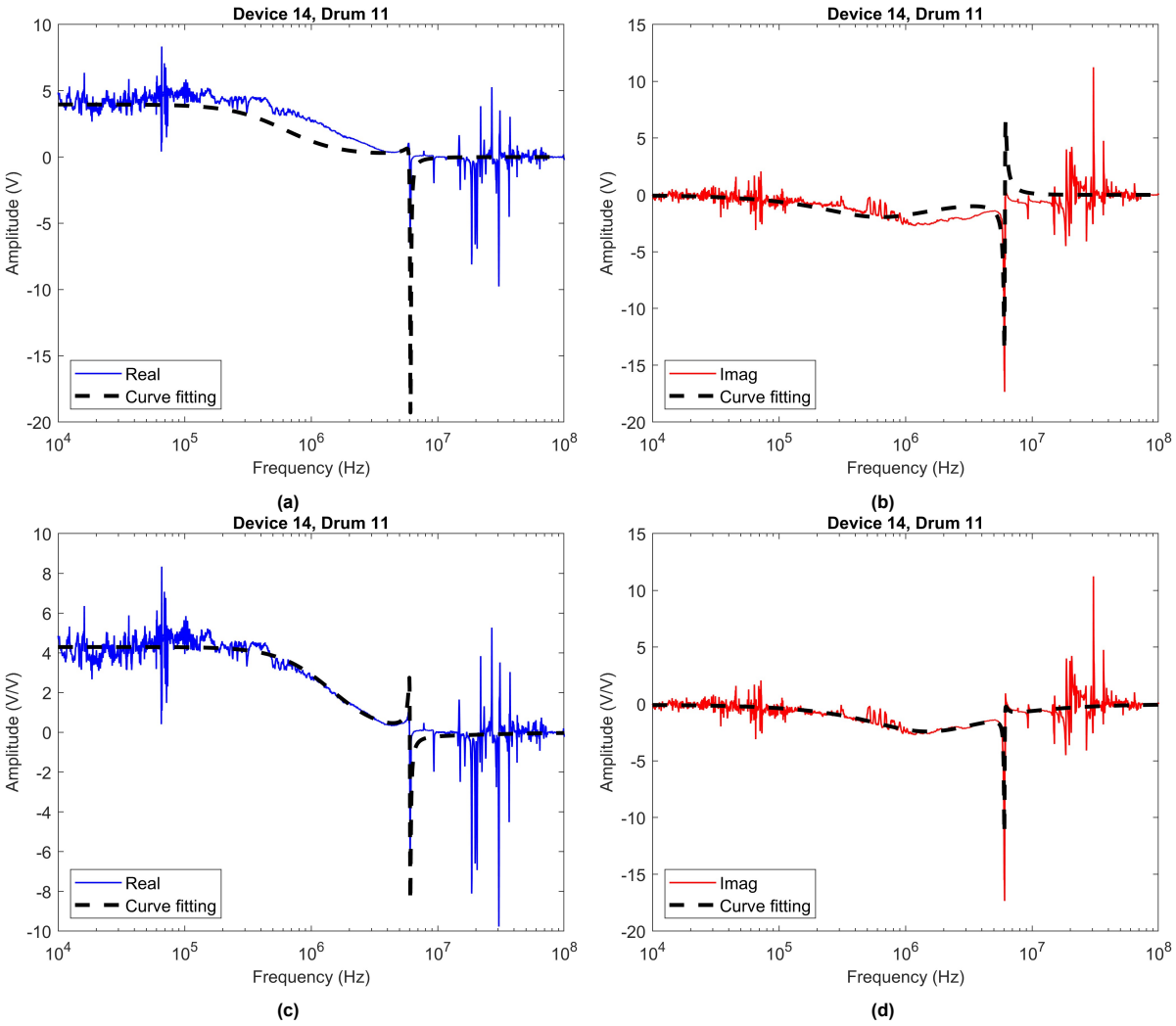

Figure 3.3: Curve fitting of type 1 measurement, device 14, drum 11: (a) real part, by model 2; (b) imaginary part, by model 2; (c) real part, by model 3; (d) imaginary part, by model 3.

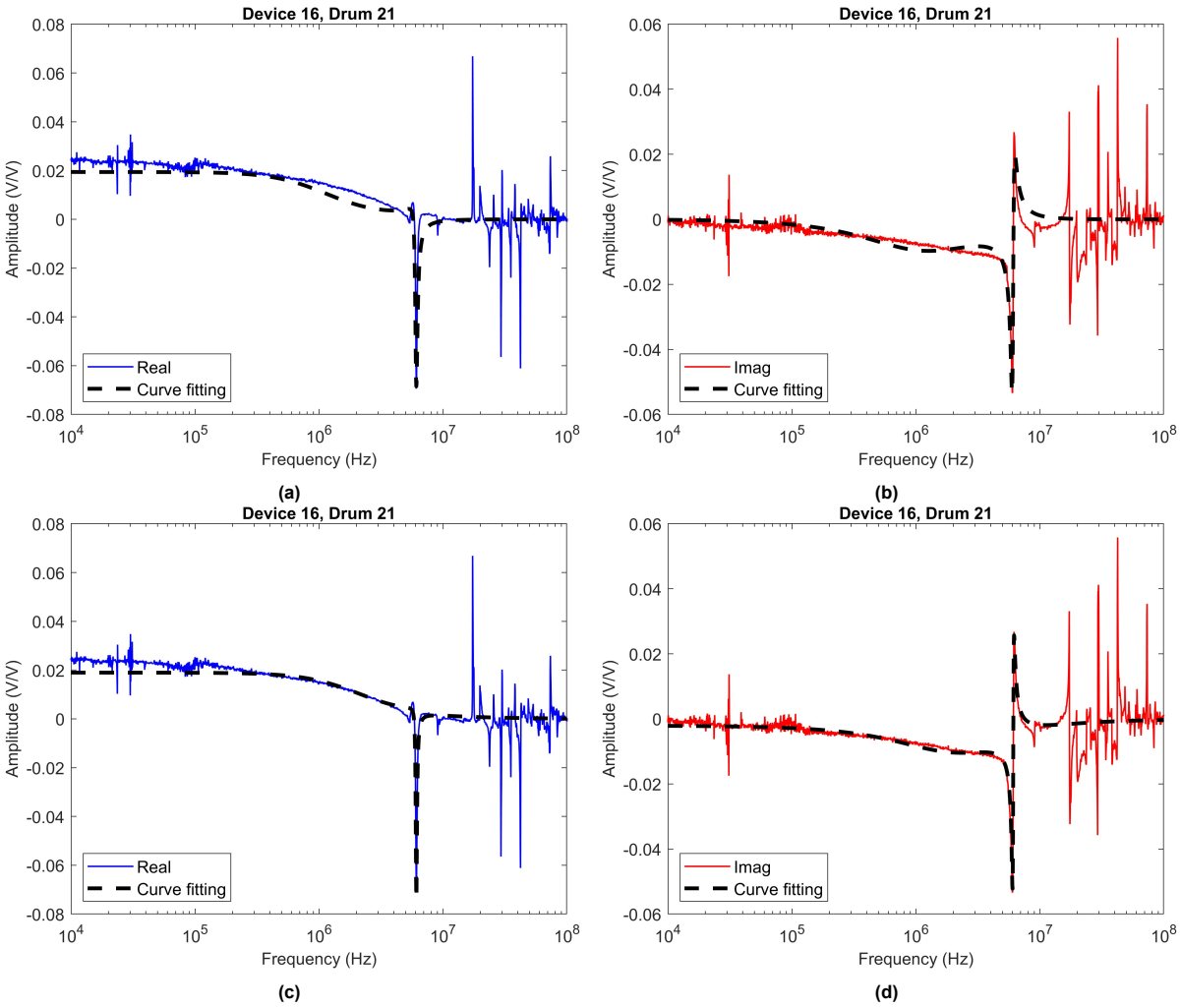

Figure 3.4: Curve fitting of type 2 measurement, device 16, drum 21: (a) real part, by model 2; (b) imaginary part, by model 2; (c) real part, by model 3; (d) imaginary part, by model 3.

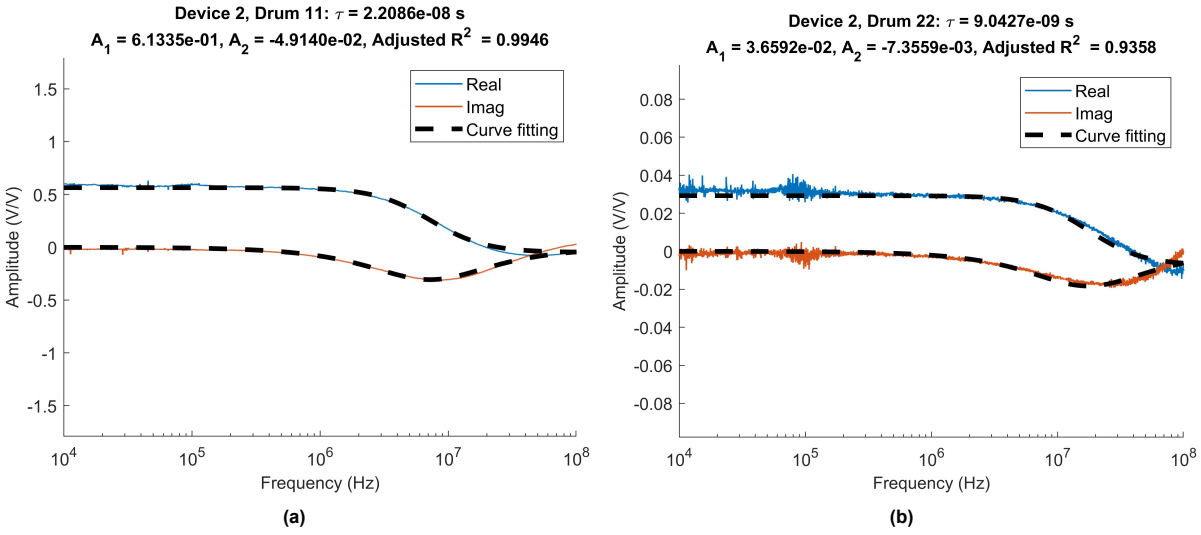

Figure 3.5: Measurement of device 2: (a) drum 11; (b) drum 22, both type 2 data, fitted with model 1.

Table 3.2: Measured thermal time constants of all devices

Device	Model	$\tau_{11,exp}(s)$	$\tau_{12,exp}(s)$	$\tau_{21,exp}(s)$	$\tau_{22,exp}(s)$
1	1	2.6375e-07	2.1388e-07	1.5819e-07	1.6081e-07
3	1	1.0505e-07	1.2239e-07	4.0851e-07	1.5305e-07
4	3	1.2438e-08	2.6259e-07	1.4728e-07	1.6310e-08
5	1	1.2025e-07	1.4615e-07	1.6430e-07	8.5135e-08
7	1	4.7572e-08	7.7288e-08	1.4926e-07	4.3813e-08
8	3	1.8486e-08	7.1143e-08	1.0098e-07	2.2348e-08
9	3	1.4690e-07	6.7254e-08	1.0214e-07	2.2126e-08
10	3	7.1570e-08	1.1059e-07	6.8182e-08	1.8433e-08
11	3	1.9230e-08	3.0244e-08	6.2925e-08	1.5042e-08
12	1	1.0553e-08	5.1595e-08	3.2689e-08	2.6525e-08
14	3	3.3940e-08	4.1235e-08	6.7606e-08	3.2626e-08
15	1	9.1293e-08	1.6379e-07	1.1522e-07	1.1306e-07
16	3	1.8000e-08	7.2759e-08	3.0030e-08	2.8965e-08
17	3	2.6377e-08	5.2779e-08	7.6083e-08	3.3492e-08
18	1	1.8010e-07	5.3910e-08	1.3615e-07	1.5050e-07
19	1	1.8663e-08	1.2778e-07	4.1844e-08	2.9159e-08

To compare the performance of model 2 and model 3, we again use type 1 data. We extract τ_{m-1} with model one, and τ_{m-2} and τ_{m-3} should be close to τ_{m-1}. Taking device 14, drum 11 measurement as example, τ_{m-3} is much closer to τ_{m-1}, with a 1.3% discrepancy compared to a 235.5% difference from τ_{m-2}. A much higher $R^2_{adj,p}$ is also recorded for model 3, as listed in table 3.1. Fitting in figure 3.3 too agrees with the statistics, with a much better overlapping of data and fitting curves using model 3.

Finally, we move on to type 2 data, using model 2 and 3, as shown in figure 3.4. Both model can capture the resonance, while model 3 is much better tracking the data before the resonance, exhibiting a higher $R^2_{adj,3}$ than $R^2_{adj,1}$ and $R^2_{adj,2}$. Model 3 is also more robust compared to model 2, for $R^2_{adj,3}$ is never below 0.76, and is mostly over 0.95 if the resonance is well identified.

There are two remaining issues in extracting those τ. First, the reason why model 3 performs better than model 2 in fitting is unclear, since theoretically the coupling term $(a+bi)\omega+c+di$ in equation (3.3) should have been inversely proportional to ω^a (a is an integer depending on frequency, see appendix A). Second, device 2 and 6 are not included, due to their type 3 measurement of drum 11 and drum 22, as illustrated in figure 3.5. The imaginary part goes up above zero while the real part drops below zero around 100 MHz, and the fitting curve of model 1 is slightly off the thermal signal. Moreover, the facility only allow measurement up to approximately 120 MHz, so this phenomenon of crossing real and imaginary part is not well captured, and thus model 1 is not considered a reasonable model to do curve fitting.

In conclusion, for type 1 and 3 measurement, model 1 is employed to extract its thermal time constant, while for type 2 measurement, model 3 is used. Following this guideline, thermal time constants of 16 devices (see table 2.1) are extracted and presented in table 3.2, each with a subscript "exp".

3.2. Tuning COMSOL model

Eventually, we want to study the relationship between thermal time constant and dumbbell sizes, which is characterised by R_1, R_2, x_0, and y_0, as introduced in figure 2.1. However, it is time-consuming to prepare samples for all four variables, let alone divergence of samples. Hence, a 3D COMSOL model is built to investigate how τ depends on some variables, and what play the key role in the variations in experimental τ.

First, the convergence of a 3D circular resonator model is tested against a 2D axisymmetric model created and verified by Liu[31]. Thermal amplitude A_{th} and thermal time constant τ, as seen in model 1 in equation (3.1), ought to be extracted to quantify the convergence. The extracted τ fluctuates with A_{th}, so the valley location is calculated instead. This location refers to the thermal signal, i.e. the frequency

where the imaginary part reaches the minimum. As depicted in figure 3.6a, the valley locations of two models are invariant with mesh sizes, while A_{th} of the 3D model also approaches to the 2D model as mesh sizes become smaller. Given the negligible discrepancy in A_{th} and valley location, w conclude that the 3D circular resonator model is converging and valid.

$$\begin{aligned}\Delta\tau_+ &= \left|\frac{1}{2\pi f_\tau} - \frac{1}{2\pi(f_\tau + \Delta f_\tau)}\right| = \frac{1}{2\pi}\left|\frac{1}{f_\tau} - \frac{1}{f_\tau 10^d}\right| = \frac{1}{2\pi f_\tau}\cdot\frac{10^d - 1}{10^d} \\ \Delta\tau_- &= \left|\frac{1}{2\pi f_\tau} - \frac{1}{2\pi(f_\tau - \Delta f_\tau)}\right| = \frac{1}{2\pi}\left|\frac{1}{f_\tau} - \frac{1}{f_\tau 10^{-d}}\right| = \frac{1}{2\pi f_\tau}\cdot(10^d - 1)\end{aligned} \tag{3.7}$$

$$\frac{\Delta\tau_+}{\tau} = \frac{10^d - 1}{10^d}; \quad \frac{\Delta\tau_-}{\tau} = 10^d - 1; \tag{3.8}$$

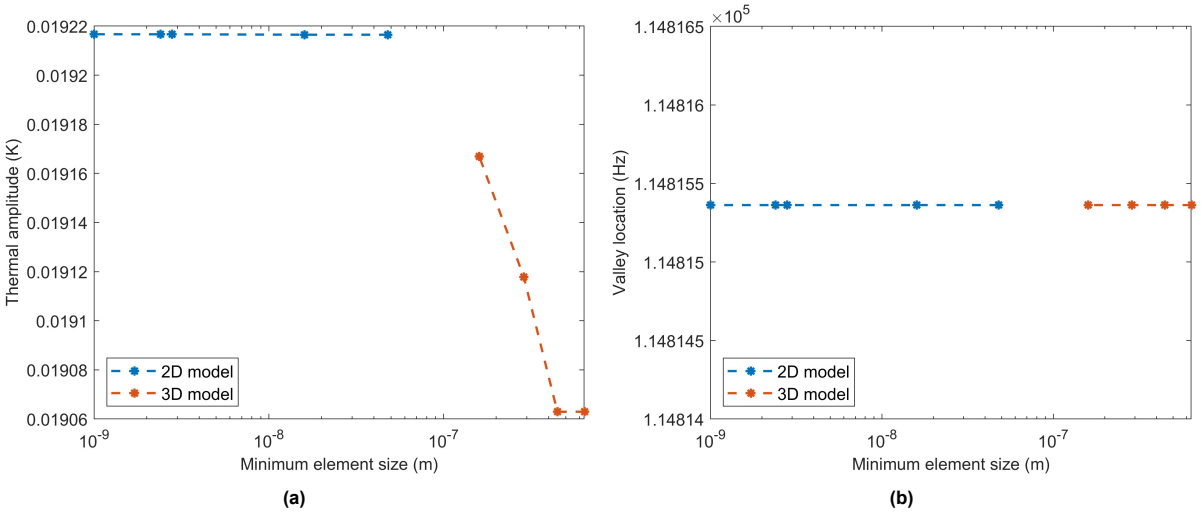

Figure 3.6: Convergence plots, minimum element size against: (a) thermal amplitude A_{th}; (b) location of thermal signal, i.e. the minimum of the imaginary part.

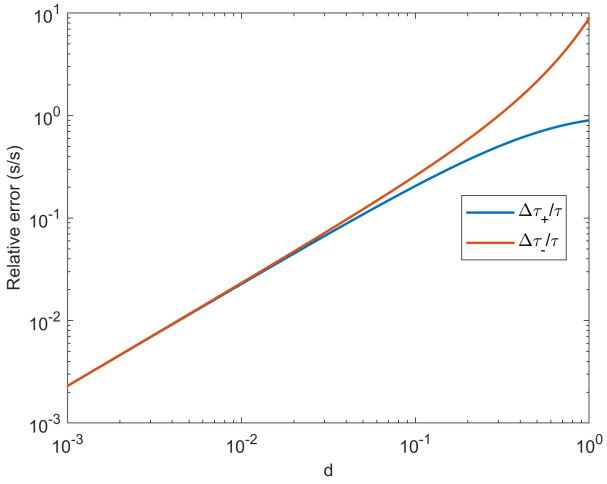

Figure 3.7: Relative error in thermal time constant caused by using valley location, plotted against d, which indicates a d of 0.01 would suffice the precision of τ.

Additionally, to extract τ, valley location is proffered when it comes to drum 12 or drum 21 of simulation and analytical model. As seen in section 2.4 and section 2.5, those curves resemble type 2 data in

section 3.1, which means curve fitting with model 1 is no longer appropriate. However, to use valley location instead of curve fitting for τ must lead to some error, but such error is tolerable if the frequency resolution is sufficient. Assume the actual valley location is at f_τ, whereas we obtain $f_\tau + \Delta f_\tau$, then the error between the real thermal time constant τ and the extracted one is $\Delta\tau$, as written in equation (3.7). In simulation, frequency sweep is determined by an array of geometric sequence f_i, where common ratio $10^d = \frac{f_{i+1}}{f_i}$. Typical values of d are from 0.001 to 0.02. According to such settings, the maximum relative error $\frac{\Delta\tau}{\tau}$ is obtained by setting Δf_τ equals to $(10^d - 1)f_\tau$ or $(1 - 10^{-d})f_\tau$. In this way, $\frac{\Delta\tau}{\tau}$ becomes a function of of d, as presented in equation (3.8) and plotted in figure 3.7. If we expect the relative error to be smaller than 0.1, then $d = 0.02$ would meet this requirement.

After settling the mesh size and frequency resolution, we investigate the settings of actuation and readout laser. As Liu[32] found out, the actuation amplitude do not affect thermal time constant, we can also reason that τ remain unaffected by readout amplitude. Therefore, equation (3.9) is borrowed from section 2.5 to define the actuation power $P(x,t)$ and readout weight function $W(x,y)$. First, we tune r_0 in $P(x,t)$, as illustrated in figure 3.8a, to examine the corresponding shift in τ_{11} and τ_{12}. In addition, the thermal time constants extracted with weight function $W(x,y)$ are calculated as well, called τ_{11c} and τ_{12c}. All four time constants are plotted in figure 3.8b. Smaller laser spots, i.e. smaller r_0, leads to larger thermal time constants, since it takes longer time to heat up the membrane for smaller r_0. The variation in τ_{11} due to r_0 is negligible, registering within 5%, and thus can originate from errors in valley location, as defined in equation (3.8). While variation in τ_{12} is almost 15%, and that means the variation mainly stems from heat transfer in bridge and drum 2. Variation saturates as r_0 go beyond 4 μm, which coincides with less variation in actuation power: difference between curves of $r_0 = 8\mu m$ and $r_0 = 4\mu m$ compared to that between curves of $r_0 = 4\mu m$ and $r_0 = 1\mu m$ is more distinct. As for $W(x,y)$, R_0 is set to $4.0\mu m$, and $W(x,y)$ assign larger weight to area closer to the centre of drum 1 or drum 2, Since the temperature distribution can be expressed by a series of Bessel function $J(mx)$ (see section 2.5), when x grows, the first valley location in the imaginary part of $J(mx)$ registers at a smaller frequency, and that means a larger τ for larger x. This complies with the physical meaning of τ: longer time duration is required for heat to transfer from the centre to area of larger x. Despite a increase of τ with $W(x,y)$, such growth is marginal if we calculate the ratio, as detailed in figure 3.8c. The maximum growth is within 9%, and the ratio is closer to 1 for τ_{12}/τ_{12c}. There are some odd points go slightly above 1 (at 1.02), but this probably comes from error of valley location again. Hence, it is not necessary to take into account $W(x,y)$ if the readout location is at the centre.

$$\begin{aligned} P(x.t) &= H_0 e^{-\frac{x^2}{r_0^2}} e^{i\omega t} \\ W(x.y) &= e^{-\frac{(x-x_r)^2+(y-y_r)^2}{R_0^2}} \end{aligned} \tag{3.9}$$

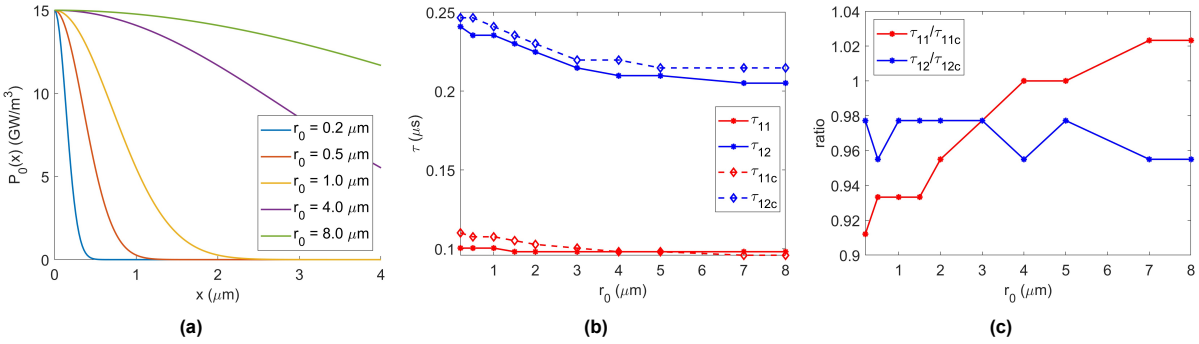

Figure 3.8: Tuning actuation laser spot: (a) power of laser spot in space with different shape parameter r_0; (b) values of resultant thermal time constant, with and without a weight function in readout; (c) ratio between thermal time constants with and without a weight function in readout.

Nonetheless, when readout locates away from the centre, i.e. $x_r \neq 0$ or $x_r \neq 0$, then the shift of the thermal time constant can be significant. The same should be reasoned for actuation location. We fix

R_0 to $4.0\mu m$ and r_0 to $0.5\mu m$, and vary x_r and y_r in $W(x, y)$ for actuation and readout to see how large the shift of τ is.

To explore the influence of actuation location, the red laser spot is moved along axis x_{r1} from -3μm to 3μm, and then along axis y_{r1} from -3μm to 3μm, as drawn in top figure 3.9a. The same is conducted for the blue laser, as drawn in bottom figure 3.9a, and the results are summarised in figure 3.9c. Moving actuation or readout location has limited affect on τ_{11}, with the largest fluctuation of merely 2.3%. For τ_{12}, the shift is more observable. The curve of τ_{12} with varying y_r is symmetrical against x_r = 0. The largest variance in figure 3.9b is found in τ_{12} with a fixed y_r = 0, and the corresponding curve is almost linear from $-1\mu m$ to $3\mu m$ (see the yellow line). Such linear relationship matches the time needed for the heat to travel from the actuation to the readout location. This is again evidenced by moving readout away from actuation location: τ_{12} with fixed y_r drops almost linearly in figure 3.9c. Similarly, changing readout location exerts less influence on τ_{11} compared to τ_{12}. Hence, positions of actuation and readout along x_r1 and x_r2 axis matter, bringing about shifts up to 9% and 31%, respectively. In comparison, deviance along y_r1 and y_r2 is negligible, always within 3%. Additionally, the linear relationship between τ_{12} and x_r is not valid when $x_r < -2\,\mu m$. This location is close to the bridge part, where some of the readout is off the membrane, thus distorting τ_{12}.

From this point on, we can combine the influence of actuation and readout location, and calculate the largest and smallest resultant thermal time constant $\tau_{12,max}$ and $\tau_{12,min}$, then compare them to τ_{11c} and τ_{12c}. The largest τ_{12} should be obtained by actuation at $(x_{r1} = -3,\, y_{r1} = 0)\ \mu m$ and readout at $(x_{r2} = 3,\, y_{r2} = 0)\ \mu m$, while to attain the smallest τ_{12}, actuation is situated at $(x_{r1} = 3,\, y_{r1} = 0)\ \mu m$ and readout is situated at $(x_{r2} = -3,\, y_{r2} = 0)\ \mu m$. As a result, $\tau_{12,max}$ registers 0.3103 μs, 26% larger than τ_{12c}, and the $\tau_{12,min}$ is 40% smaller than τ_{12c}, measuring 0.1485 μs. This means the ratio between $\tau_{12,max}$ and $\tau_{12,min}$ is 2.10, or 0.48 if the denominator and the numerator are switched. These ratios are further utilised in section 3.4.

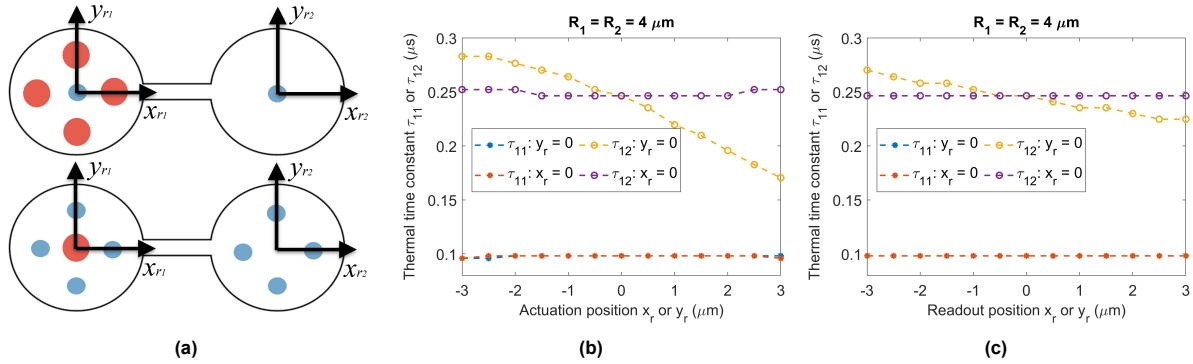

(a) (b) (c)

Figure 3.9: Tuning actuation or readout location in the COMSOL model: simulation setup illustrated in (a). Top of (a): varying location of actuation blue laser and fixed location of readout red laser at the centre of drum 1 and drum 2, and the results shown in (b). Bottom of (a): varying location of readout red laser and fixed location of actuation blue laser at the centre of drum 1, and the results shown in (c). Red or blue laser is moved along axis x_{ri} or x_{ri} ($i = 1, 2$) defined in (a).

So far, we are using this COMSOL model to test variations rooted in optomechanical measurement, and the next step is to test how material properties can change the thermal time constant. For this matter, in following simulations, r_0 is fixed to $0.5\mu m$ and R_0 $4.0\mu m$, actuation and readout locations have no deviation from the drum centre, and $W(x, y)$ is not involved when acquiring thermal time constants.

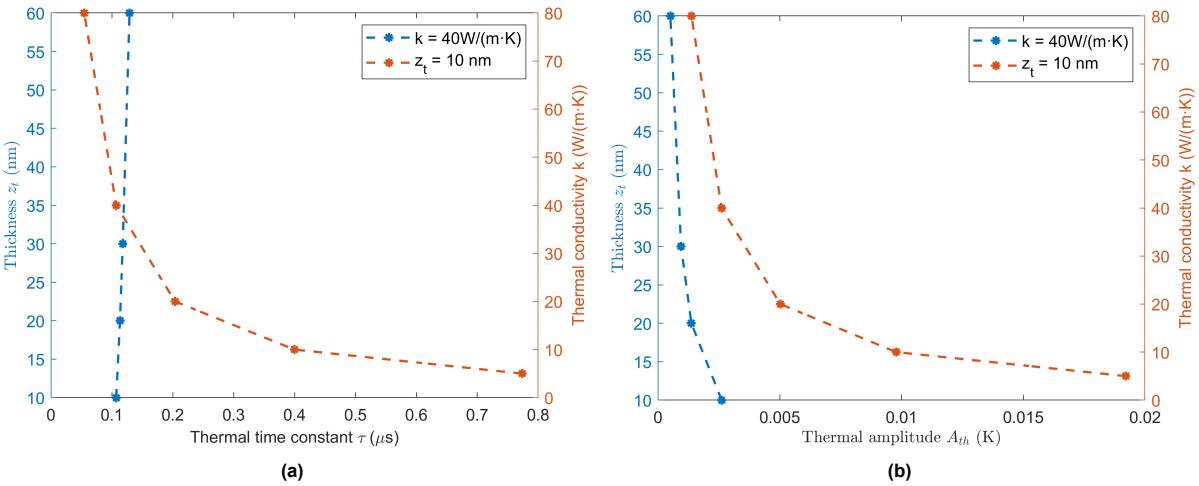

Figure 3.10: Affect of material properties on: (a) thermal time constant τ and (b) thermal amplitude A_{th}.

From equation (1.30), we see that thermal conductivity k and specific heat C_v play a key role in τ value, if material density is considered constant. Apart from that, thickness also matters if it is not much smaller than resonator dimensions. Accordingly, we tune the thermal conductivity and membrane thickness in the COMSOL model, and plot how τ and A_{th} varies in figure 3.10. Large thickness contributes to a larger τ due to more time needed for heat to propagate in the thickness direction, which is the case in figure 3.10a. Thickness of our samples is found between 8 nm to 60 nm, and that would result in a shift in τ registering around 20%. This shift is dwarfed by that caused by thermal conductivity, measuring a 1418% difference. The curve also agrees with equation (1.30), which indicates a inverse proportional relationship between τ and k. The range of thermal conductivity is determined by experiments on monolayer MoS_2 [35, 53, 28, 22], and considering thickness variation in our samples, such range of k is conservative. Similarly in A_{th}, thermal conductivity brings about a much larger variation, as this property is directly linked to heat transfer. Hence, as a material property, thermal conductivity is the dominant factor in determining τ.

In recapitulate, the major factors of variance in thermal time constant are actuation and readout location along x_r axis, and thermal conductivity of the membrane.

3.3. Temperature distribution

The COMSOL model serves as a robust tool to study how some parameters or properties shift thermal time constant, but it is still a black box that only the equivalent input and output are clear to us. Therefore, we use the analytical model to better understand the physics and mathematics of temperature distribution.

First, the analytical model should converge to the simulation in COMSOL, as they both solve the heat equation with the same boundary condition. The solution of temperature distribution in drum 1 is copied from section 2.5 and written in equation (3.10), and in theory the more Bessel functions we include, the more closer the analytical and simulation models are. Thus, normalised average temperature of drum 1 $U_{1,avg}$, bridge V_{avg}, and drum 2 $U_{2,avg}$ are calculated when $n = 3$, 5, and 8. These curves are compared with the normalised average calculated by the COMSOL model, as displayed in figure 3.11. All those curves are normalised by dividing a ratio γ defined in equation (3.11), where $f_1 = 1$ kHz and $f_1 = 10$ kHz. In this way, the real part of the signal at 10 kHz (i.e. the start frequency of plots) is close to 1 Kelvin, then the shape of them can be addressed. For $U_{1,avg}$, $n = 3$ already shows a good overlapping, and improvement by increasing n is marginal. While $n = 8$ yields decent improvement for V_{avg} and $U_{2,avg}$, particularly regarding small fluctuations at high frequencies. However, if the location of the first valley in the imaginary part only is considered, $n = 3$ is sufficient and much more time-saving in calculation.

An obvious drawback that can be observed in figure 3.11 is error around 20 MHz, especially in the solution of bridge V_{avg}. When using Galerkin method to solve for $U_1(x)$ in section 2.5, we used base functions that are not orthogonal to each other in the integration interval, then inverse of a matrix $\mathbf{A}$

need to be calculated in equation (2.18). This matrix $\mathbf{A}$ becomes more baldly scaled when n grows, and is the closest to singular matrix around 20 MHz. Consequently, numeric error, comprising precision in Bessel functions and inverse calculation, become dominant when the amplitude of signal per se is small, as seen in the bridge part. Luckily, such numerical error is attenuated when calculating b_j using orthogonal base in equation (2.37), so that the solution of drum 2 is more smooth.

$$U_1(x) = \sum_{i=0}^{n-1} c_i \left[J_i(mx) - \frac{J_i(mR)}{J_n(mR)} J_n(mx) \right] \tag{3.10}$$

$$\gamma = \int_{f_1}^{f_2} \mathrm{Re}\{z_w(2\pi f)\}\, df \tag{3.11}$$

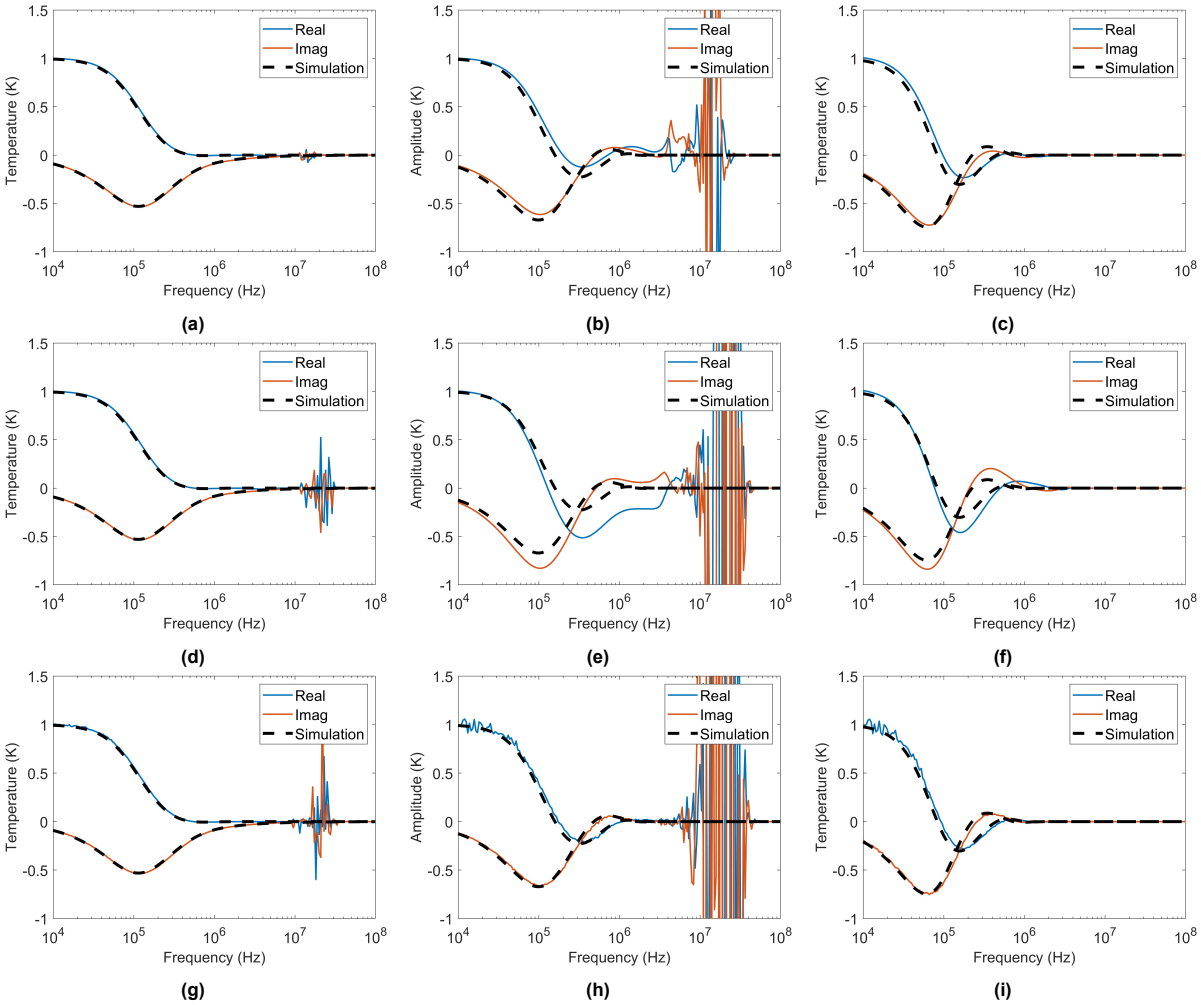

Figure 3.11: Convergence of analytical model and COMSOL simulation model in normalised results, with red and blue lines calculated by analytical model while dotted lines from COMSOL model. (a-c) $n = 3$; (d-f) $n = 5$; (g-i) $n = 8$. Material (graphene) properties for both models are based on settings in literature [32]: thermal conductivity is 5 W/(m^3·K), specific heat is 700 J/(g·K), and density is 3375 kg/m^3.

In figure 3.11, normalised curves calculated by the analytical model and the COMSOL model share a similar shape, but the original ones are of different amplitude, as evidenced by temperature distributions in figure 3.13 and figure 3.12. The analytical model lacks a thickness direction, so it is a 2D model. The COMSOL model's heat source, as introduced in equation (3.9), is set to $H_0 = 1.5\text{E}10$ W/m^3, while in the analytical model, H_0 takes the same amplitude, but the unit of it becomes W/m^2. This raw translation of

heat source from 3D to 2D is one of the reasons why the amplitudes are different. Comparing figure 3.13 and figure 3.12, the COMSOL model in general produces a higher temperature amplitude at 1 MHz. In particular, the bridge and drum 2 of the COMSOL model gives a temperature almost three orders of magnitude higher than that of the analytical model. A prominent difference in the bridge and drum 2 temperature amplitude has to do with the assumption on the boundary condition, which is discussed in section 4.2.

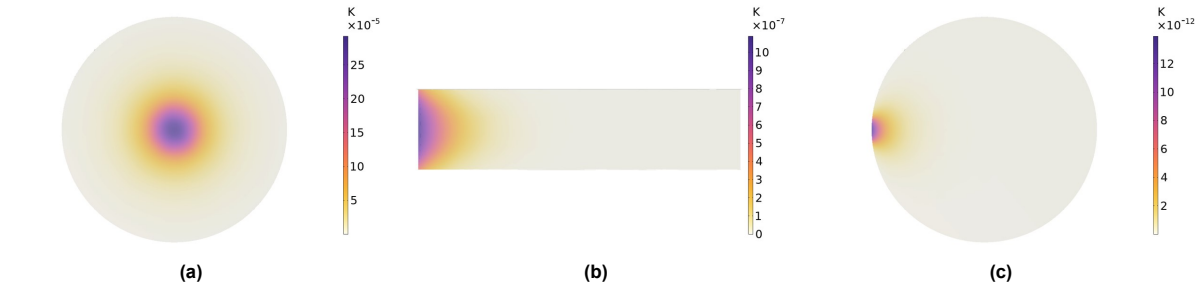

Figure 3.12: Temperature distribution at 1 MHz (absolute values), produced by the COMSOL model: (a) domain drum 1; (b) domain bridge; (c) domain drum 2. Material properties follow figure 3.11.

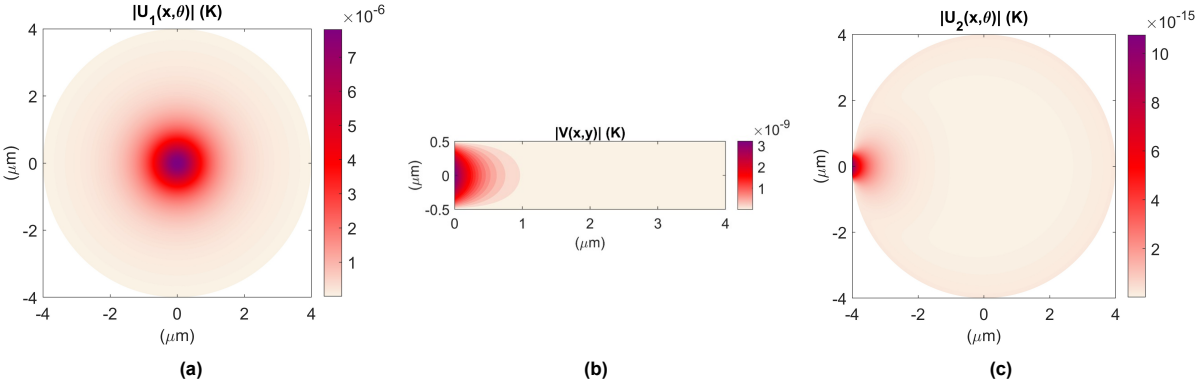

Figure 3.13: Temperature distribution at 1 MHz (absolute values), produced by the analytical model with $n = 8$: (a) drum 1 part; (b) bridge part; (c) drum 2 part. Material properties follow figure 3.11.

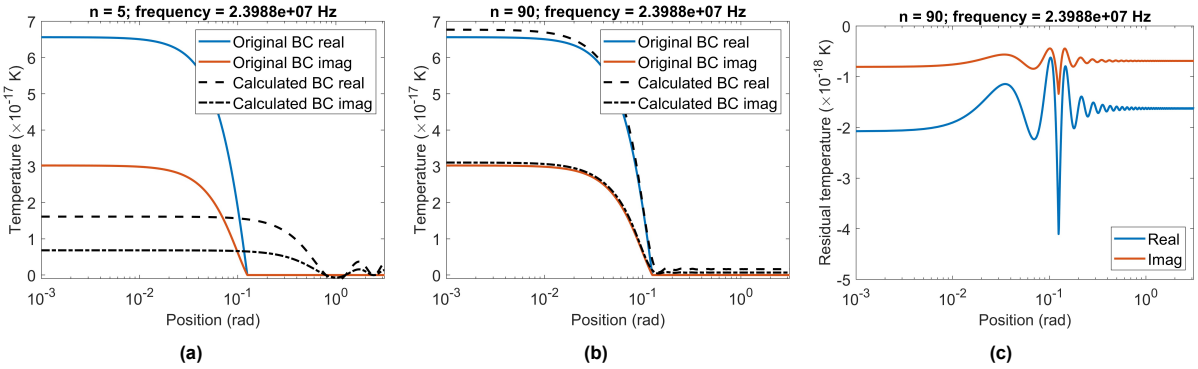

Figure 3.14: Residual on drum 2 boundary condition, using equation (2.34). Convergence towards the actual BC can be observed when comparing: (a) when using 5 cosine functions; (b) when using 90 functions. The residual value is plotted in (c). Position refers to θ defined in figure 2.12.

As for the pattern of temperature distribution, the calculation of the analytical model follows the COMSOL model well. In domain drum 1, the centre features a significantly higher temperature due to the actuation. In domain bridge, the left side features shades of ellipse, which fades out at around 1 μm

along horizontal direction. In domain drum 2, small areas of relatively high temperature are identified on the left side.

In addition, a flaw of the analytical model lies in the satisfaction of boundary condition. In section 2.5, equation (2.36) is applied to satisfy boundary condition equation (2.34). However, this boundary condition is not smooth, and the cosine functions cannot fulfill the boundary condition exactly, always leaving a DC residual. As seen in figure 3.14, the calculated BC converges to the actual one as number of cosine function n increases, and luckily the residual is well over one order of magnitude smaller than the original BC thus tolerable.

Another flaw of the analytical model emerges when thermal conductivity k is higher than 10 W/(m·K). The solution of $U_{1,avg}$ always match for the two models no matter what the k is, as evidenced by the first column of figure 3.15. However, mismatch appears in V_{avg} in the second column when k grows. Even larger discrepancy ensues in the third column of $U_{2,avg}$, particularly in figure 3.15i where k is the highest, at 40 W/(m·K). The reason for such gap is ascribed to the assumption made in section 2.5: (1) the opening of the bridge part exerts trivial impact on the temperature distribution in drum 1. This assumption holds for $U_{1,avg}$, but it might not for V_{avg} or $U_{2,avg}$; (2) in the COMSOL model, temperature at the edge of the dumbbell is not fixed, but that is fixed in the analytical model. The reasons are detailed in section 4.2.

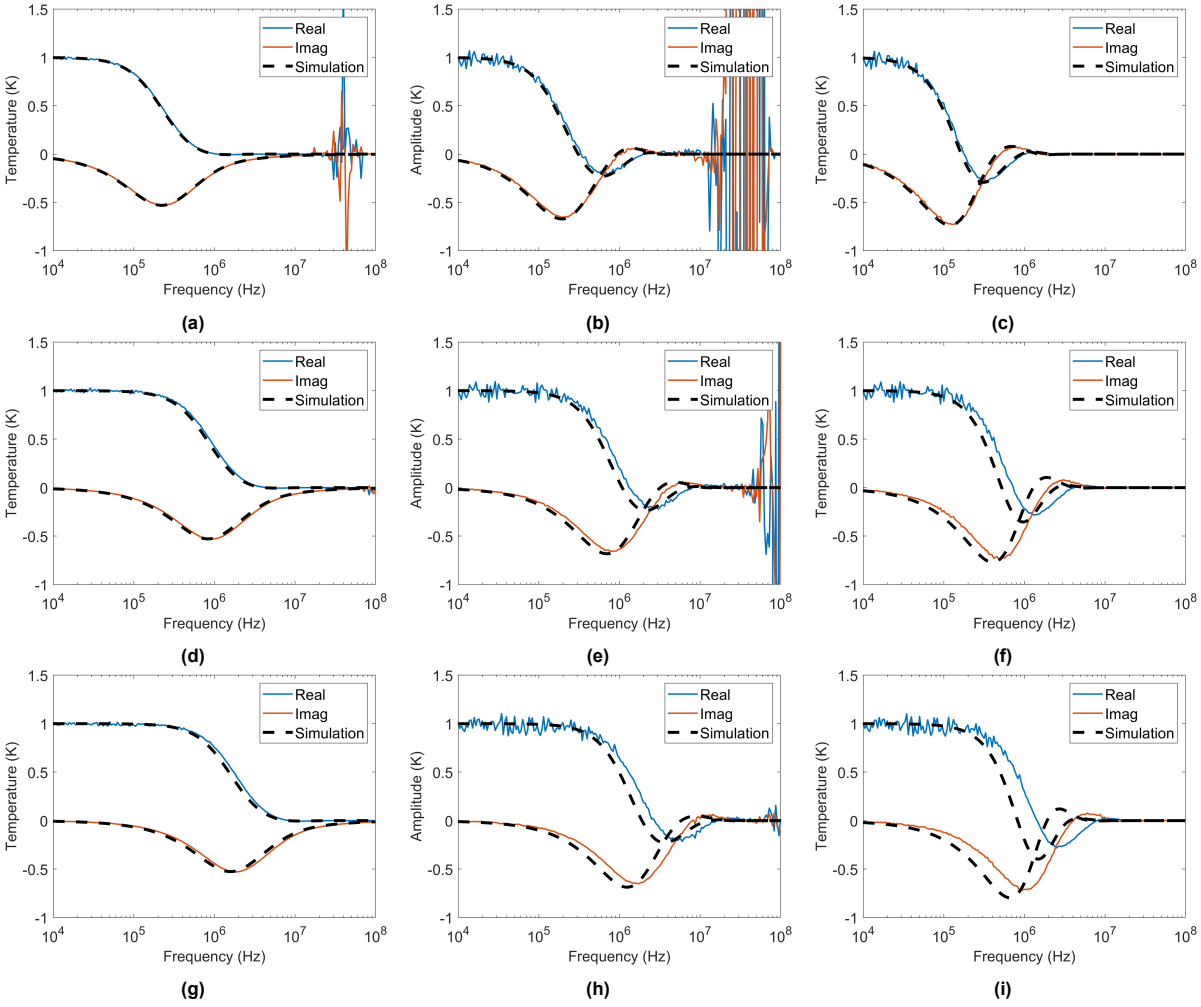

Figure 3.15: Comparison of the analytical model to the COMSOL model with three thermal conductivity values, in terms of average temperature of three domains: drum 1, bridge, and drum2. (a-c) $U_{1,avg}$, V_{avg}, and $U_{2,avg}$ with $k = 5$ W/(m·K); (d-f) the same three averages with $k = 20$ W/(m·K); (g-i) the same three averages with $k = 40$ W/(m·K). Other material (MoS_2) properties for both models are: specific heat is 240 J/(g·K), and density is 5060 kg/m^3.

3.4. Verification with experimental data

In this section, thermal time constants from experiments, COMSOL simulation, and the analytical model are compared. For clarity, subscript "exp", "sim", "ana" are assigned to them, respectively. For example, $\tau_{12,exp}$ denotes thermal time constant τ_{12} derived from experimental data.

The previous section 3.2 and section 3.3 present the results of the COMSOL model and the analytical model, and those two models match each other. This section moves on to explore if these models match the experimental results in section 3.1, so that eventually these models can be employed to explore the τ-dumbbell size relationship.

As revealed in section 3.2, laser location and thermal conductivity both play a significant role in thermal time constant, so large variance is found in experimental data, as detailed in section 3.5. Furthermore, each size of drum has only one or two samples, so it is impossible to directly verify the models with extracted τ in table 3.2. Given this, we need to numerically filter out the disturbance of laser location and thermal conductivity from experiments, and compare the filtered results with the COMSOL or analytical model.

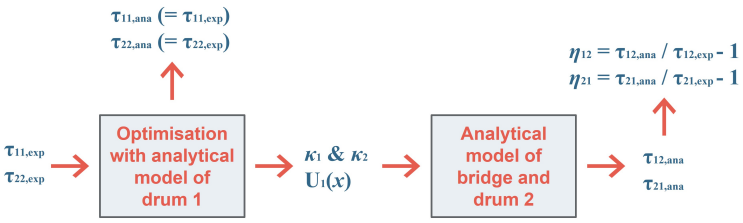

Figure 3.16: Procedure to cancel out the effect of varying thermal conductivity.

$$\kappa_i = \frac{R_i^2}{\mu^2 \tau_{ii}}, \quad (i = 1, 2) \tag{3.12}$$

$$\kappa_{bridge} = \frac{\kappa_1 + \kappa_2}{2} \tag{3.13}$$

$$\eta_{ij} = \frac{\tau_{ij,ana}}{\tau_{ij,exp}}, \quad (i, j = 1, 2) \tag{3.14}$$

First, to tackle the thermal conductivity, a procedure to produce $\tau_{12,ana}$ and $\tau_{21,ana}$ without the effect of thermal conductivity is illustrated in figure 3.16 and explained in the next two paragraphs.

As heat capacity and density are deemed constant for all devices, thermal diffusivity κ_1 and κ_2 for drum 1 and drum 2 are dealt with instead. To acquire κ_1 and κ_2, we align the experimental results of drum 1 and drum 2 with those of the analytical model of drum 1, i.e. making $\tau_{11,ana} = \tau_{11,exp}$ and $\tau_{22,ana} = \tau_{22,exp}$. To do this, equivalent thermal diffusivity κ_1 for drum 1 and κ_2 for drum 2 can be derived by equation (3.12). Note that μ^2, despite being constant, can vary from 5.02 to 5.78[31], so an optimisation algorithm is employed to make sure $\tau_{11,ana}$ is as close to $\tau_{11,exp}$ as possible, and same for $\tau_{22,ana}$ and $\tau_{22,exp}$. We extract $\mu^2 = 5.6564$ for all devices, if an error of 5% is allowed. As for the bridge part, its thermal diffusivity κ_{bridge} is assumed to be the average of κ_1 and κ_2, as stated in equation (3.13). This coarse assumption should lead to some error, but unfortunately there is no experimental data to extract κ_{bridge} directly.

Thereafter, these thermal diffusivity constants, along with temperature distribution of drum 1 $U_1(x)$ are inserted in the analytical model of bridge and drum 2 to calculate $\tau_{12,ana}$ and $\tau_{21,ana}$. In this way, the difference between $\tau_{12,ana}$ and $\tau_{12,exp}$ should mainly stem from deviation of laser location from the drum centre, and the same can be argued for $\tau_{21,ana}$ and $\tau_{21,exp}$. Consequently, the thermal time constants without the influence of thermal conductivity are listed in table 3.3.

Table 3.3: Thermal time constants of all devices calculated by the analytical model

Device	$\tau_{11,ana}(s)$	$\tau_{12,ana}(s)$	$\tau_{21,ana}(s)$	$\tau_{22,ana}(s)$
1	2.6650e-07	3.7818e-07	3.3551e-07	1.5911e-07
3	1.0610e-07	2.2579e-07	4.3023e-07	1.5336e-07
4	1.2573e-08	2.3957e-08	2.5552e-08	1.6271e-08
5	1.1959e-07	1.8268e-07	1.6971e-07	8.5842e-08
7	4.7248e-08	7.9137e-08	7.8412e-08	4.4298e-08
8	1.8632e-08	3.4219e-08	3.5178e-08	2.2196e-08
9	1.4619e-08	2.9710e-08	3.2878e-08	2.2331e-08
10	7.1740e-08	8.7854e-08	6.6033e-08	1.8525e-08
11	1.9408e-08	3.1331e-08	2.9375e-08	1.5135e-08
12	1.0658e-08	2.7775e-08	3.4646e-08	2.6770e-08
14	3.4254e-08	5.6848e-08	5.6326e-08	3.2412e-08
15	9.0719e-08	1.7446e-07	1.8268e-07	1.1421e-07
16	1.7942e-08	3.8537e-08	4.3040e-08	2.9233e-08
17	2.6604e-08	5.1161e-08	5.4068e-08	3.3802e-08
18	1.8101e-07	3.0318e-07	2.8953e-07	1.5195e-07
19	1.8740e-08	4.2538e-08	6.8041e-08	2.9429e-08

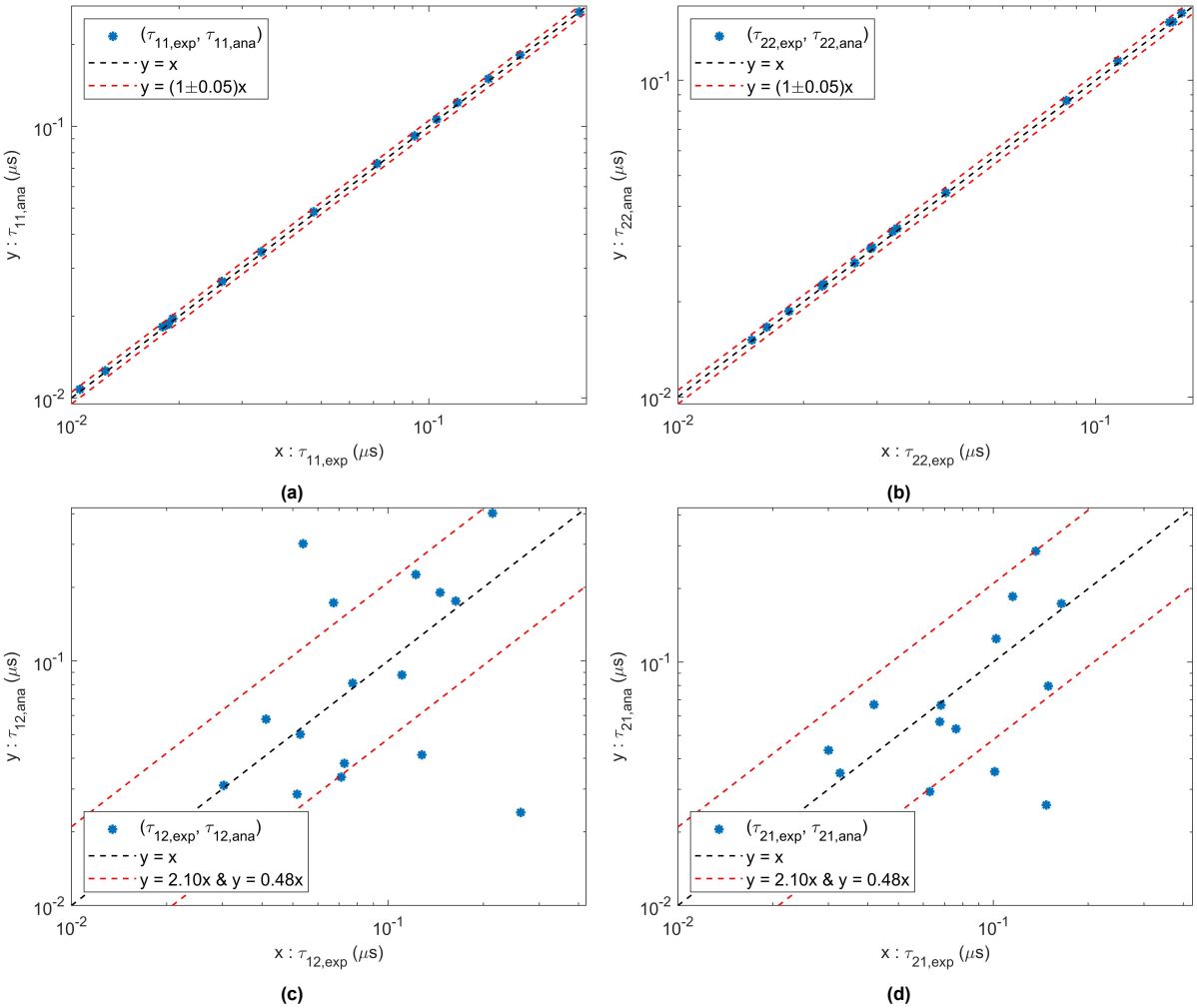

Figure 3.17: Derived thermal time constants without the effect of thermal conductivity. (a) and (b) show desired alignment of $\tau_{11,ana}$ with $\tau_{11,exp}$, and $\tau_{22,ana}$ with $\tau_{22,exp}$, as evidenced by an error bar of $\pm 5\%$. (c) and (d) show large variation in $\tau_{12,ana}$ and $\tau_{21,ana}$, with over 70% data points falling within the error bar. Reasons of such variation is further discussed insection 4.1.

As a result of the aforementioned procedure, the alignment of $\tau_{11,ana}$ and $\tau_{11,exp}$ is plotted in figure 3.17a, while $\tau_{22,ana}$ and $\tau_{22,exp}$ in figure 3.17b. For both alignment, the error is within 5%, as all data points fall with in the lines $y = (1 \pm 0.05)x$. Two similar plots are presented in figure 3.17c and figure 3.17d to compare $\tau_{12,ana}$ with $\tau_{12,exp}$ and $\tau_{21,ana}$ with $\tau_{21,exp}$, respectively. When filtering out the effect of thermal conductivity, the variation should mainly come from deviation of laser location. Theoretically, if deviation of lasers from the centre of a drum is random in space, then the chances of $\tau_{12,exp}$ and $\tau_{21,exp}$ being larger or smaller than the ones measured at the drum centre are the same, so the median of all ratios η_{ij} should be one. In fact, a median of 0.05 is recorded, which is close to one.

As calculated in section 3.2, the ratios among thermal conductivity of various actuation positions range from 0.48 to 2.10. These two ratios form an error bar, as indicated by the dotted red lines. Though a much larger variation can be spotted, over 70% of points are located within the error bar. Such variation is further discussed in section 4.1.

To quantify the difference between results in table 3.3 and experimental data in table 3.2, ratios between those thermal time constants are calculated, as defined in equation (3.14). Since the alignment of $\tau_{11,ana}$ with $\tau_{11,exp}$ and $\tau_{22,ana}$ with $\tau_{22,exp}$ boost desired results (meaning η_{11} and η_{22} close to 0 for all devices), a diagram is drawn only for η_{12} and η_{21}, as seen in figure 3.18a. Two dotted lines of 210% and 48% are drawn, signifying the same error bar in figure 3.17c and figure 3.17d. Those ratio range from 0.09 to 5.60, with only 25% η_{ij} considered closed to 1 (i.e. within 1 ± 0.1 range). For many outliers, for example device 1 and 17, their η_{12} and η_{21} are both much larger than one, while those of device 4 and 8 are much smaller than one.

Large variation is also spotted in the derived thermal diffusivity κ_1 and κ_2, as depicted in figure 3.18b. They span from 4.19E-6 to 4.19E-4 m^2/s. For 11 out of 16 devices the discrepancy between κ_1 and κ_2 registers below 5E-5 m^2/s (see the dotted yellow line), with the largest found in device 12 at 2.5E-4 m^2/s.

In summary, the experimental data exhibits large variation compared to the COMSOL and analytical model, and the reasons are discussed in section 4.1.

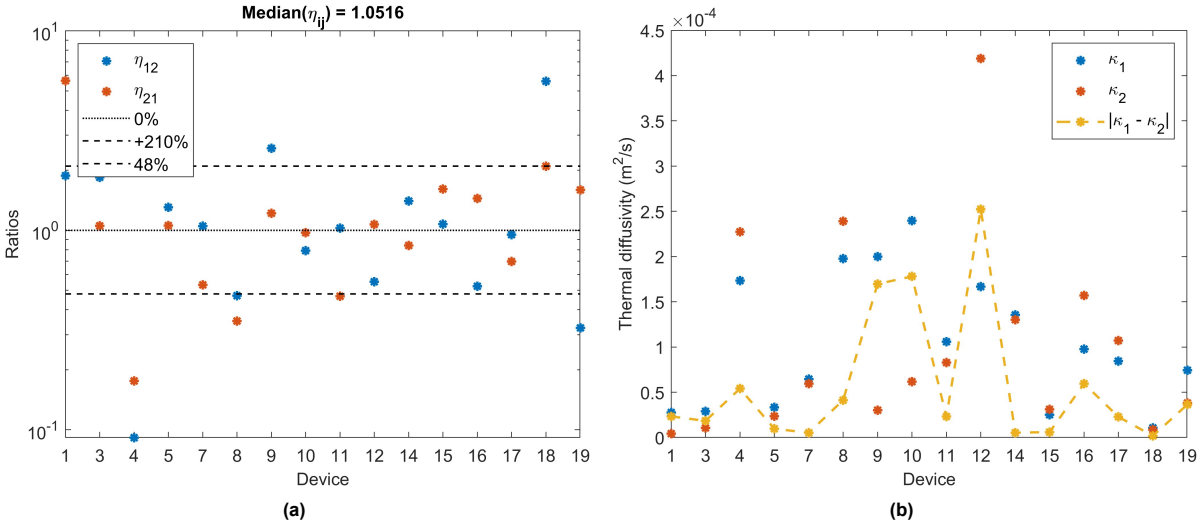

Figure 3.18: Results of η_{ij} and κ_i by device: (a) comparison of experimental thermal time constants and those calculated by procedure in figure 3.16; (b) variation in thermal diffusivity, along with difference between drum 1 and drum 2.

3.5. Dependence of thermal time constant on dumbbell size

There are four parameters for defining a dumbbell: R_1, R_2, x_0, and w y_0, as drawn in figure 2.1. The thermal time constant characterise the time for the heat flux to travel from the actuation to covering up the whole membrane, thus these four parameters should all play a role in the thermal time constants. As mentioned in section 4.1, it is difficult to recognise a pattern between any τ and parameter. Therefore,

it is more practical to summarise the τ-dumbbell size relationship using the COMSOL and analytical models, as they have been verified with experimental data in section 3.4. Same as section 3.4, subscript "ana" and "sim" are introduced to denote data derived by the analytical and COMSOL model, respectively.

Following the controlled variable method, the relationship between the thermal time constant and dumbbell dimensions are derived by the COMSOL model. The plots are arranged in figure 3.19.

With an increasing bridge length x_0 in figure 3.19a, bridge width exerts ignoble effect on $\tau_{11,ana}$ and $\tau_{11,sim}$, while both $\tau_{12,ana}$ and $\tau_{12,sim}$ experience a growing trend, almost linear to x_0. This corresponds with the physical meaning of τ: a longer bridge requires more time for heat flux to propagate. In addition, there are prominent gap between the simulated and analytical data. $\tau_{11,ana}$ is 14% less than $\tau_{11,sim}$, which coincides with the mismatch seen in figure 3.15 (g-i): a large k = 40 W/(m·K) incurs more noticeable differences between the simulated τ and its analytical counterpart. But in general, the trend of those simulated curves agrees with that of the analytical ones.

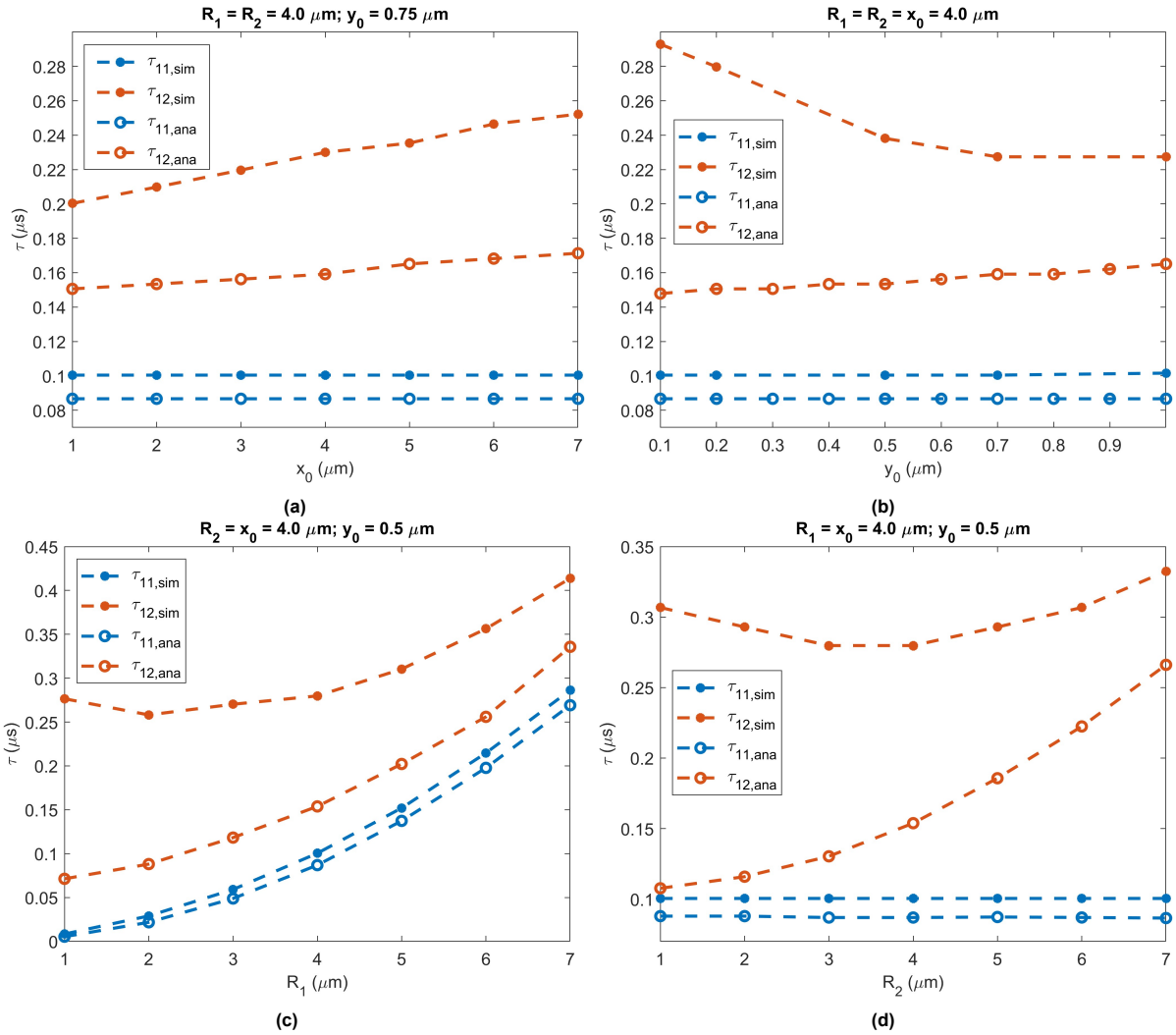

Figure 3.19: The relationship between thermal time constants and: (a) bridge width y_0; (b) bridge length x_0; (c) drum 1 radius R_1; (d) drum 2 radius R_2. Material properties for both COMSOL and analytical models follow figure 3.15 (g-i).

In figure 3.19b, $\tau_{11,ana}$ and $\tau_{11,sim}$ remains constant irrespective of bridge width y_0. However, $\tau_{12,ana}$ shows a slow growing trend while $\tau_{12,sim}$ drops fast with smaller y_0 and slows down with a larger y_0. A larger bridge width also calls for a longer time to heat up, so the physical meaning of τ supports the

trend of $\tau_{12,ana}$. Nonetheless, there are assumptions that simplifies the analytical model compared to the COMSOL one, so in turn the trend of $\tau_{12,ana}$ is not affected by some factors overlooked by those assumptions. This is detailed in section 4.3.

As for the radius of drum 1 R_1, the behaviour of both $\tau_{11,ana}$ and $\tau_{11,sim}$ demonstrate a almost parabolic relationship with R_1, which agrees with the theory in equation (1.30). $\tau_{12,ana}$ gives a same trend with a larger value because of the bridge part. While there is an initial decrease below R_1 = 2 μm in $\tau_{12,sim}$, followed by an accelerating rise. On the other hand, $\tau_{11,ana}$ and $\tau_{11,sim}$ remains almost unaffected by a changing R_2. Whereas $\tau_{12,ana}$ climbs up monotonously as R_2 increases. The pattern of $\tau_{12,sim}$ again differs from that of $\tau_{12,ana}$: it reaches a minimum between 3 and 4 μm, and appears monotonous on either side of the minimum. Physically, larger R_1 or R_2 should have resulted in a larger thermal time constant, and the reasons why not for the COMSOL model are discussed in section 4.3.

To sum up, the thermal time constants extracted from the analytical COMSOL models always exhibit a discrepancy, which is first captured in section 3.3 and then discussed insection 4.2. In figure 3.19, the behaviour of curves produced by the two models resembles only partially, and the reasons are explained in section 4.3.

4

Discussion

The results in chapter 3 present nearly 30% outliers in experimental data, and identifies a disagreement between the analytical and COMSOL model regarding average temperature in each dumbbell domain and the relationship of thermal time constants with dumbbell dimensions. This chapter discusses the reasons behind these mismatches.

4.1. Variation in experimental data

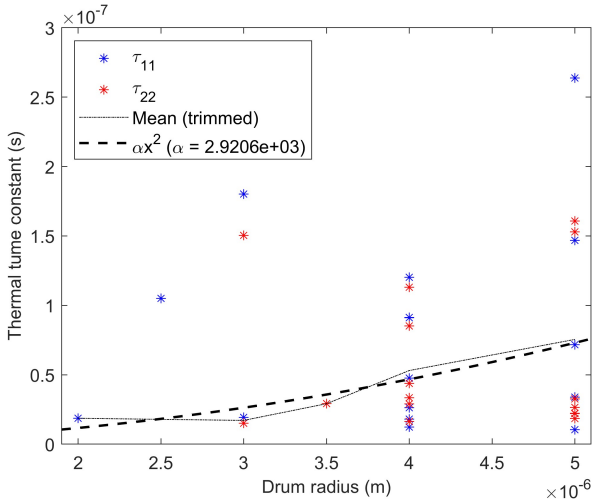

Figure 4.1: Dependence of thermal time constant on drum radius using experimental data

In figure 4.1 lies the τ_{11} and τ_{22} extracted from the experiments. Unfortunately, it is hard to find a convergence for each drum radius, not to mention that for some drum radius there is only one sample. Theoretically, a parabolic relation should be recognised between the thermal time constant and dumbbell radius, as indicated by equation (1.29). If we trim out the outliers, the mean values can form a parabolic curve (see the fitting of αx^2). But again, the trimming and curve fitting can be a wishful thinking, for there is no convergence for those data points and we seek for a relation presented in equation (1.29). Such large variation is reminiscent of the work of Dolleman et al[17]: they built circular resonators using monolayer molybdenum disulfide, and extracted thermal time constant τ with equation (1.29). The maximum τ is more than ten times larger than the smallest one for nanodrums with the same radius at 5 μm. Hence, given multilayer samples in our experiments, large variation in thermal times constants is understandable, and a limited sample size do not allow us to extract τ-dumbbell size relationship directly from the experimental data.

In section 3.2, we find thermal conductivity and laser locations culpable for the variation in experimental data, and then in section 3.4, the effect of thermal conductivity is cancelled out. Those obtained thermal time constants still show significant difference from the experimental data, and such difference is visualised in figure 3.17 and quantified by η_{ij} defined by equation (3.14). However, there are still almost 30$\%$ of outliers that cannot be explained by mere laser location deviation detailed in section 3.4, and the following text discusses the possible reasons.

First, the thermal diffusivity of the bridge part is assumed to be the average of that of drum 1 and drum 2, owing to a lack of experimental data. Hence, there is no physical reasoning behind such assumption. In the results of κ_1 and κ_2 in figure 3.18b, though 11 out 16 devices show a close κ_1 and κ_2 with a difference less than 5E-5 m^2/s, there are chances that κ_{bridge} deviate significantly from the assumed value. This can account for cases when both η_{12} and η_{21} are much larger or smaller than zero, which includes device 1, 4, 8, and 17.

Second, in section 3.2, range of laser deviation is limited to 3μm when $R_1 = R_2$ =4 μm. However, occasionally, the deviation can be larger. For example, in device 1, a $\tau_{12,exp}$ is measured smaller than $\tau_{11,exp}$, and the same occurs to $\tau_{21,exp}$ and $\tau_{22,exp}$. It also happens to device 9 and 17. For those devices, it is likely that when measuring $\tau_{12,exp}$ and $\tau_{21,exp}$, the distance between the red and blue lasers are smaller than l (see definition in figure 2.1), so that the thermal time constants are much underestimated. For other outliers found in device 11 and 18, they are just outside the error bar, thus can also come from a larger deviation of laser location than expected.

Third, irregularities of the membrane is another inherent contributor of variation. Liu[31] measured pretension for four graphene resonators, and the maximum one was 1.9 times larger than the smallest. And normalised areal tensity also featured a ratio of over 10 between the largest and the smallest. That indicates variation could be large in the same material, and from this point we can deduce that within one resonator, the material can also demonstrate appreciable variation. In our analysis, both COMSOL and analytical model feature a smooth membrane with the same material properties, at least within each domain. However, the variation in material properties can change the local temperature distribution. Consequently, the shift of input of the bridge part, or of the input of drum 2 in the analytical model would result in a different $\tau_{12,ana}$ or $\tau_{21,ana}$.

Other sources of variation include: (1) Curve fitting introduced in section 3.1 gives error in thermal time constants. Due to a high adjusted R^2 (mostly over 0.8), the error comes from fitting itself is small but not negligible. Moreover, we are still not sure why model 3 in section 3.1 works well with the curve fitting, or if there is a better model to extract thermal time constants for dumbbell resonators, so error might originate from fitting model per se. Additionally, the resonance is nonlinear in some measurements, but still a curve fitting model with linear resonance is applied. This is expected to induce minor error, but not yet verified. (2) Extracting thermal time constant using the valley location. Such error is briefed in section 3.1, which could introduce an error within 2$\%$. (3) Ambient temperature. There is no temperature controller in the experimental setup, so in theory thermal time constant can shift due to temperature changes. Unfortunately, we have not investigated how much this perturbation from temperature result in. (4) Thermal resistance at the edge. In the analytical model, the thermal resistance at the dumbbell edge is treated as infinity, but this value is difficult to measure directly in experiments, and the COMSOL model does not take into account the profile of a membrane, as depicted in figure 1.1a. It plays an important role in thermal time constant, as detailed in section 4.2.

In summary, a verification is conducted in section 3.3, giving nearly 30$\%$ of outliers. Such amount of outliers are mainly attributed to the coarse assumption of κ_{bg} in equation (3.13), larger deviation of lasers than applied in section 3.2, and variation of local material properties. Other factors include curve fitting error, valley location error, temperature shift in experiments, and thermal resistance at the dumbbell edge.

4.2. Differences between the analytical and COMSOL model

In section 3.3, the analytical model is compared with the COMSOL model, and a discrepancy between them, especially when thermal conductivity k is high, is identified. This section discusses four capable contributors: (1) coupling between drum 1 and bridge; (2) coupling between bridge and drum 2; (3) value of thermal conductivity; (4) boundary condition.

The first major difference between the COMSOL model and the analytical model lies in the assumption that the bridge part changes the temperature distribution of drum 1 $U_1(x)$ only marginally. However, the solution of $U_1(x)$ is utilised as the input of bridge part as the boundary condition on the left side. A minor change in $U_1(x)$ around the boundary might not affect the $U_{1,avg}$ but it can alter V_{avg}, and eventually $U_{1,avg}$. If this is true, we shall see a difference between the temperature of two points located symmetrical to the drum 1 centre. Thus, we mark the left side of bridge boundary as line B, and the symmetrical line B is marked on the other side of drum 1. Nest, at the midpoint of two lines, two representative points, Q_b and Q_d, are selected to showcase the temperature difference, as drawn in top figure 4.3.

The temperature of points Q_b and Q_d is displayed in figure 4.2 with various bridge width y_0. A temperature gap between the two locations can always be recognised for any y_0, but it widens for a larger y_0. The increase of temperature at Q_d due to y_0 is small, relative to that at Q_b. This verifies that the opening of bridge changes the local temperature distribution significantly.

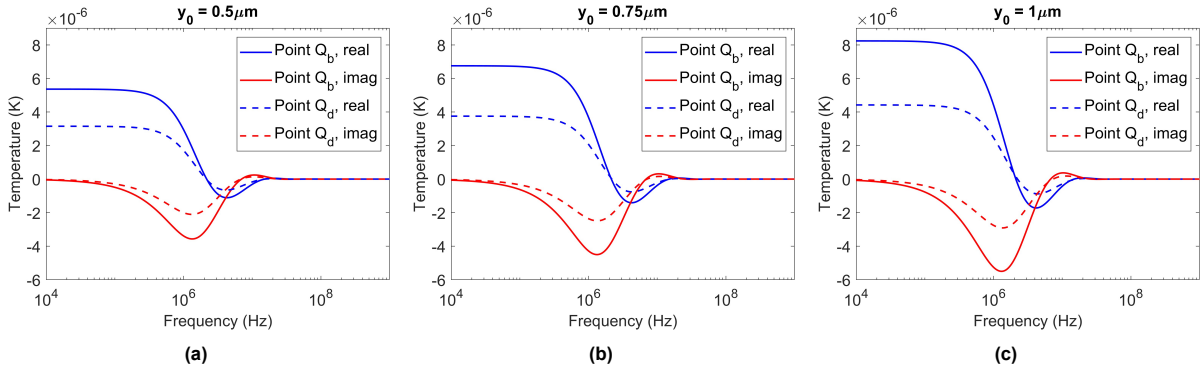

Figure 4.2: Comparison of temperature at point Q_b and Q_e when: (a) bridge half width y_0 =0.5 μm; (2) bridge half width y_0 =0.75 μm; bridge half width y_0 =1 μm. Boundary condition follows **BC1** defined in figure 2.10a.

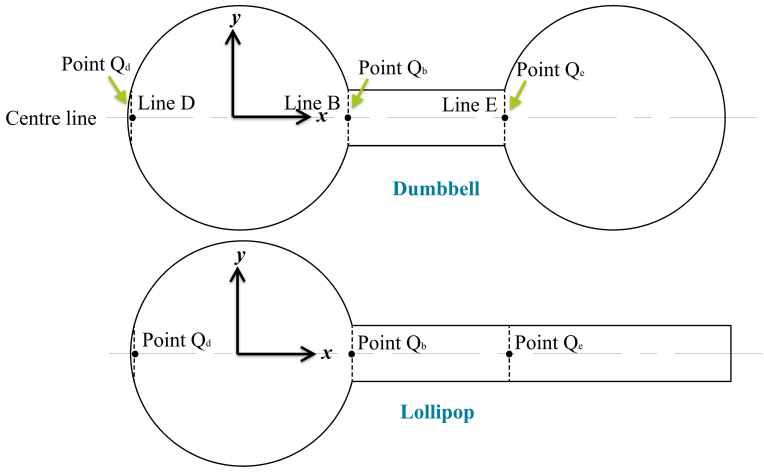

Figure 4.3: Two simulation setups to compare temperatures at three points, Q_d, Q_b, and Q_e. In the dumbbell setup (top), R_1 = R_2 = x_0 = 4 μm; y_0 = 0.5 μm. In the lollipop setup (bottom), R_1 = 4 μm, R_2 = 0, x_0 = 12 μm, y_0 = 0.5 μm. Point Q_e has the same coordinates in two setups, and the same for Q_d and Q_b. Boundary condition follows **BC1** desribed in figure 2.10a.

A similar assumption is made for the analytical model of drum 2: it would not change the temperature distribution of the bridge $V_(x, y)$. However, even for small bridge width (i.e. y_0 < 0.25R_2), this might not hold with large thermal conductivity k, as an educated guess for reason of the mismatch found in figure 3.15. To test this hypothesis, we need to delve into the boundary condition again. In the analytical model, the boundary at line E is free, which means the temperature at Q_e relies only on its x coordinates and the solution of drum 1, rather than the length of bridge. This inspires us to establish a

lollipop resonator with much longer bridge part and no drum 2 to compare the impact of drum 2 on the temperature at Q_e. Accordingly, the lollipop setup is drawn in bottom figure 4.3 to investigate contributor (2).

In figure 4.4, temperatures of two setups are compared, with various k. The existence of drum 2 makes the temperature amplitude marginally larger than the lollipop setup, even with k = 40 K/(W·K), and this gap is much smaller than the ones in figure 4.2. This denotes that coupling due to drum 2 is not the main contributor of the discrepancy seen in the solutions of the two models.

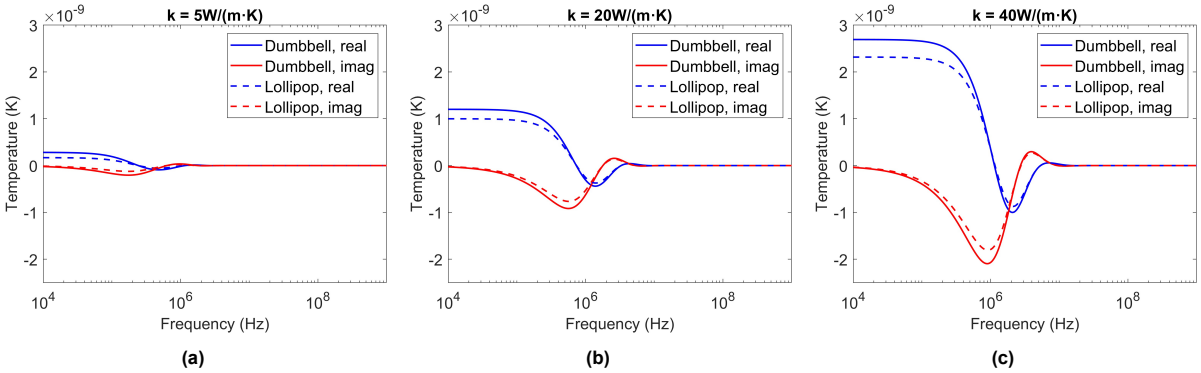

Figure 4.4: Temperature at point Q_e in both dumbbell and lollipop models with COMSOL, when thermal conductivity k equals to: (a) 5 W/(m·K); (b) 20 W/(m·K); (c) 40 W/(m·K). Boundary condition follows **BC1** shown in figure 2.10a.

The previous text discusses the influence of geometry that the analytical model does not take into account, and the following text measures the contributors of thermal conductivity and boundary condition with the simulation of dumbbell setup.

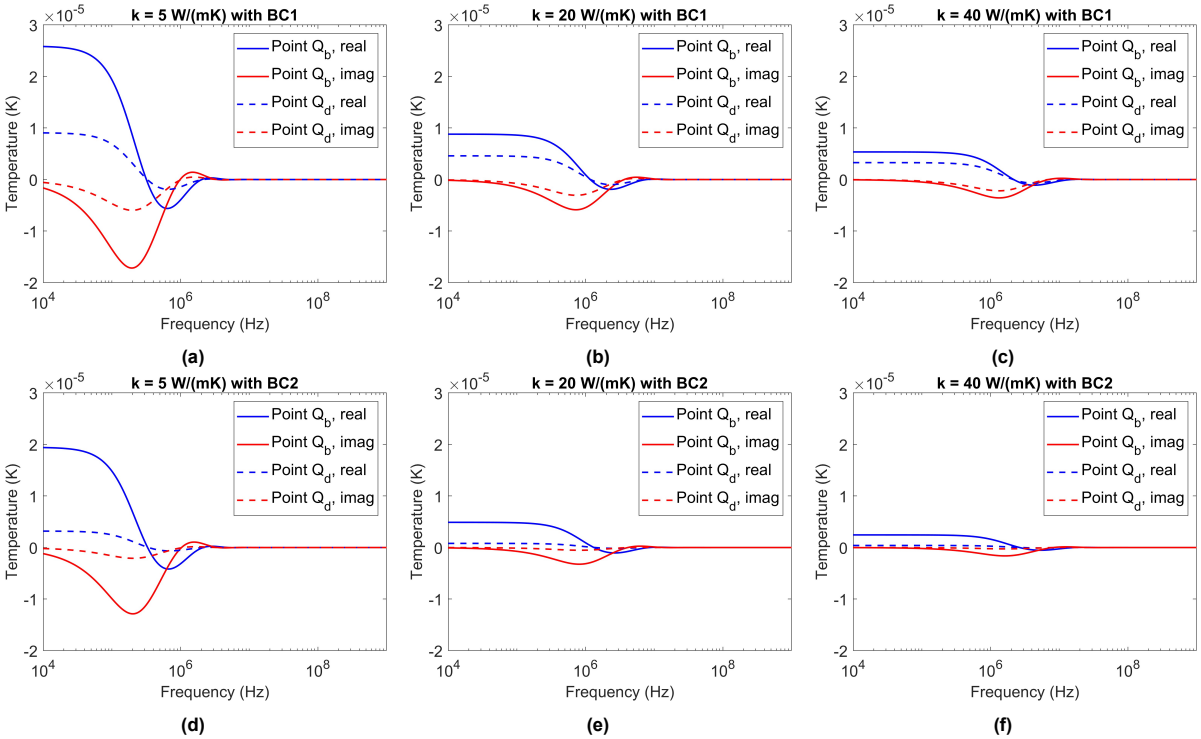

Figure 4.5: Temperatures of point Q_b and Q_d with three thermal conductivity values under two boundary conditions: (a-c) **BC1** and (d-f) **BC2**.

In figure 4.5, temperature amplitude of point Q_b and Q_d under two boundary conditions (i.e. **BC1** and **BC2**, see figure 2.10) with multiple thermal conductivity values are plotted. To further quantify the amplitude difference as well as valley location of the imaginary part, pertinent statistics are listed in table 4.1. The amplitude is defined in equation (4.1), where z_ω is the temperature signal. A ratio (dubbed ζ) between the temperature amplitude at point Q_b and Q_d is determined by equation (4.2). This ratio measures how large the temperature discrepancy is between the two points. The valley location (defined in section 3.2) marks the approximated thermal time constant, represented by τ in table 4.1.

BC2 always manifests a larger amplitude compared to **BC1**, and τ with **BC1** is always larger than that with **BC2**. Physically, this makes sense. A non-fixed boundary **BC2** allows heat to diffuse beyond the boundary, as evidenced by non-zero values at the edge in figure 4.6a. This gives rise to higher amplitudes at the dumbbell edge and longer time to heat up the membrane. However, the difference between τ under **BC1** and **BC2** is unaffected by the variation of the thermal conductivity k, so is the ratio ζ with **BC2**. While ζ with **BC1** declines with growing k. This signifies that k is not a significant contributor for the mismatch of τ, as observed in figure 3.19, and the pattern of the temperature distribution should be insensitive to k with **BC2**. But it changes with **BC1** in that the non-fixed boundary with larger k allows more heat to transfer outside the dumbbell domain, resulting in a reduced difference between the temperature amplitude of Q_b and Q_d.

$$\gamma_P = \int_{f_1}^{f_2} \mathrm{Re}\{z_w(2\pi f)\}\, df\,, \quad \text{where } P = Q_b, Q_d \tag{4.1}$$

$$\zeta = \frac{\gamma_{Q_b}}{\gamma_{Q_d}} \tag{4.2}$$

Table 4.1: Caption for the table.

k (W/(m·K))	τ (μs)		ζ	
	BC1	**BC2**	**BC1**	**BC2**
5	0.80	0.78	2.85	6.09
20	0.22	0.20	1.91	6.11
40	0.12	0.10	1.63	6.11

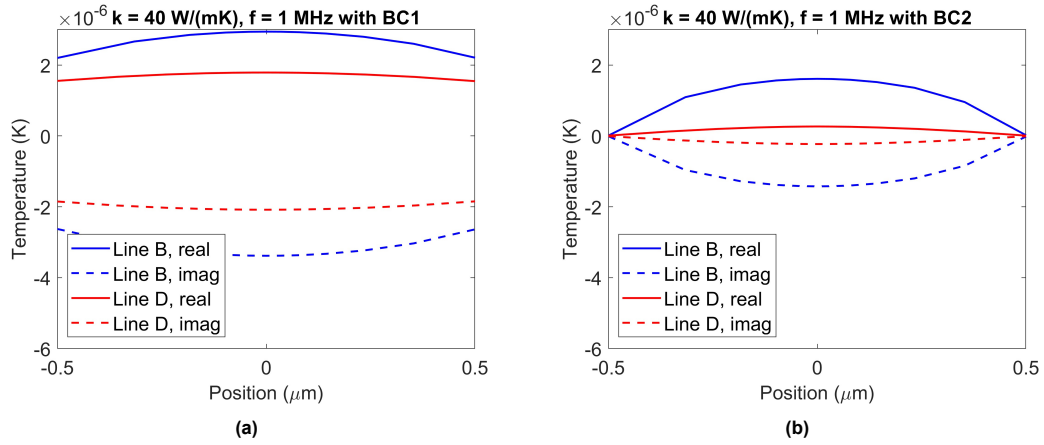

Figure 4.6: Comparison of temperature amplitude along line B and D with two boundary conditions: (a) with **BC1**, amplitude is not zero at the edge; (b) with **BC2**, amplitude is zero at the edge and is smaller than that with **BC1**.

As indicated by previous text, the dominate contributor to the discrepancy of the two models is a fixed temperature at the edge of the dumbbell in the analytical model while a free boundary for the COMSOL

model. This boundary condition in COMSOL is first illustrated in figure 2.10a, and applied throughout chapter 3. It is more realistic since heat can propagate beyond the edge of a dumbbell. But in the analytical model, it is difficult to determine the thermal resistance at the edge, so a fixed temperature is selected.

To further verify the aforementioned hypothesis, **BC2** is employed, as displayed in figure 2.10b. Using a thermal conductivity k = 40 W/(m·K), the results are shown in figure 4.7. The analytical model now follows the COMSOL model well. Such desired match-up proves that a large k lead to larger fluctuation of temperature at the edge of the dumbbell, which deviates further from the fixed temperature assumption in the analytical model.

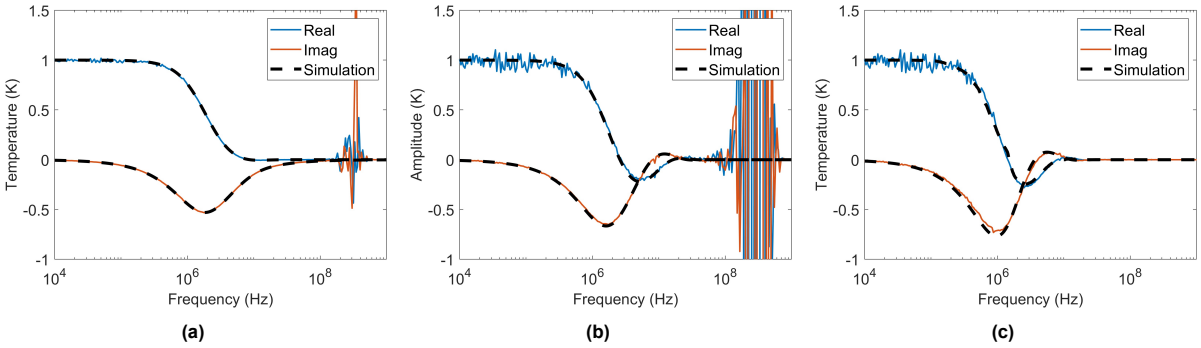

Figure 4.7: Average temperature of each domain with a thermal conductivity at 40 W/(m·K): (a) $U_{1,avg}$, (b) V_{avg}, and (c) $U_{2,avg}$. The red and blue lines indicate the real and imaginary part of the analytical model, while the dotted lines are for the COMSOL model. Boundary condition follows **BC2** introduced in figure 2.10b.

To summarise, all four contributors play a role in different amplitudes, with (1) coupling between drum 1 and bridge and (4) boundary condition being the dominant ones. Whereas only contributor (4) accounts for the discrepancy in thermal time constants.

4.3. Restriction of a dumbbell shape

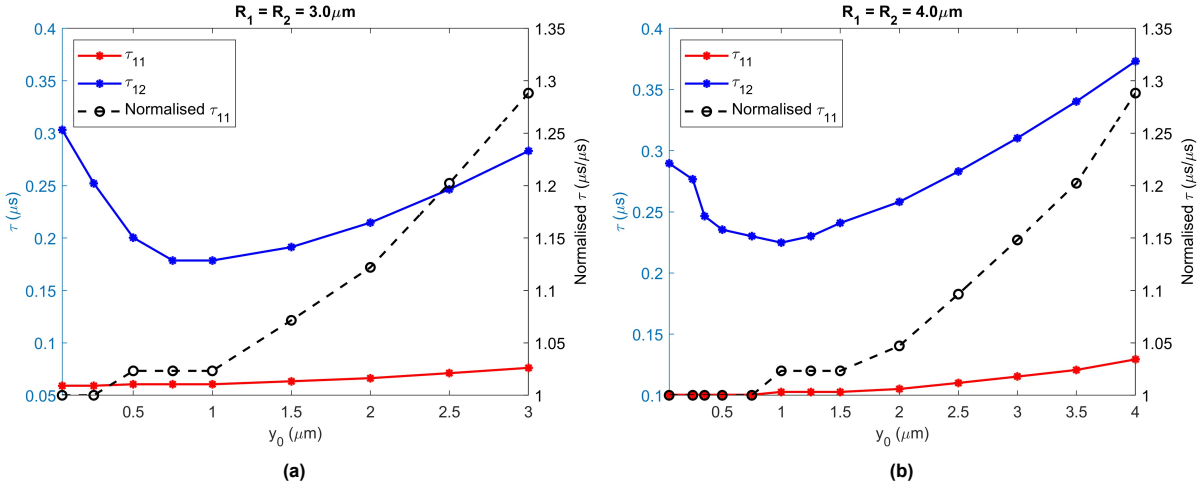

Figure 4.8: Behaviour of thermal time constants with larger variation of bridge width y_0: (a) when both radius are 3.0 μm; (b) when both radius are 4.0 μm. Other parameters are fixed.

In section 4.2, we notice that if R_2 = 0, then the dumbbell shape degrades to a lollipop. Equally, when y_0 approximates one of the drum radius, the shape is analogous to a stadium. In the analytical model, two assumptions are made for a dumbbell shape: the bridge should not affect the solution in drum 1, i.e. $U1(x)$; and drum 2 should not affect the solution in the birdge, i.e. $V(x, y)$. However, when some

parameters become too large or small, these assumptions no longer hold, thus giving a different τ, as seen in figure 3.19. To address this issue, COMSOL simulations are conducted for various y_0 with two drum radius.

Shifting y_0 from 0.1 μm to drum radius, and the corresponding τ_{11} and τ_{12} are plotted in figure 4.8. To evaluate how much τ_{11} has changed due to the presence of the bridge, the thermal time constant of a circular drum is obtained as τ_{11s}, and a normalised value $\frac{\tau_{11}}{\tau_{11s}}$ is calculated. For $R_1 = R_2 = 4\,\mu m$, the normalised τ is less than 1.05 when y_0 is smaller than 1 μm. While for $R_1 = R_2 = 4\,\mu m$, y_0 registers 1.5 μm for the same condition. Thus, it is safe to say y_0 should be less than 25% of the smaller drum radius to make τ_{11} unaffected by the bridge geometry. A y_0 larger than this 25% critical value can bring about a surging τ_{11} up to 30% larger than τ_{11s}.

Interestingly, τ_{12} in both sub-figures of figure 4.8 demonstrate a minimum around the critical value of 25%, as mentioned in the last paragraph. For R_1 = R_2 = 4 μm, the minimum is situated at around 0.9 μm, i.e. 23 % of the drum radius. While for R_1 = R_2 = 3 μm, the percentage creeps up to 33 %, at around 1 μm. This phenomenon corresponds with the (partial) decrease of $\tau_{12,ana}$ in figure 3.19b, figure 3.19c, and figure 3.19d, where y_0 is relatively small as opposed to R_1 or R_2.

To explain the initial downward trend mathematically, we need to resort to the analytical model, although it does not demonstrate such trend. For this matter, the solution of drum 1 temperature is brought to equation (4.3), along with the boundary condition of the bridge in equation (4.4). When y_0 grows, the boundary condition in equation (4.4) takes the value of $U_1(x)$ with a smaller x. A smaller x in Bessel function $J(mx)$ indicates a valley location at a higher frequency (see green arrows in figure 4.9), which in turn gives a smaller τ. This smaller τ translates into the initial downward trend produced by the COMSOL model, but the analytical model fails to capture this. The reason probably lies in the solution of $U_2(x)$, given that the trend of $tau_{11,ana}$ and $tau_{11,sim}$ always resemble each other in figure 3.19. $U_2(x)$ of the analytical model is primarily shaped by the boundary condition from the bridge part, and this boundary condition is changed due to the presence of bridge, the same way bridge changes the boundary of drum 1 (see figure 4.2).

$$u_1(x,t) = \sum_{i=0}^{n-1} c_i \left[J_i(mx) - \frac{J_i(mR)}{J_n(mR)} J_n(mx) \right] e^{i\omega t} \tag{4.3}$$

$$v(x, y = \pm y_0, t) = 0; \quad v(x = 0, y, t) = u_1(\sqrt{y^2 + R_1^2 - y_0^2}, t) \tag{4.4}$$

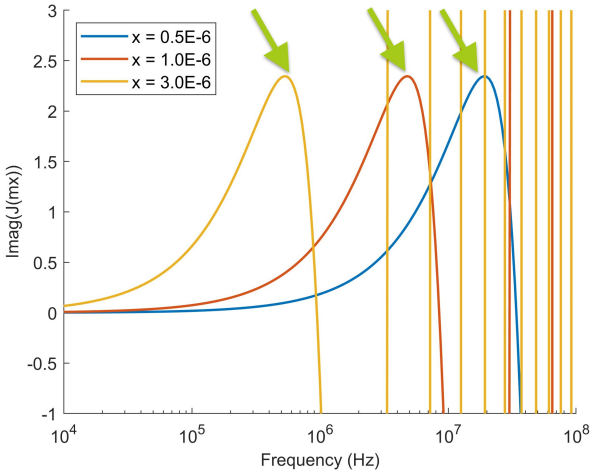

Figure 4.9: Extra plot for mathematical explanations on τ_{12} curves in figure 3.19a: valley location of $J(mx)$, as highlighted by the green arrows, moves to the left side given a larger x, which means a larger τ in the end. x in the legend refers to that in function $J(mx)$.

Physically, the initial decrease of τ_{12} accounts for the relatively wide bridge that allows the heat to

travel to drum 2 more efficiently, producing a smaller τ_{12}. But as the bridge continues to widen, this is eventually countered by the time to heat up the bridge itself, thus a growing trend ensues.

In a nutshell, for a fixed radius, there must be a bridge width that brings about a smallest τ_{12} or τ_{21}. This minimum is reached with a balance of efficient heat transport through the bridge and tolerable time to warm up the bridge itself.

5

Conclusion

This thesis investigates the thermal time constants of a dumbbell-shape 2D resonator with analytical, simulation, and experimental method.

First, optomechanical measurements are conducted for 19 devices fabricated with molybdenum disulfide, and the corresponding thermal time constants are extracted with a comparison of three models. The extracted thermal time constants exhibit large variation, thus impossible to discern any pattern against dumbbell size directly. Then, the COMSOL model is established to find out what causes such variation in experiments, and to recognise the pattern clouded by the experimental variation. Moreover, The analytical approach is employed to better understand the temperature distribution by solving a series of heat equations.

As a result, over 70$\%$ of the experimental data can be explained by the combination of two models. The outliers can be accounted for by unexpected thermal conductivity of the bridge part, too much deviation (over 3 μm) of laser location, along with irregularities of membranes. As for the pattern against dumbbell sizes, the bridge width relative to drum radius plays a major role: narrow bridges are not efficient in heat transport so bigger thermal time constants ensue, while wide bridges needs more time to heat up itself, thus a large thermal time constant can also be calculated. Therefore, there is always an optimal bridge width for a dumbbell that allows the smallest τ_{12} or τ_{21}.

The amplitude discrepancy between the analytical model and the COMSOL model is mainly ascribed to the coupling between drum 1 and bridge and a non-fixed boundary of the dumbbell in COMSOL model. While the discrepancy in thermal time constant is only induced by the aforementioned boundary difference. Such discrepancy become significant for the calculation of τ_{12} or τ_{21} when thermal conductivity is larger than 10 W/(m·K).

There is much to continue and improve for this project, especially the analytical part. The analytical model can be upgraded by treating the boundary between drum 1 and bridge as free, as well as investigating how to determine the thermal resistance at the boundary instead of treating it as infinity. Moreover, the vibration is not coupled into the analytical model, and the addition of it can shed some light on why there is a term linear to frequency in curve fitting model 3 in equation (3.3). Then, how to derive the optimal bridge width for the minimal thermal time constant is not yet known, which can also benefit from a more thorough analytical model. Regarding experiments, means to reduce variation are appreciated. For example, using one large monolayer flake to cover multiple dumbbell cavities (even the whole chip) is desired. Thus, chemical deposition might be a better way to fabricate samples for dumbbells as it produces more large thin flakes.

References

[1] Alexander A Balandin et al. “Superior thermal conductivity of single-layer graphene”. In: *Nano letters* 8.3 (2008), pp. 902–907.

[2] Yahav Ben-Shimon and Assaf Ya’Akobovitz. “Magnetic excitation and dissipation of multilayer two-dimensional resonators”. In: *Applied Physics Letters* 118.6 (2021).

[3] Ewald Benes et al. “Sensors based on piezoelectric resonators”. In: *Sensors and Actuators A: Physical* 48.1 (1995), pp. 1–21.

[4] Theodore L Bergman. *Fundamentals of heat and mass transfer*. John Wiley & Sons, 2011.

[5] Theodore L Bergman et al. *Introduction to heat transfer*. John Wiley & Sons, 2011.

[6] J Scott Bunch et al. “Electromechanical resonators from graphene sheets”. In: *Science* 315.5811 (2007), pp. 490–493.

[7] Weiwei Cai et al. “Thermal transport in suspended and supported monolayer graphene grown by chemical vapor deposition”. In: *Nano letters* 10.5 (2010), pp. 1645–1651.

[8] Andres Castellanos-Gomez et al. “Mechanics of freely-suspended ultrathin layered materials”. In: *Annalen der Physik* 527.1-2 (2015), pp. 27–44.

[9] Andres Castellanos-Gomez et al. “Single-layer MoS2 mechanical resonators”. In: *Advanced Materials* 25.46 (2013), pp. 6719–6723.

[10] Andres Castellanos-Gomez et al. “Strong and tunable mode coupling in carbon nanotube resonators”. In: *Physical Review B* 86.4 (2012), p. 041402.

[11] Changyao Chen et al. “Performance of monolayer graphene nanomechanical resonators with electrical readout”. In: *Nature nanotechnology* 4.12 (2009), pp. 861–867.

[12] Dejan Davidovikj et al. “Nonlinear dynamic characterization of two-dimensional materials”. In: *Nature Communications* 8.1 (2017), p. 1253.

[13] Dejan Davidovikj et al. “On-chip heaters for tension tuning of graphene nanodrums”. In: *Nano letters* 18.5 (2018), pp. 2852–2858.

[14] Dejan Davidovikj et al. “Visualizing the motion of graphene nanodrums”. In: *Nano letters* 16.4 (2016), pp. 2768–2773.

[15] Guang-Wei Deng et al. “Strongly coupled nanotube electromechanical resonators”. In: *Nano letters* 16.9 (2016), pp. 5456–5462.

[16] Robin J Dolleman et al. “Optomechanics for thermal characterization of suspended graphene”. In: *Physical Review B* 96.16 (2017), p. 165421.

[17] Robin J Dolleman et al. “Transient thermal characterization of suspended monolayer MoS 2”. In: *Physical Review Materials* 2.11 (2018), p. 114008.

[18] Ruixiang Fei et al. “Enhanced thermoelectric efficiency via orthogonal electrical and thermal conductances in phosphorene”. In: *Nano letters* 14.11 (2014), pp. 6393–6399.

[19] Andre K Geim and Konstantin S Novoselov. “The rise of graphene”. In: *Nature materials* 6.3 (2007), pp. 183–191.

[20] Matthew J Hancock. “The 1-D heat equation”. In: *MIT OpenCourseWare. Accessed August* 31 (2006), p. 2018.

[21] Frank P Incropera et al. *Fundamentals of heat and mass transfer*. Vol. 6. Wiley New York, 1996.

[22] Jin-Wu Jiang, Harold S Park, and Timon Rabczuk. “Molecular dynamics simulations of single-layer molybdenum disulphide (MoS2): Stillinger-Weber parametrization, mechanical properties, and thermal conductivity”. In: *Journal of Applied Physics* 114.6 (2013).

[23] Tao Jiang and Yong Zhu. “Measuring graphene adhesion using atomic force microscopy with a microsphere tip”. In: *Nanoscale* 7.24 (2015), pp. 10760–10766.

[24] Ata Keskekler et al. “Symmetry-breaking-induced frequency combs in graphene resonators”. In: *Nano letters* 22.15 (2022), pp. 6048–6054.

[25] SunPhil Kim, Jaehyung Yu, and Arend M Van Der Zande. “Nano-electromechanical drumhead resonators from two-dimensional material bimorphs”. In: *Nano letters* 18.11 (2018), pp. 6686–6695.

[26] Jan N Kirchhof et al. “Tunable graphene phononic crystal”. In: *Nano Letters* 21.5 (2021), pp. 2174–2182.

[27] Jaesung Lee et al. “High frequency MoS2 nanomechanical resonators”. In: *ACS nano* 7.7 (2013), pp. 6086–6091.

[28] Wu Li, Jesús Carrete, and Natalio Mingo. “Thermal conductivity and phonon linewidths of monolayer MoS2 from first principles”. In: *Applied Physics Letters* 103.25 (2013).

[29] Xuesong Li et al. “Large-area synthesis of high-quality and uniform graphene films on copper foils”. In: *science* 324.5932 (2009), pp. 1312–1314.

[30] Yuhao Li et al. “Mapping the elastic properties of two-dimensional MoS2 via bimodal atomic force microscopy and finite element simulation”. In: *NPJ Computational Materials* 4.1 (2018), p. 49.

[31] Hanqing Liu. “Mechanics and thermodynamics of suspended two-dimensional membranes”. In: (2023).

[32] Hanqing Liu et al. “Enhanced photothermal response near the buckling bifurcation in 2D nanomechanical resonators”. In: *arXiv preprint arXiv:2305.00712* (2023).

[33] Hanqing Liu et al. “Nanomechanical resonators fabricated by atomic layer deposition on suspended 2D materials”. In: *2D Materials* 10.4 (2023), p. 045023.

[34] Hanqing Liu et al. “Tension tuning of sound and heat transport in graphene”. In: *arXiv preprint arXiv:2204.06877* (2022).

[35] Xiangjun Liu et al. “Phonon thermal conductivity of monolayer MoS2 sheet and nanoribbons”. In: *Applied Physics Letters* 103.13 (2013).

[36] Gang Luo et al. “Strong indirect coupling between graphene-based mechanical resonators via a phonon cavity”. In: *Nature communications* 9.1 (2018), pp. 1–6.

[37] Kin Fai Mak et al. “Atomically thin MoS 2: a new direct-gap semiconductor”. In: *Physical review letters* 105.13 (2010), p. 136805.

[38] Tengfei Miao et al. “Graphene nanoelectromechanical systems as stochastic-frequency oscillators”. In: *Nano letters* 14.6 (2014), pp. 2982–2987.

[39] DL Nika et al. “Lattice thermal conductivity of graphene flakes: Comparison with bulk graphite”. In: *Applied Physics Letters* 94.20 (2009).

[40] Kostya S Novoselov et al. “Electric field effect in atomically thin carbon films”. In: *science* 306.5696 (2004), pp. 666–669.

[41] IE Rosłoń et al. “High-frequency gas effusion through nanopores in suspended graphene”. In: *Nature Communications* 11.1 (2020), p. 6025.

[42] Banafsheh Sajadi et al. “Experimental characterization of graphene by electrostatic resonance frequency tuning”. In: *Journal of Applied Physics* 122.23 (2017).

[43] Ali Sarafraz et al. “Pressure-induced nonlinear resonance frequency changes for extracting Young’s modulus of nanodrums”. In: *Nonlinear Dynamics* (2023), pp. 1–11.

[44] Hannes C Schniepp et al. “Bending properties of single functionalized graphene sheets probed by atomic force microscopy”. In: *ACS nano* 2.12 (2008), pp. 2577–2584.

[45] Rajan Singh et al. “Motion transduction with thermo-mechanically squeezed graphene resonator modes”. In: *Nano letters* 18.11 (2018), pp. 6719–6724.

[46] V Singh et al. “Optomechanical coupling between a multilayer graphene mechanical resonator and a superconducting microwave cavity”. In: *Nature nanotechnology* 9.10 (2014), pp. 820–824.

[47] Makars Šiškins et al. “Tunable strong coupling of mechanical resonance between spatially separated FePS3 nanodrums”. In: *Nano letters* 22.1 (2021), pp. 36–42.

[48] Peter G Steeneken et al. “Dynamics of 2D material membranes”. In: *2D Materials* 8.4 (2021), p. 042001.

[49] Ching-Yuan Su et al. “High-quality thin graphene films from fast electrochemical exfoliation”. In: *ACS nano* 5.3 (2011), pp. 2332–2339.

[50] Hideo Suzuki, Naoki Yamaguchi, and Hideaki Izumi. “Theoretical and experimental studies on the resonance frequencies of a stretched circular plate: Application to Japanese drum diaphragms”. In: *Acoustical science and technology* 30.5 (2009), pp. 348–354.

[51] GJ Verbiest et al. “Tunable coupling of two mechanical resonators by a graphene membrane”. In: *2D Materials* 8.3 (2021), p. 035039.

[52] Guorui Wang et al. “Bending of multilayer van der Waals materials”. In: *Physical Review Letters* 123.11 (2019), p. 116101.

[53] Xiaolin Wei et al. “Phonon thermal conductivity of monolayer MoS2: A comparison with single layer graphene”. In: *Applied Physics Letters* 105.10 (2014).

[54] Dana Weinstein et al. “Mechanical coupling of 2D resonator arrays for MEMS filter applications”. In: *2007 IEEE International Frequency Control Symposium Joint with the 21st European Frequency and Time Forum*. IEEE. 2007, pp. 1362–1365.

[55] Bo Xu et al. “Nanomechanical resonators: toward atomic scale”. In: *Acs Nano* 16.10 (2022), pp. 15545–15585.

[56] Yanyan Xu et al. “Liquid-phase exfoliation of graphene: an overview on exfoliation media, techniques, and challenges”. In: *Nanomaterials* 8.11 (2018), p. 942.

[57] Yue-De Yang, Shi-Jiang Wang, and Yong-Zhen Huang. “Investigation of mode coupling in a microdisk resonator for realizing directional emission”. In: *Optics Express* 17.25 (2009), pp. 23010–23015.

[58] Zhuo-Zhi Zhang et al. “Coherent phonon dynamics in spatially separated graphene mechanical resonators”. In: *Proceedings of the National Academy of Sciences* 117.11 (2020), pp. 5582–5587.

[59] Zijian Zhang et al. “High-Sensitivity Force Sensors Based on Novel Materials”. In: *Advanced Devices & Instrumentation* 4 (2023), p. 0019.

[60] Xu-Qian Zheng, Jaesung Lee, and Philip X-L Feng. “Hexagonal boron nitride nanomechanical resonators with spatially visualized motion”. In: *Microsystems & Nanoengineering* 3.1 (2017), pp. 1–8.

A

Coupling in a dumbbell resonator

In this appendix, the signal of coupled thermal signal and fundamental resonance for a dumbbell is derived. First, consider drum 1 and drum 2 of the dumbbell resonator:

$$\begin{aligned} m_1\ddot{z}_1 + c_1\dot{z}_1 + k_1 z_1 &= f_d^1 e^{i\omega t} + \Gamma x_2 \\ m_2\ddot{z}_2 + c_2\dot{z}_2 + k_2 z_2 &= f_d^2 e^{i\omega t} + \Gamma x_1 \end{aligned} \tag{A.1}$$

where m_i, c_i, k_i are mass, damping, and spring coefficient for drum i; z_i is the generalised coordinate for drum i, and Γ is the coupling strength. The driving force is further expressed as:

$$f_d^i = \frac{A_{th,i}}{1 + j\omega\tau_i}, \quad where\ j^2 = -1,\ i = 1, 2 \tag{A.2}$$

Then the solution of z_i is supposed to be in the form of:

$$\begin{aligned} z_1 &= Z_1\, e^{j(\omega t + \phi_1)} \\ z_2 &= Z_2\, e^{j(\omega t + \phi_2)} \end{aligned} \tag{A.3}$$

where Z_1 and Z_2 are complex constants. Next, equation (A.3) is taken back to equation (A.1) to solve for Z_1 and Z_2. This results in the matrix equation:

$$\begin{pmatrix} -m_1\omega^2 + jc_1\omega + k_1 & -\Gamma \\ \Gamma & -m_2\omega^2 + jc_2\omega + k_2 \end{pmatrix} \begin{pmatrix} Z_1 \\ Z_2 \end{pmatrix} = \begin{pmatrix} \frac{A_{th,1}}{1+j\omega\tau_1} \\ \frac{A_{th,2}}{1+j\omega\tau_2} \end{pmatrix} \tag{A.4}$$

Finally, A_1 and A_2 are solvable by matrix inverse.

In our experiments, there is only one actuation, at either drum 1 or drum 2, so either f_d^1 or f_d^2 is zero. Hence, when setting f_d^2 = 0, actuation is located in drum 1, and Z_1 should be the amplitude of measurement drum 11, while Z_2 is that of drum 12. This leads to the solution of equation (A.4), displayed in equations (A.6) and (A.7). Another case is when f_d^1 = 0, and this yields the solution in equations (A.9) and (A.10). In those solutions, z_{mn} denotes measurement drum mn, where m, n = 1, 2.

Case 1 : $f_d^2 = 0$ (A.5)

$$z_{11}(\omega) = Z_1 = \frac{1}{-m_1\omega^2 + jc_1\omega + k_1 - \Gamma^2/(-m_2\omega^2 + jc_2\omega + k_2)} \cdot \frac{A_{th,1}}{1 + i\omega\tau_{11}} \tag{A.6}$$

$$z_{12}(\omega) = Z_2 = \frac{\Gamma}{(-m_1\omega^2 + jc_1\omega + k_1)(-m_2\omega^2 + jc_2\omega + k_2) - \Gamma^2} \cdot \frac{A_{th,1}}{1 + i\omega\tau_{11}} \tag{A.7}$$

Case 2 : $f_d^1 = 0$ (A.8)

$$z_{21}(\omega) = Z_1 = \frac{\Gamma}{(-m_1\omega^2 + jc_1\omega + k_1)(-m_2\omega^2 + jc_2\omega + k_2) - \Gamma^2} \cdot \frac{A_{th,2}}{1 + i\omega\tau_{22}} \tag{A.9}$$

$$z_{22}(\omega) = Z_2 = \frac{1}{-m_2\omega^2 + jc_2\omega + k_2 - \Gamma^2/(-m_1\omega^2 + jc_1\omega + k_1)} \cdot \frac{A_{th,2}}{1 + i\omega\tau_{22}} \tag{A.10}$$

Furthermore, z_{11} and z_{22} can be written as:

$$z_{11}(\omega) = \frac{1}{1 - \Gamma^2/\left[(-m_1\omega^2 + jc_1\omega + k_1)(-m_2\omega^2 + jc_2\omega + k_2)\right]} \cdot \frac{A_{th,1}}{1 + i\omega\tau_{11}} \cdot \frac{1}{-m_1\omega^2 + jc_1\omega + k_1} \tag{A.11}$$

$$z_{22}(\omega) = \frac{1}{1 - \Gamma^2/\left[(-m_1\omega^2 + jc_1\omega + k_1)(-m_2\omega^2 + jc_2\omega + k_2)\right]} \cdot \frac{A_{th,2}}{1 + i\omega\tau_{22}} \cdot \frac{1}{-m_2\omega^2 + jc_2\omega + k_2} \tag{A.12}$$

Hence, equation (A.11) and equation (A.12) resemble equation (3.2) in curve fitting. However, why equation (3.3) does not exhibit any resemblance to the solutions presented above remains unknown.